THEORETICAL INVESTIGATION OF A LASER TRIGGERED GAS SPARK GAP

A Thesis presented to the Faculty of the Graduate School

University of Missouri-Columbia

In Partial Fulfillment of the

Requirements for the Degree

Master of Science

By

ERIC WORTS

Dr. Scott Kovaleski, Thesis Advisor

DECEMBER 2005

The undersigned, appointed by the Dean of the Graduate School,
have examined the thesis entitled.

THEORETICAL INVESTIGATION OF

A LASER TRIGGERED SPARK GAP

Presented by Eric Worts

A candidate for the degree of Master of Science.

And hereby certify that in their opinion it is worthy of acceptance.

Acknowledgements

Many people deserve recognition for assisting me in the completion of my Master's work. The person that has been the most influential is my advisor, Dr. Scott Kovaleski. He has been an excellent guide through the trials and tribulations of graduate work. The lessons that I have learned have not only been beneficial to the project, but will prove to be advantageous throughout the rest of my career as an Electrical Engineer. I would also like to thank Dr. William C. Nunnally and Lawrence Livermore National Laboratories for financial support of the project.

I also received assistance from several other students and professors whom I would like to acknowledge. Dr. John Gahl and Dr. Justin Legarski were crucial influences when I first began my graduate studies. Mark Kemp, Andy Benwell, Matt Koukl and Ashkan Seyadi are among the students that have lent a hand with this research.

My wife, whom I love, has had perhaps the hardest job by putting up with me for the past two years. Other than proofreading numerous drafts of papers and this thesis, she has provided intangible support in the form of words of encouragement and cooking dinner after long nights at the lab. Finally, I cannot forget my dog, Growlie, who is only happy that I came home and can make me forget about work for a little while.

Table of Contents

Table of Figures

Table of Tables

Chapter 1

Introduction and Background

1.1 Introduction to the Blumlein and Spark Gap Switch

Blumleins are well-known, compact pulse power sources consisting of two transmission lines stacked together sharing a center conductor [1]. Three parallel plates separated by a dielectric make up the Blumlein. The center plate is charged to a high voltage. The charge voltage and the capacitance of the Blumlein indicate how much energy is stored in the system. Energy is found from

$$E = \frac{1}{2}CV^2$$

(1)

where V is voltage and C is capacitance. Because there are two transmission lines, the amount of energy stored in the Blumlein is double what would be stored in a single transmission line pulse-forming network. When the high voltage plate is shorted to ground by a switch, a high current pulse is generated in the Blumlein. This short can be accomplished a number of ways; one method is a gas-filled spark gap. This switch

1

creates an electrical connection between the center plate and one of the outside plates.

The opposite plate is connected to ground through high impedance so that the generated

current pulse is reflected back to the load. The current pulse generates a voltage across

the load, which is attached to the opposite end of a Blumlein from the switch across the

two outside plates. A depiction of a Blumlein can be seen in Figure 1. Figure 2

illustrates the behavior of a pulse in a Blumlein. A pulse travels the length of the

transmission line after the switch has initiated a short between the high and low potential

plates. The voltage across the load is equal to the charge voltage and lasts as long as

twice the time it takes for the pulse to travel the length of the Blumlein.
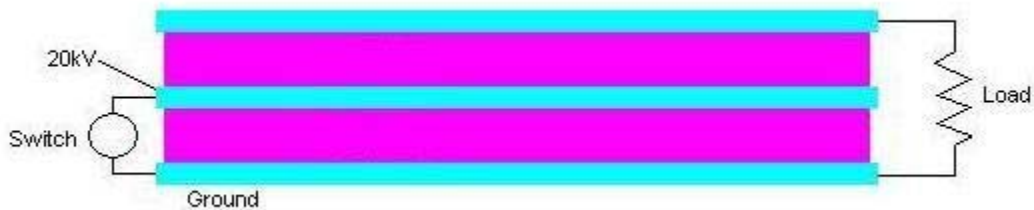
Figure 1 - A Blumlein. The spark gap triggering mechanism is located on the left side and the load is attached to the right side. The center plate is charged to 20 kV and the outside plates are grounded.

2
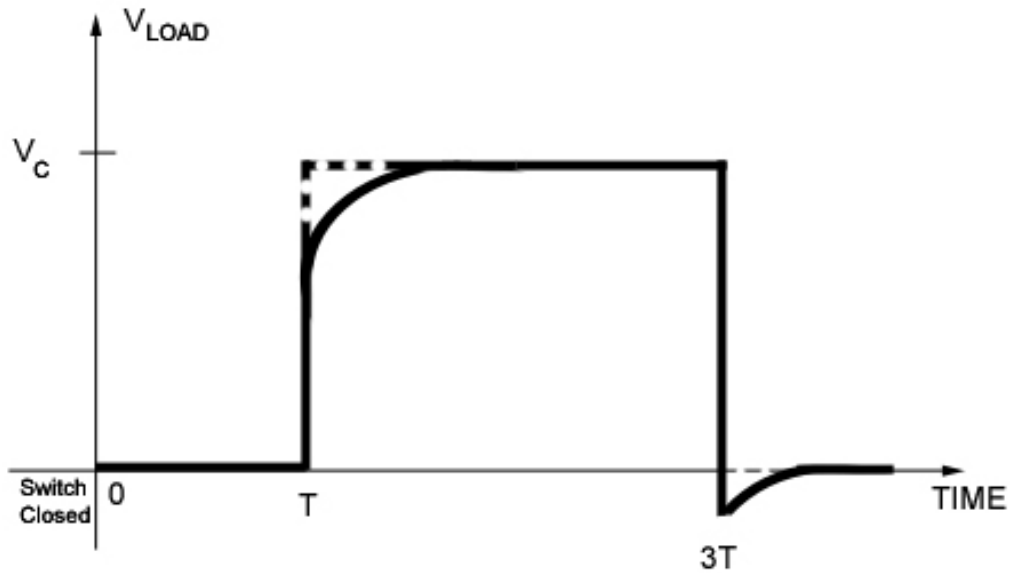
Figure 2 - Behavior of a pulse in a Blumlein pulsed power system. The pulse travels the length of the Blumlein in time T and is developed over the load for twice that time. The rise time of the pulse is the time taken for the pulse to reach the charge voltage.

One disadvantage of using a single transmission line as a pulse-forming line is that the pulse generated into a matched load is equal to half of the original voltage on the transmission line. A matched load means that the attached load has an equal resistance to the impedance of the transmission line. The impedance of the transmission line is determined by

$$Z_0 = \sqrt{\frac{L}{C}} \tag{2}$$

where L is the inductance of the line and C is the capacitance. When a pulse is triggered, half of the voltage is developed across the line itself, while the other half is developed across the load. This is a disadvantage in high voltage experiments; power supplies

3

needed to charge the line are required to provide twice the total voltage needed across the load.

The two transmission lines that make up a Blumlein enable the full voltage to be developed across the load because twice the energy is stored in the Blumlein. Both transmission lines deposit energy across the load at the same time, while summing the voltages together. Stacking several Blumleins using coordinated switches allows for the voltage across the load to multiply by the number of stacked Blumleins [2-3]. For example, ten stacked Blumleins charged to 1000 V will develop 10 kV across a matched load if all of the switches are triggered at the same time.
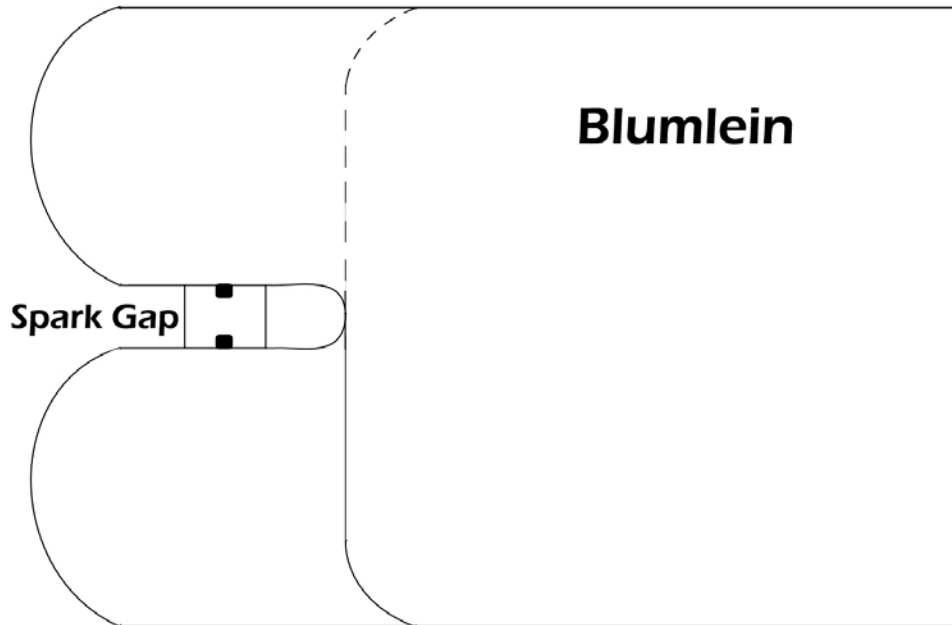
Figure 3 - Illustration of where the spark gap switch connects the two plates on the Blumlein.

The shorting switch investigated in this study is a laser triggered, gas-filled spark gap. Figure 3 illustrates how the switch is connected to the Blumlein. This switch will hold-off several kilovolts and conduct several kiloamperes when triggered [4]. Two electrodes are present in the spark gap. One electrode is connected to the positively charged high potential plate in the Blumlein. The other electrode is connected to the grounded plate. The electrodes are separated by a short distance and placed in a gas chamber. The chamber's pressure and gas mixture can be varied to change the conditions for triggering. The hold-off voltage of a spark gap is related to the pressure of the gas in the chamber and the distance between the electrodes. A higher value of the product of pressure and distance will enable a higher hold-off voltage for the spark gap. The spark switch connected to the center plate of the Blumlein does not conduct until it is triggered. A focused laser pulse can act as a trigger as illustrated in Figure 4.
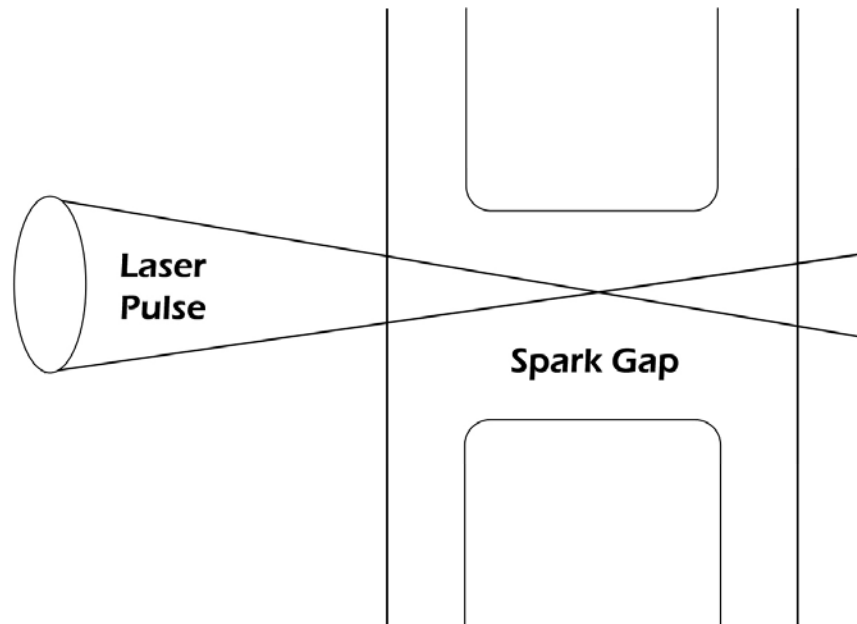
Figure 4 - A laser pulse that acts as a trigger for the spark gap. The laser beam is focused onto the region between the two electrodes in the spark gap.

1.2 Previous Work on Switches and Arc Models

Arc phenomena have been studied since the 1800s. Claudio DeMichelis compiled

a comprehensive review in 1968 that included studies of laser-induced breakdown

mechanisms, plasma expansion, and plasma decay, as well as a bibliography of papers on

the subject. In this paper, two breakdown mechanisms were discussed: multi-

photoionization and cascade ionization. Multi-photon ionization occurs when more than

one photon is absorbed by a gas atom, thus giving an electron more energy than a single

photon alone possesses. The larger energy absorbed makes the ionization of the atom more probable. Cascade ionization occurs when naturally occurring free electrons gain energy from an electric field and collide with an atom, ionizing it and creating another free electron ionizer. Plasma expansion and decay were also addressed in DeMichelis' work. Plasma expansion is caused by intense heating, with the rate of expansion related to the amount of energy deposited into the arc. Plasma decay occurs as electrons recombine with ions when no energy is left in the switch to sustain them. DeMichelis' bibliography contains 161 studies on arc expansion conducted prior to May 1968. [5]

Various types of switches are used in pulse power technology. A thyrotron consists of a tube of low pressure hydrogen gas ignited by a spark. The resulting plasma acts as the conductive path which closes the switch. Ignitrons and liquid metal plasma valves (LMPV) vaporize a pool of Mercury in order to complete the connection. Cross field tubes utilize magnetic fields employed parallel to the electric field to establish collisions in a low pressure gas-filled gap. These collisions lead to a building up of the plasma and breakdown across the gap. Vacuum tubes utilize a thermionic cathode as an electron source. Spark gaps consist of two current-carrying electrodes separated by a gas dielectric. The dielectric is made to breakdown by over-volting the gap, by applying a trigger signal to a third trigger electrode, or with a laser beam [6]. Rail gaps are similar to spark gaps and can also be triggered with an electrical or laser pulse. [7, 8]

Martin Gunderson presented a review work that addressed many different types of switches, including gas-filled spark gaps (the switches investigated in this work). He addresses the fundamental difficulty of modeling switches of this type. The models must incorporate spatial variations of the plasma density and type. Breakdown occurs due to

an over-voltage in the spark gap. This has been addressed by models utilizing streamer mechanisms. Models utilizing a laser trigger to initiate the streamer have also been studied. [9]

A review by E.E. Kunhardt [10] addresses the evolution of the understanding of the electrical breakdown in the pre-breakdown stage. Early work on switch breakdown was known as the Townsend Theory of Breakdown. This theory was later modified into modern streamer theory. Both theories conclude that free electrons are accelerated by the electric field in the gap and collide with background gas atoms to create ion-electron pairs. The electric field is typically established in a gap by a pair of charged electrodes. An avalanche of electrons from multiple collisions forms a streamer plasma. As the streamer becomes more dense, it shields its interior from the electric field in the gap, effectively extending the anode conductor toward the cathode. More electrons move toward the streamer head, creating more plasma, and the streamer grows in the direction of the cathode. This is illustrated in Figure 5. The streamer theory also considers the effect of photoionization in creating more electrons at the head of the streamer. Studies of corona discharges in lower voltage environments, correlate to the streamer theory [11-14]. Examinations of the conducting arc after breakdown have also been performed [15-16]. When the streamer bridges the gap between charged electrodes, current begins to flow through the streamer. An arc grows and becomes less resistive as energy from the current is deposited. Investigators have examined these phenomena in various spark gap experiments [17-25].
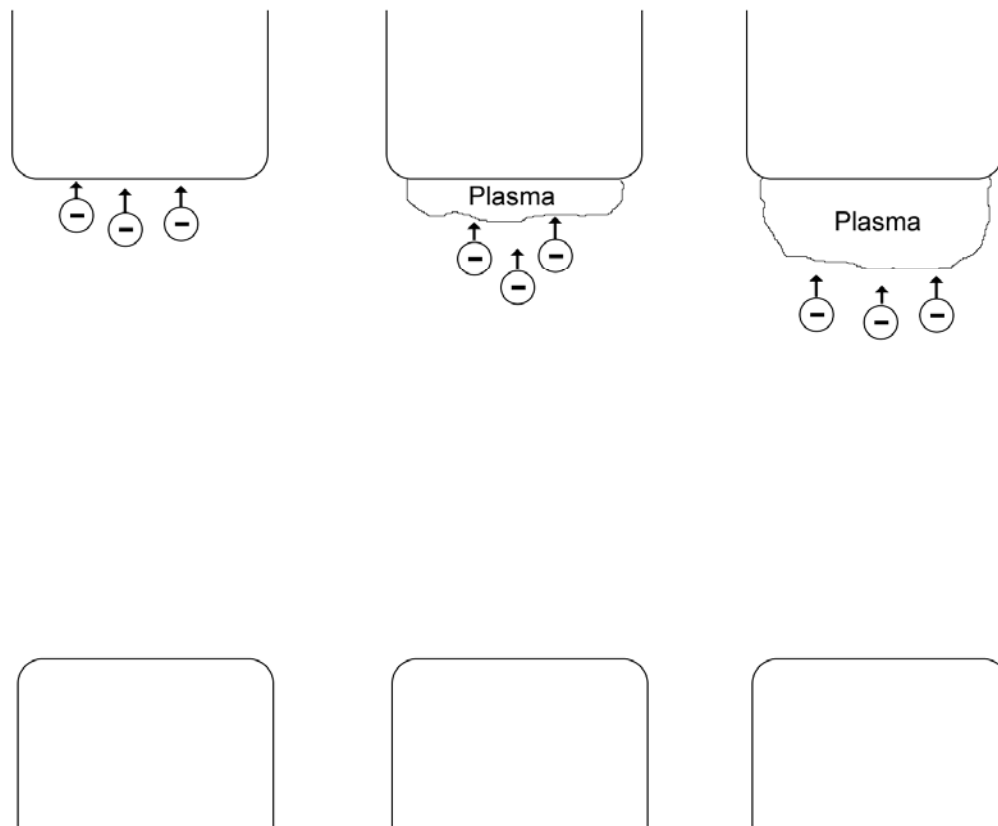
Figure 5 - Electrons build up on the anode over time extending the streamer towards the cathode.

Many models have attempted to relate arc resistance to arc current. Engel [26] takes a comprehensive look at several of these models. Kushner's model [27-28] takes information on gas and thermodynamic processes, kinetic processes, and radiation and incorporates it into a complex model. He compares the model to experimental data, Braginskii's[29] model, and a model by Dabora [30] to illustrate its accuracy. Braginskii's model assumes a constant conductivity for the arc and relates the arc radius to the current. Dabora's model concentrates on measuring the shock wave expansion created by the triggering effect and ensuing current pulse. None of these fluid models

concentrate on the formation of the streamer, and each simply assumes initial conditions from the streamer formation.

Works on pre-breakdown modeling are also available. These models are meant to show a streamer formation via electron-atom collisions [31-32]. A model has been developed by Fowler using fractal branching techniques to look at the global properties of the streamer [33]. The model developed by Pfeiffer utilizes Monte Carlo collision models and represents the streamer as a fluid [34]. Liu utilizes Monte Carlo collision models on individual electrons [35]. Soria has developed a simple particle-in-cell model [36]. Information from models such as these can be utilized to determine the initial conditions for fluid models like those developed by Kushner and Braginskii.

1.3 Project Overview and Objectives

Two models were developed in order to predict the behavior of the spark gap switch. The kinetic model was developed to show streamer formation. From this model, information on plasma density and temperature were determined, as well as the width of the streamer that formed. The kinetic model was run in a particle-in-cell code that is able to simulate the behavior of individual particles and generate new particles according to a defined physics model. The streamer was the initial connection between the high voltage electrode and the grounded electrode in the spark gap, and its properties were used as the initial conditions of the fluid model. The fluid model was developed to determine the properties of the arc as current flows through it and charge is drained from the center plate of the Blumlein. This model was based upon the Blumlein circuit model and the arc model developed by Braginskii. Braginskii's switch model was chosen for

this study because of its simplicity. The simple model was able to more easily show the

effects of changing the experimental parameters affecting the behavior of the spark gap.

The model was utilized to determine the resistance, inductance, and impedance of the

switch over time. The Blumlein investigated consists of two 1 m long by 10 cm wide

transmission lines with a separation of 1mm between the plates. The dielectric separating

the plates has a relative permittivity (ε_r) of 10. This gives the Blumlein a capacitance

of .22 nF and the transmission lines an impedance of 2 Ω each. The load on the line is

therefore 4 Ω. The spark gap electrodes are separated by a 2 mm gap.

This thesis investigates conditions that will accelerate the transition from a high

resistance streamer to a very low resistance arc in a Blumlein switch. A faster resistive

fall time in the arc will lead to a faster, more powerful pulse in the Blumlein load.

Current rise time in the arc is determined by

$$T_{RISE} \approx \sqrt{T_{RESISTIVE}^2 + T_{INDUCTIVE}^2} \tag{3}$$

where $T_{RESISTIVE}$ is the time required for the resistance to fall to a small value compared

to the transmission line impedance. $T_{INDUCTIVE}$ is approximated by

$$T_{INDUCTIVE} \approx \frac{3 \cdot L_{sw}}{Z_L} \tag{4}$$

where L_{sw} is the inductance of the switch and Z_L is the impedance of the load [37].

Since the current rise time in the load is related to the resistive fall time of the arc in the

spark gap, methods of decreasing the resistive fall time in the switches were investigated.

The Braginskii model, utilized to determine the behavior of the arc after the

connection is made and current is flowing, does not exactly correspond to experimental

data [38-39]. However, the model is able to predict the effect of varying several experimental parameters. Therefore, it is possible to use the Braginskii model as a platform for testing changes in particular experimental conditions. The conditions tested in the Braginskii model are the gas density, arc conductivity, and initial arc radius. Gas density can be affected experimentally by changing the pressure in the spark gap or the type of gas used to pressurize the gap. Methods for changing the steady state conductivity in the arc were not investigated. The kinetic model of streamer formation was developed in order to predict the initial radius of the arc. The kinetic model utilized the PIC simulation code, XOOPIC [40] to determine the properties of the streamer. Several conditions were varied in the model to determine the affect on the streamer radius and the conductivity: the pressure in the gap, gas type, electric field generated by the initial voltage, and parameters of the laser pulse used to trigger the gap. These parameters included the area the pulse affected, the orientation of the laser spot, and the laser power. A model of the initiation and growth of the conducting arc in a spark gap can be developed by utilizing the kinetic model in conjunction with the fluid model.

Chapter 1 References

[1]   Blumlein A.D. UK Patent 589127, 1941.

[2]   Somerville I.C., MacGregor S.J., Farish O. "An Efficient Stacked-Blumlein HV Pulse Generator," *Meas. Sci. Technol.,* vol.1, pp 865-868, 1990.

[3]   F. Davanloo, J.L. Korioth, D.L. Borovina, R.K. Krause, C.B. Collins, F.J. Agee, J.H. Hull, L.E. Kingsley, "Stacked Blumlein pulse generators," *Power Modulator Symposium*, pp. 181-185, 1996.

[4]   K. Ujihara., M. Kamiyama, "Triggering of spark gaps by laser-induced ion emission**,"** *IEEE Journal of Quantum Electronics*, vol. 6(4), pp. 239-241, April 1970.

[5]   C., DeMichelis, "Laser Induced Gas Breakdown: A Bibliographical Review," *IEEE Journal of Quantum Electronics*, pp. 188-202, April 1969.

[6]   T. R. Burkes, J.P. Craig, M. O. Hagler, M. Kristiansen, W. M. Portnoy, "A Review of High Powered Switch Technology," *IEEE Transactions on Electron Devices,* vol. 26(10), pp. 1401-1411, October, 1979.

[7]   A. Endoh, S. Watanabe, "Laswer Triggering of a 500-kV Rail-Gap Switch," *J. Appl. Phys.,* vol. 59(10), pp. 3561-3565, May, 1986.

[8]   R.S. Taylor, K.E. Leopold, "UV Radiation-Triggered Rail-Gap Switches," *Rev. Sci. Instrum.* Vol. 55(1), pp. 52-63, January, 1984.

[9]   M.A. Gunderson, "Gas-Phase Pulsed Power Switches," *IEEE Transactions on Plasma Science,* vol. 19, pp. 1123-1131. 1991.

[10]   E.E. Kunhardt, "Electrical Breakdown of Gases: The Prebreakdown Stage," *IEEE Transactions on Plasma Scienc,* vol. 8(3), pp. 130-138, September, 1980.

[11]   J. Chang, P.A. Lawless, T. Yamamoto, "Corona Discharge Process," *IEEE Transactions on Plasma Science,* vol. 19(6), pp. 1152-1166, December, 1991

[12]   R.J. Van Brunt, "Physics and Chemistry of Partial Discharge and Corona," *IEEE Transactions on Dielectrics and Electrical Insulation,* vol. 1(5), pp. 761-784, October, 1994.

[13]   G. J. Roth, M.A. Gunderson, "Laser-Induced Fluorescent Images of NO Distribution After Needle-Plane Pulsed Negative Corona Discharge," *IEEE Transactions on Plasma Science,* vol. 27(1), pp. 28-29, February, 1999.

[14]   E. M. van Veldhuizen, W.R. Rutgers, "Pulsed Positive Corona Streamer Propagation and Branching," *Journal of Physics D: Applied Physics,* vol. 35, pp. 2169-2179, 2002.

[15]   W.D. Kimura, M.J. Kushner, J.F. Seamans, "Characteristics of a Laser-Triggered Spark Gap Using Air, Ar, CH_4, H_2, He, N_2, SF_6 and Xe," *J. Appl. Phys.,* vol. 63(6), pp. 1882-1888, March, 1986.

[16]   C.L.M. Ireland, "A Multichannel Laser Triggered Spark Gap with Subnanosecond Risetime for Electro-Optic Switching," *Journal of Physics E: Scientific Instruments,* vol. 8, pp. 1007-1010, 1975.

[17]   J.R. Woodworth, R.G. Adams, C.A. Frost, "UV-Laser Triggering of 2.8-Megavolt Gas Switches," *IEEE Transactions on Plasma Science,* vol. 10(4), pp. 257-261, December, 1982.

[18]   A. Faltens, L.L. Reginato, R. Hester, A. Chesterman, E.G. Cook, T. Yokota, W. Dexter, "High Repetition Rate Burst-Mode Spark Gap," *IEEE Transactions on Electron Devices,* vol. 26(10), pp. 1411-1413, October, 1979.

[19]   M.F. Rose, M.T. Glancy, "High Repetition Rate Miniature Triggered Spark Switch," *IEEE Transactions on Plasma Science,* vol. 8(3), pp. 139-142, September, 1980.

[20]   H.C. Jarjes, K.H Schonbach, M. Kristiansen, A.H. Guenther, L.L. Hatfield, "Laser Triggering Through Fiber Optics of a Low Jitter Spark Gap," *IEEE Transactions on Plasma Science,* vol. 8(3), pp. 170-176, September, 1980.

[21]   R.A. Petr, T.R. Burkes, "Erosion of Spark Gap Electrodes," *IEEE Transactions on Plasma Science,* vol. 8(3), pp. 149-153, September, 1980.

[22]   H. Watson, "Long-Life High-Repetition-Rate Triggered Spark Gap," *IEEE Transactions on Plasma Science,* vol. 8(3), pp. 154-159, September, 1980.

[23]   A. Ramrus, J. Shannon, "Testing of a 100-kV 100-Hz Rep-Rate Gas Switch," *IEEE Transactions on Plasma Science,* vol. 8(3), pp. 160-162, September, 1980.

[24]   H. Kusama, T. Yagi, "Laster-Triggered Low Timing Jitter Coaxial Marx Generator," *IEEE Transactions on Plasma Science,* vol. 25(6), pp. 1431-1434, December, 1997

[25]   W.R. Rapoport, J. Goldhar, J.R. Murray, "KrF Laster-Triggered SF_6 Spark Gap for Low Jitter Timing," *IEEE Transactions on Plasma Science,* vol. 8(3), pp. 167-170, September, 1980.

[26] T.G. Engel, A.L. Donaldson, M. Kristiansen, "The Pulsed Discharge Arc Resistance and its Functional Behavior," *IEEE Transactions of Plasma Science,* pp. 323-329, vol. 17, April 1989.

[27] M.J. Kushner, R.D. Milroy, W.D. Kimura, "A Laser-Triggered Spark Gap Model," *J. Appl. Phys.,* pp. 2988-3000, vol. 58(8), October, 1985.

[28] M.J. Kushner, W.D. Kumura, S.R. Byron, "Arc Resistance of Laser-Triggered Spark Gaps," *J. Appl. Phys.,* pp. 1744-1751, vol 58(5), September, 1985.

[29] S. I. Braginskii, "Theory of the Development of a Spark Channel," JETP, vol. 34, pp.1548-1557, June 1958.

[30] E.K. Dabora, "Variable Energy Blast Waves," *AIAA Journal,* pp. 1384-1386, vol. 10, October, 1972.

[31] E.H.R Gaxiola, J.M. Wetzer, "Streamers and Transition to Breakdown," *Eleventh International Symposium on High Voltage Engineering,* pp. 11-14, vol. 3, August, 1999.

[32] M. Akram, "The Evolution of Spark Discharges in Gasses: II. The Numerical Solutions of One-Dimensional Models," *J. Appl. Phys.,* vol. 29, pp. 2137-2147, 1996.

[33] H.A. Fowler, J.E. Devaney, J.G. Hagedorn, "Growth Model for Filamentary Streamers in an Ambiant Field," *IEEE Transactions on Dielectrics and Electrical Insulation,* vol. 10(1), pp. 73-79, February, 1993.

[34] W. Pfeiffer, F. Wang, N. Kouzichine, "Simulation of the Formation and Propogation of Streamers in SF_6 and Its Gas Mixtures in Uniform and Non-Uniform Fields," *IEEE International Symposium on Electrical Insulation,* pp. 269-272, September, 2004.

[35] J. Liu, G.R.G. Raju, "Streamer Formation and Monte Carlo Space-Charge Field Calculation in SF6," *IEEE Transactions Electrical Insulation,* pp. 261-170, vol. 28(2), Aprill, 1993.

[36] C. Soria, F. Pontiga, A. Castellanos, "Two-Dimensional Numerical Simulation of Streamers Using a Particle-in-Cell Method," *Conference on Electrical Insulation and Dielectric Phenomena,* pp. 539-542, 2000.

[37] W. C. Nunnally, "Critical Component Requirements for Compact Pulse Power System Architectures," *IEEE Transactions on Plasma Science,* pp. 1262-1267, August, 2005.

[38] T.W. Hussey, K.J. Davis, J.M. Lehr, "Dynamics of Nanosecond Spark-Gap Channels," *12th IEEE International Pulsed Power Conference, Digest of Technical Papers*, vol. 2, pp.1171-1174, June 1999.

[39] T.P. Sorensen, V.M. Ristic, "Rise Time and Time-Dependance Spark-Gap Resistance in Nitrogen and Helium," *J. Appl. Phys*., vol. 48, p. 114, 1977.

[40] J.P. Verboncoeur and A.B. Langdon and N.T. Gladd, "An Object-Oriented Electromagnetic PIC Code," C*omp. Phys. Comm.,* vol. 33, pp. 191-211, May 1995.

Chapter 2

Modeling Setup

In order to understand the switching arc, two models were developed: a kinetic model of streamer development and a fluid model of the arc. The kinetic model was used to study the formation of the streamer to obtain the initial properties of the arc. The fluid model described the switching arc via a discrete element circuit model for the Blumlein and spark gap. The kinetic model results determined the initial streamer radius and conductivity in the switch.   Thus, values obtained from the kinetic model served as initial conditions for the fluid model. Together, these two models described the beginning and end of the life cycle of the arc in the laser triggered gas switch. Environmental parameters and laser triggering parameters were varied to determine the effect on the streamer radius and conductivity in the kinetic model, and the drop in the resistive fall time of the fluid model.

2.1 Kinetic Model Description

The kinetic model was a particle-in-cell (PIC) model, run in the 2D code XOOPIC [1]. The OOPIC kernel was developed to model low to medium density neutral gasses, beams of ionized particles, and electric and electromagnetic fields utilizing a

variety of boundary conditions. Included in the code are several electromagnetic and electrostatic field solvers. The code supports slab (x-y) and cylindrical (r-z) configuration of the 2D simulation space. Rare among other PIC codes is its ability to utilize Monte Carlo collision models to handle the ionization of background gasses. [2]
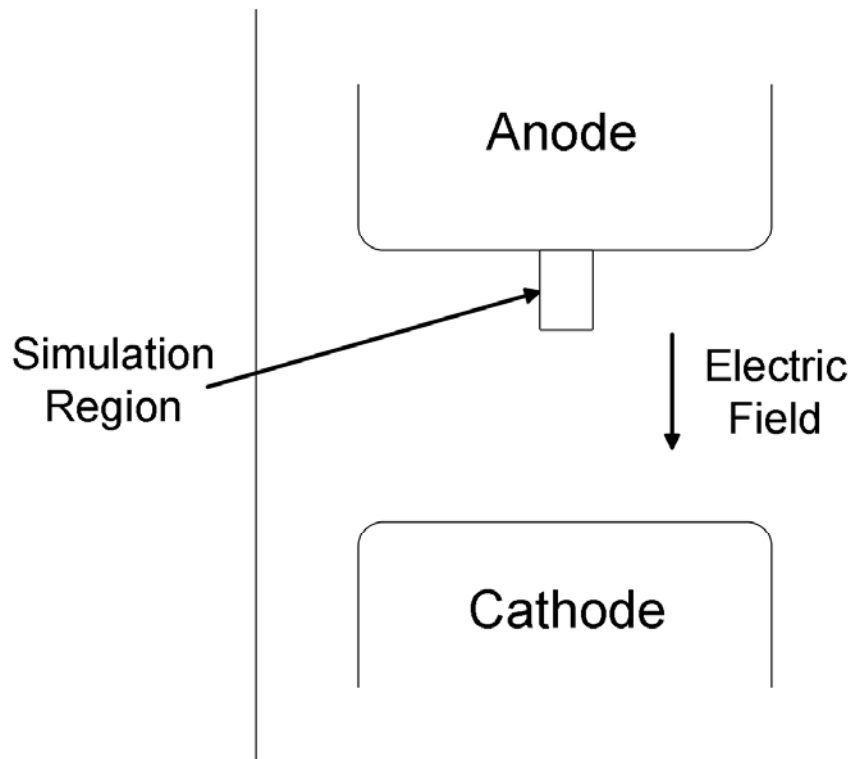
Figure 6 - Simulation space of the kinetic model in a spark gap.

The kinetic model simulated streamer formation in the spark gap. The simulation region of the spark gap was a scaled down version of the actual spark gap: a simple rectangular shape 0.6 mm high and 0.3 mm wide. This region is shown in Figure 6. The size was chosen to be the smallest possible to encompass the entire width of the streamer, but large enough that few electrons escape the sides of the simulation. The top boundary

of the simulation space represented the positive electrode and was modeled as an equipotential boundary with a DC bias of 1200 V to 3000 V. The bottom boundary, which represented the low potential electrode, was modeled as a grounded conductor. These two boundaries established a linear electric field of 2 MV/m to 5 MV/m, respectively. The side boundaries were modeled as a dielectric with a relative permittivity of one in order to simulate a gas dielectric. Argon or Neon at room temperature filled the simulation space at pressures of 1 or 1.5 atm. These conditions represented the intrinsic switch characteristics and were varied to determine the effect on the streamer radius and the streamer conductivity at the end of the simulation time.

Ionization was generated in the switch volume at a fixed rate. The number of electrons generated per time step and their position were defined in the input deck. This rate can either represent the small amount of ionization naturally occurring in the switch space, which facilitates self-breaking, or the amount of ionization generated by a focused UV laser beam. To translate laser power into ionization, it was arbitrarily assumed that 0.5% of all photons ionize a gas atom, thus creating an ion-electron pair in the switch. For example, a 266 nm photon, which falls in the ultraviolet range in the electromagnetic spectrum, has an energy of 4.66 eV. A UV pulse at 15 mJ over 10 ns would contain $2 \cdot 10^{16}$ photons and generate ionized particles at a rate of $1 \cdot 10^{13}$ ns^{-1}. The position at which ionized particles were created in the simulation was manipulated to mimic a focused or expanded laser spot, or to create a linear spot parallel or transverse to the direction of the electric field. The ionization rate was increased to $4 \cdot 10^{13}$ ns^{-1} to indicate a change in laser power from 15 mJ to 60 mJ. These properties of the laser beam pulse

were manipulated to determine trigger laser effects on the streamer at the end of the simulation time.

The simulations were run for 2 ns each to allow a well-developed streamer to form. The time step for the model was 0.1 ns. This was less than $1/(20 f_{plasma})$, where f_{plasma} is the plasma frequency, approximated as $f_p(s^{-1}) \approx 9\sqrt{n(m^{-1})}$. Once the simulation ended, information on position and velocity for each particle in the plasma was used to determine the radius and conductivity of the streamer. The positions of electrons in a sample streamer are shown in Figure 7.
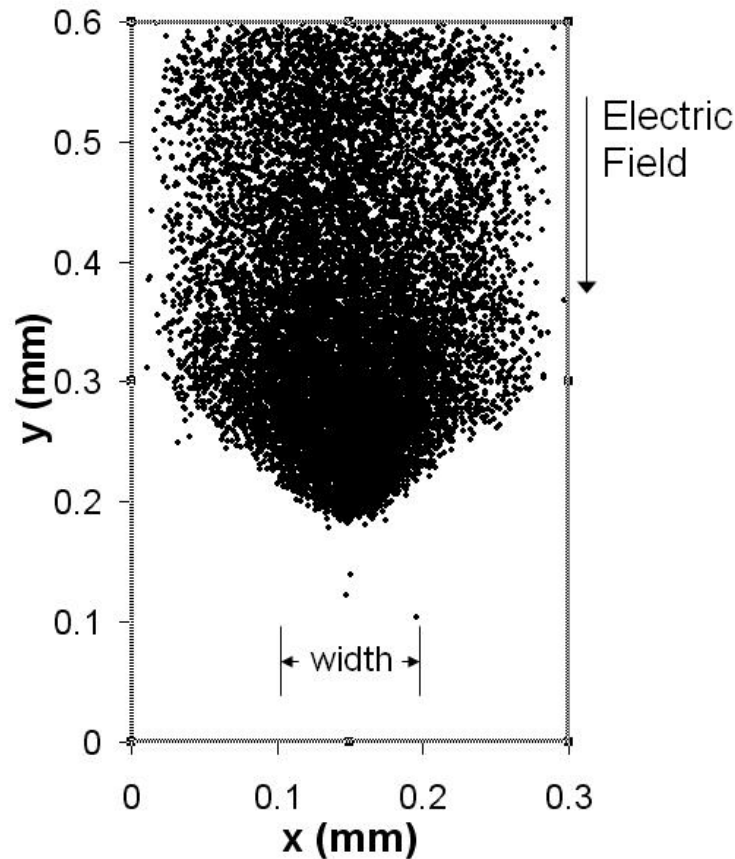
Figure 7 - A cross-sectional image of a sample streamer at simulation end. The entire simulation space is shown. A field of 3 MV/m was applied. The simulation was run for 2 ns at a time step of 0.1 ns with grid dimensions at 512x1028. The electron density is $2.2 \cdot 10^{19}$.

Because the plasma has no easily determined boundary, the radius of the streamer was taken to be the standard deviation of the transverse position of each of the particles relative to the direction of the electric field. The plasma density was determined from the number of particles lying within the defined radius. Electron temperature was determined from the velocity of the particles, where m_e is the mass of the electron and v is the velocity of the particles along the indicated vector.

$$kT_e = \frac{1}{2} m_e (v_x^2 + v_y^2) \tag{2}$$

Conductivity (σ) of the plasma streamer was determined from the electron density (n_e), charge on an electron (e), electron mass (m_e), and collision frequency of the plasma (υ_α) in the following equation.

$$\sigma = \frac{n_e e^2}{m_e \nu_\alpha} \tag{3}$$

The collision frequency component was found from the equation,

$$\nu_\alpha = n_0 \sigma_s (kT_e / m_e)^{\frac{1}{2}} \tag{4}$$

where n_0 is neutral gas density, σ_s is the cross section of the gas, and kT_e is the electron temperature of the plasma.

2.2 Limitations of the Kinetic Model

The number of simulated particles and the size of the mesh are limited by the constraints of computing power. The number of simulated particles should be high to

allow a more fluid streamer to form. A value of 10^6 real particles per simulated particle was found to give acceptable results. The number of particles per simulation ranged from 60,000 to 250,000. The 10^6 ratio between real particles and simulated particles was required to keep this number manageable.

The number of grids must be large so that space between mesh points is small enough to resolve the Debye length of the plasma. The Debye length is the width of the surrounding sheath needed to shield out all applied electric fields,

$$\lambda_D = \left(\frac{\varepsilon_0 k T_e}{n_e e^2} \right)^{1/2}$$

(5)

where ε_0 is the relative permeability, k is Boltzman's constant, T_e is the electron temperature, n is the electron density and e is the charge on an electron. A highly refined mesh is required to resolve the Debye length of the plasma. The kinetic model utilized 512 grids horizontally and 1024 grids vertically in the simulation space of 0.3 mm by 0.6 mm. This provided a grid size of approximately 0.5 μm. The minimum Debye length observed was greater than 1 μm, so the grid size was chosen to be at least twice the Debye length in every simulation. Simulations run with the grid size greater than the Debye length produced an artificial heating effect that would lead the simulation to crash after a period of time.

The electric field in the simulations was scaled down from the originally desired 10 MV/m field established by the 20 kV charge across the 2 mm gap of the switch. This is because higher electric fields generated more dense plasmas, decreasing λ_D to a value unresolved by the established mesh. The scaled gap length of 0.6 mm was large enough to allow a well-developed streamer to form. The simulation width of 0.3 mm was large

enough to encompass the width of the streamers that were simulated. More computing

power is required to simulate the number of particles required in the entire switch at the

required mesh size.

Another limitation of the model was that XOOPIC is only packaged with code to

determine collisions between noble gasses such as Argon and Neon. Many gas-filled

spark gaps are filled with gas mixtures such as dry air, which contains primarily Nitrogen,

Oxygen, Carbon Dioxide and Argon. Also, complex molecules such as SF_6 are

sometimes used.   A collision model using these different types of gasses would require

finding an acceptable collision model for the gasses and incorporating it into the

XOOPIC code. The choice was made to go ahead with simulations using Argon and

Neon in order to determine effects of the changing the gas type and other parameters. It

was assumed that many effects will be similar for other gasses commonly used in spark

gaps.

2.3 Fluid Model Description

The fluid model was developed to predict the behavior of the conducting arc after

the streamer makes a connection between the two electrodes. The arc becomes a very hot,

dense plasma due to the energy dissipated in by the current. Energy from the current also

causes the arc to expand. As the arc expands and heats up, the resistance of the arc drops

drastically. The resistance fall time is of key importance to increasing the power in the

Blumlein load.

The fluid model of the arc was developed based on the model derived by

Braginskii [3] and further investigated by Hussey [4]. Braginskii proposed that all energy

from the current goes into channel expansion and conductivity remains constant. He

related the radius of the streamer to the current, where a is the radius, ρ_0 is the gas density,

σ is conductivity, ξ is an experimentally derived constant equal to 4.5, and I is the current.

One added parameter is a_0, which represents the initial radius of the streamer from the

kinetic model.

$$a^2(t) = a_0{}^2 + \left(\frac{4}{\pi \rho_0 \xi \sigma}\right)^{\frac{1}{3}} \int I^{\frac{2}{3}} dt \tag{6}$$

Note that σ in equation (1) is the fully developed arc conductivity, not the streamer

conductivity from the kinetic model.

The radius of the streamer directly relates to its resistance: d is the length of the

streamer and R is the resistance. Also, the inductance of the streamer is given, where a_{cr}

is the current return radius and L is inductance.

$$R(t) = \frac{d}{\sigma \pi a^2(t)} \tag{7}$$

$$L(t) = 2 \times 10^{-7} d \ln\left(\frac{a_{cr}}{a(t)}\right) \tag{8}$$

A circuit model of the Blumlein and switch was developed using the Braginskii

model for the spark gap parameters shown in Figure 8. The Blumlein transmission lines

were modeled as a series of four capacitors and inductors, each having a value of one-

quarter the total capacitance and inductance of the line. The Blumlein load was modeled

as a pure resistance that matches the total impedance of the two transmission lines. The

switch was modeled as a variable resistance and inductance as described by equations (7)

and (8), which were recursively resolved as the current through the switch changed. The inductance of the spark gap includes 100 nH which accounts for the change in area from the plate to the small electrode of a spark gap.
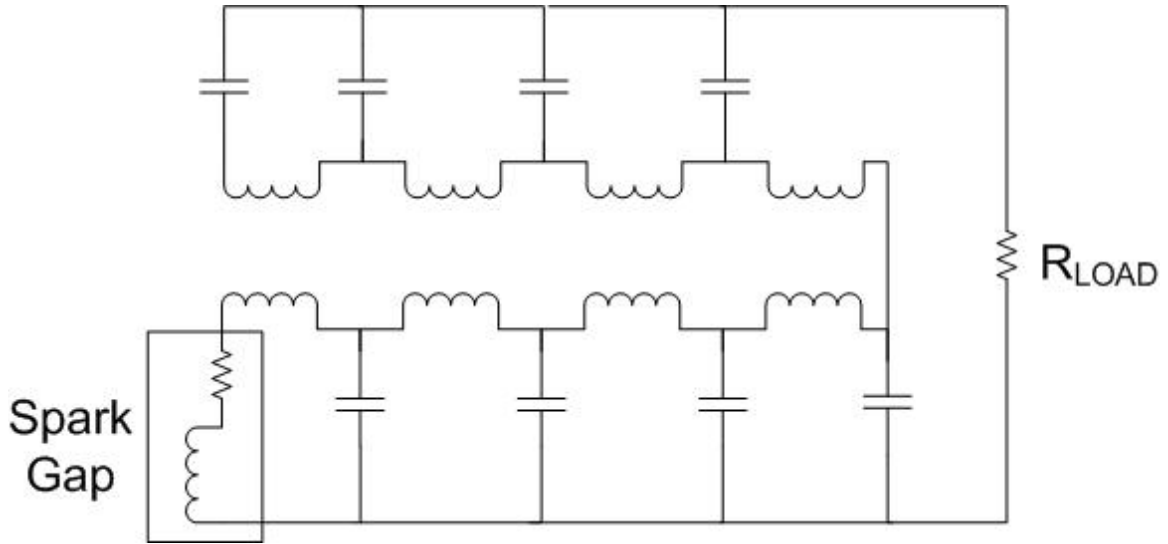
Figure 8 - The circuit model of the Blumlein system. The transmission lines are modeled as a series of 4 capacitors and inductors. The spark gap is modeled as a time dependant resistance and inductance in series. The Blumlein load is matched to the sum of the impedance of the two transmission lines.

The Blumlein investigated is made up of two transmission lines, each 1 m long and 10 cm wide, with a separation of about 1.5 mm between the plates. The dielectric separating the plates has a relative permittivity (ε_r) of 10. This gives the Blumlein a capacitance of 14 nF and the transmission lines an impedance of 2 Ω each. The load on the line is therefore 4 Ω.

A series of differential equations that describe the behavior of the voltage at each node and the current through each loop were solved based on the initial voltage of 20 kV and zero current through the switch. A solution for current over time was found and used to find the radius of the streamer over time from equation (6). Resistance and inductance of the arc was then found from equation (7) and (8).

The gas density, the conductivity, and the initial radius were varied to examine the effect on the resistive fall time. A change in gas density was accomplished in one of two ways: increasing the gas pressure or changing the gas type to a heavier gas. Neon at 1 atm has a density of 0.90 kg/m^3 and a density of 2.70 kg/m^3 at 3 atm. Argon at 1 atm has a density of 1.78 kg/m^3, and a density of 5.35 kg/m^3 at 3 atm. The values for initial radius used (10 μm, 35 μm, and 60 μm) were meant to encompass the range of radii that are found in the kinetic model. Conductivity values that were chosen were 10,000 mho/m, 20,000 mho/m, and 30,000 mho/m, corresponding to values proposed by Braginskii and Martin [5].

2.4 Limitations of the Fluid Model.

One limitation to the fluid model is with regard to the assumptions made about the expanding shock wave created by the arc. Braginskii assumes that the expansion velocity is approximately constant. In order for this to be true, the gas density and conductivity must be constant. A constant gas density implies that the pressure also must remain constant. An assumed constant conductivity requires a constant temperature and density. In order to maintain a constant density in the arc, mass from the shocked region must be constantly injected into the channel. These assumptions allowed Braginskii to develop a simple mathematical formula relating arc radius to arc current. Any deviations in these values that might occur in a real spark gap would introduce an error into the model.

Another limiting factor of the fluid model was determining transition from the streamer conductivity found in the kinetic model to the arc conductivity utilized by the fluid model. While the streamer conductivity is the initial condition for the arc,

26

measuring the increase in conductivity from streamer to arc was beyond the scope of this

work. The fluid model utilized the streamer radius as the initial arc radius, but did not

take into account the streamer conductivity. Braginskii's equation assumes a constant,

high, conductivity throughout the arc. This equation must be rederived in order to

incorporate the effect a changing conductivity has on the arc. The result of this

inconsistency was that the resistance of the arc in the initial stages of the arc formation

was less than what would be observed in the laboratory. However, the adjustments of the

experimental values did still show the effect they have on the resistance of the arc.

Chapter 2 References

[1] J.P. Verboncoeur and A.B. Langdon and N.T. Gladd, "An Object-Oriented Electromagnetic PIC Code," C*omp. Phys. Comm.,* vol. 33, pp. 191-211, May 1995.

[2] OOPIC Pro User's Guide version 1.0.

[3] S. I. Braginskii, "Theory of the Development of a Spark Channel," JETP, vol. 34, pp.1548-1557, June 1958.

[4] T.W. Hussey, K.J. Davis, J.M. Lehr, "Dynamics of Nanosecond Spark-Gap Channels," 12th IEEE International Pulsed Power Conference, Digest of Technical Papers, vol. 2, pp.1171 – 1174, June 1999.

[5] T.H. Martin, J.F. Seamen, D.O. Jobe, "Energy Losses in Switches," *Proceedings of the 1993 IEEE Pulsed Power Conference,* p. 463, 1993.

Chapter 3

Kinetic Model Results

3.1 Overview of Results for Kinetic Model

The kinetic model was used to determine the parameters that most affected the conductivity and the radius of the streamer. A higher electric field resulted in an increase in both streamer radius and conductivity in all simulations. A change from Argon to Neon resulted in a significant decrease in streamer conductivity, but little change in streamer radius. An increased pressure in the spark gap had a negligible effect on both radius and conductivity. A linear laser spot oriented transverse to the electric field resulted in a larger radius when the area of the laser spot was large. When the laser spot was small, the reorienting had a less dramatic effect. Laser power had little effect on either the conductivity or the radius of the streamer.

Radius	Electric Field	Pressure	Gas Type
Electric Field	Yes		
Pressure	No	No	
Gas Type	Yes	No	No

Conductivity	Electric Field	Pressure	Gas Type
Electric Field	Yes		
Pressure	No	No	
Gas Type	Yes	No	No

Table 1 - Overview of the effect of the intrinsic switch parameters on the streamer radius in the kinetic model. A 'Yes' indicated that there was a large effect of the vertical and horizontal parameters; identical intersection fields denote that it had a large single parameter effect. A 'Yes' in other intersection fields denote that a large effect was observed when the parameters were varied in conjunction.

Radius	Spot Orientation	Spot Area	Laser Power
Spot Orientation	No		
Spot Area	Yes	No	
Laser Power	No	No	No

Conductivity	Spot Orientation	Spot Area	Laser Power
Spot Orientation	No		
Spot Area	No	No	
Laser Power	No	No	No

Table 2 - Overview of the effect of the laser triggering parameters on the streamer radius in the kinetic model. A 'Yes' indicated that there was a large effect of the vertical and horizontal parameters; identical intersection fields denote that it had a large single parameter effect. A 'Yes' in other intersection fields denote that a large effect was observed when the parameters were varied in conjunction.

3.2 Process for Exploring Intrinsic Switch Parameter Variances

The intrinsic switch parameters are steady state characteristics of the switch. These parameters are the electric field across the gap, the pressure in the spark gap, and the type of gas used in the spark gap. Changing the electric field was accomplished by changing the charge voltage on the equipotential boundary. This value was varied from 1200 V to 3000 V, resulting in an electric field change from 2 MV/m to 5 MV/m. Changing the pressure was accomplished by varying the pressure parameter in the Monte Carlo collision section of the input deck. Changing the gas type parameter consisted of changing the ion mass and cross-section set. Ionization was simulated via a constant volumetric generation at a rate of 10 simulated particles, each representing 10^6 real particles, per time step over an area encompassing the entire length and the middle 40% of the width of the switch. This generation mimics breakdown in the switch. The rate of pair generations was roughly $7 \cdot 10^{25}$ s^{-1}, to provide an even distribution of ionization throughout the simulation space.

Twenty-eight different combinations of pressure, electric field, gas type were simulated. Each simulation setup was run ten times with a different seed for the random number generator. This resulted in a total of 280 simulations. The variation of the random number seed provided a variety of results under the same initial conditions. The raw set of data can be seen in Appendix III. The following figures show the effects of changing the intrinsic parameters using the average of the 10 simulations run. The error bars indicate the range of the data that was observed.

The code produces an output file that contains data on horizontal and vertical position as well as velocity along the x, y, and z vectors. To convert these values into

radius, density and temperature data, a specialized program was developed (see Appendix II). The data was first converted into comma separated tables. Then, a C-program performed computations on the data to determine the radius, density, temperature, and number of particles in the simulation.

3.3 Results of Intrinsic Switch Parameter Variances

3.3.1 Experimental Variation Effects on Radius

Figure 9 shows an overview of the effects changing the electric field, gas type, and pressure had on the radius of the streamer. A gradual increase in the streamer radius due to an increasing electric field from 2 MV/m to 5 MV/m is shown. The increase in the streamer radius is more gradual for Neon than it is for Argon. A pressure change from 1 atm to 1.5 atm does not have any significant effect.
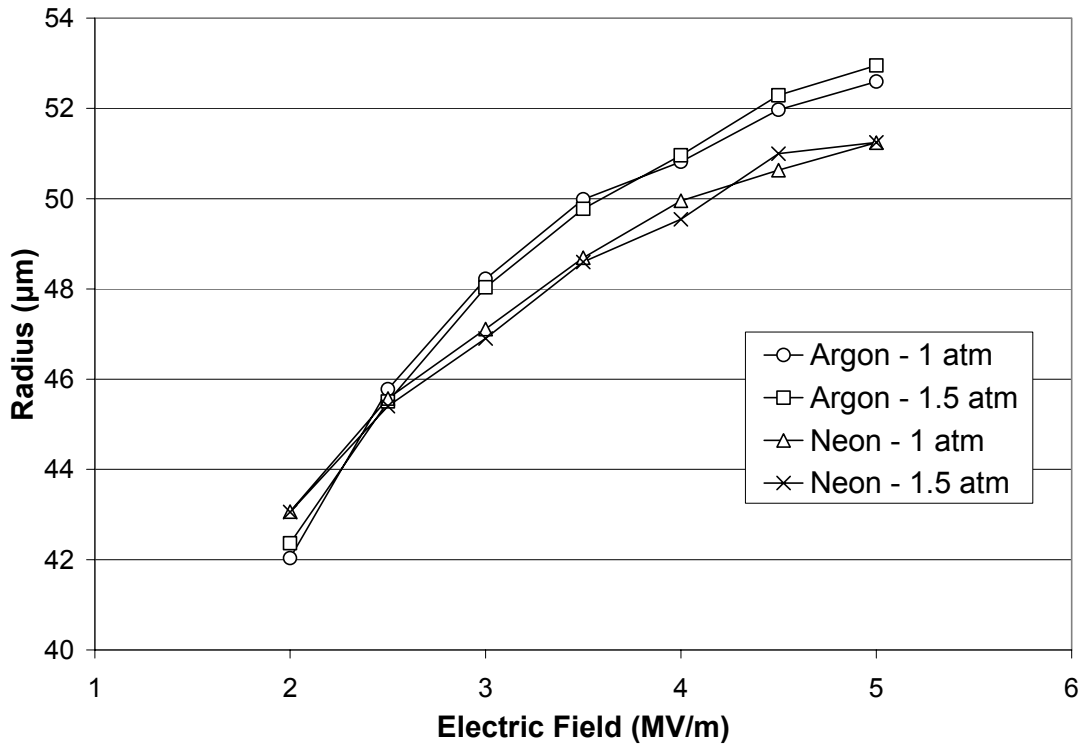
Figure 9 - Resulting streamer radii due to a change in the electric field from 2 MV/m to 5 MV/m at 0.5 MV/m intervals. The simulation sets were run for four different gas type and gas pressure combinations and simulated self-break of the spark gap. The plot points represent the mean results of 10 simulations.

Increasing electric field had a significant affect on both the conductivity and streamer radius in each instance. For example, increasing the electric field from 2 MV/m to 5 MV/m in a spark gap filled with Argon at 1 atm resulted in the streamer radius increasing 25% overall, from 42.03 μm to 52.60 μm. The effect of changing the electric field when the Argon gas was replaced by Neon gas, keeping the pressure at 1 atm is that radius increased 19%, from 43.06 μm to 51.24 μm.

The effect of varying the type of gas used to pressurize the spark gap was examined in the next set of simulations. The streamer radius in these simulations underwent a slight, but insignificant, increase in each occasion when switching from Neon gas to Argon gas at electric fields greater than 3 MV/m. The streamer radius

increased 2%, from 47.11 μm to 48.22 μm, with an electric field of 3 MV/m. A field of 4

MV/m caused a change in the gas type to yield a streamer radius increase of 2%, from

49.96 μm to 50.82 μm, when switching from Neon to Argon. At lower electric field

strength, a change in gas type had the opposite effect on the streamer radius. Streamer

radius decreased 2% from 43.06 μm to 42.03 μm when changing gas types from Neon to

Argon with an electric field of 2 MV/m.

The simulations showed that changing the background gas pressure from 1 atm to

1.5 atm did not significantly affect streamer radius. The radius at 1 atm was 48.22. The

radius at 1.5 atm was 48.04 μm. This is a decrease in radius of less than 1%. The electric

field for these simulations was 3 MV/m and the gas fill type was Argon. Streamer radius

adjusted slightly from 50.82 μm to 50.96 μm, a less than 1% decrease with an electric

field of 4 MV/m. Switching the background gas to Neon rather than Argon did nothing

to affect the significance of varying the background pressure. With an electric field of 3

MV/m, changing the pressure resulted in a slight change in streamer radius from 47.11

μm to 46.90 μm. With an electric field of 4 MV/m, the pressure change resulted in a

radius change from 49.96 μm to 49.54 μm: a 1% increase.

3.3.3 Experimental Variation Effects on Conductivity

Figure 10 shows an overview of the effects changing the electric field, gas type,

and gas pressure had on the conductivity of the streamer. An increase in electric field

from 2 MV/m to 5 MV/m had a large effect on the conductivity due to an increase in the

plasma density. Changing gas type from Neon to Argon also increased the conductivity

significantly due to a decrease in the electron temperature. A change in pressure from 1 atm to 1.5 atm had a negligible effect on the conductivity.

Increasing electric field had a significant affect on the conductivity. Increasing the electric field from 2 MV/m to 5 MV/m in a spark gap filled with Argon at 1 atm resulted in conductivity increasing 285%, from 1.06 mho/m to 4.08 mho/m. Changing the electric field when the Argon gas was replaced by Neon gas, keeping the pressure at 1 atm resulted in conductivity increasing 394%, from 0.67 mho/m to 3.31 mho/m. The change in conductivity here is associated with a change in density. Higher electric fields produced more dense streamers in the simulations.

The conductivity of the streamer showed a significant increase when switching from Neon gas to Argon gas. When the electric field across the gap is 3 MV/m and the pressure is 1 atm, the conductivity increased 53%, from 1.48 mho/m to 2.26 mho/m. An electric field to 4 MV/m while keeping the pressure at 1 atm caused a change in the gas type to yield an increase in conductivity of 49%, from 2.37 mho/m to 3.52 mho/m. Conductivity changes here are attributed to the change in electron temperature. The electron temperature for all simulations involving Argon as the background gas was around 2.9 eV while all simulations involving Neon as the background gas was around 4.0 eV.

Figure 10 - Resulting streamer conductivities, densities, and electron temperatures due to a change in the electric field from 2 MV/m to 5 MV/m at 0.5 MV/m intervals. The simulation sets were run for four different gas type and gas pressure combinations and simulated self-break of the spark gap. The plot points represent the mean results of 10 simulations.

The changes in pressure from 1 atm to 1.5 atm resulted in nearly no change in streamer conductivity. The conductivity at 1 atm was 2.26 mho/m. The radius at 1.5 atm was 48.04 μm and the conductivity was 2.27 mho/m. This is an increase in conductivity of less than 1%. The electric field for these simulations was 3 MV/m and the gas fill type was Argon. Conductivity remained nearly constant around 3.50 mho/m with an electric field of 4 MV/m. Switching the background gas to Neon rather than Argon again did nothing to affect the significance of varying the background pressure. With an electric field of 3 MV/m, changing the pressure resulted in conductivity remaining constant at 1.50 mho/m. With an electric field of 4 MV/m, conductivity increased by less than 1%, from 2.37 mho/m to 2.42 mho/m.

3.4 Statistical Analysis of Intrinsic Switch Parameter Results

Regression Statistics	
Multiple R	0.9451
R Square	0.8932
Adjusted R Square	0.8904
Standard Error	1.0870
Observations	280

ANOVA

	df	SS	MS	F	Significance F
Regression	7	2686.9629	383.8518	324.8772	4.0346E-128
Residual	272	321.3759	1.1815		
Total	279	3008.3388			

	Coefficients	Standard Error	t Stat	P-value	Lower 95%	Upper 95%
Intercept	38.3652	1.2100	31.7072	0.0000	35.9830	40.7473
Electric Field	2.8266	0.3312	8.5338	0.0000	2.1745	3.4787
Pressure	-0.6321	0.9458	-0.6683	0.5045	-2.4942	1.2300
Gas Type	-0.9645	0.4018	-2.4008	0.0170	-1.7555	-0.1736
Random Seed	0.0336	0.0226	1.4859	0.1385	-0.0109	0.0781
Field – Pressure Interaction	0.1792	0.2598	0.6897	0.4910	-0.3323	0.6908
Pressure – Type Interaction	0.1429	0.2598	0.5498	0.5829	-0.3687	0.6544
Field – Type Interaction	0.3395	0.0650	5.2266	0.0000	0.2116	0.4674

Table 3 - Regression statistics for radius in relation to intrinsic switch parameters.

Table 3 shows the regression analysis for the radius given the intrinsic switch parameters that were varied in the previously discussed simulations. The regression analysis helps to identify parameters that produce a statistically significant change in the results when their value is varied. It is assumed that a P-value less than 5% is a significant effect on the radius of the streamer. Given the regression data, electric field and gas type both have a significant effect on the streamer radius. Also, the interaction

between the two has a significant effect. Gas pressure in the switch did not have a

significant effect on the radius.

	Regression Statistics
Multiple R	0.9969
R Square	0.9938
Adjusted R Square	0.9936
Standard Error	0.0915
Observations	280

ANOVA

	df	SS	MS	F	Significance F
Regression	7	363.2453	51.8922	6192.9340	8.3192E-296
Residual	272	2.2792	0.0084		
Total	279	365.5244			

	Coefficients	Standard Error	t Stat	P-value	Lower 95%	Upper 95%
Intercept	-1.1982	0.1019	-11.7591	0.0000	-1.3988	-0.9976
Electric Field	1.0324	0.0279	37.0124	0.0000	0.9775	1.0873
Pressure	-0.0038	0.0797	-0.0479	0.9619	-0.1606	0.1530
Gas Type	-0.0443	0.0338	-1.3084	0.1918	-0.1109	0.0223
Random Seed	-0.0043	0.0019	-2.2751	0.0237	-0.0081	-0.0006
Field - Pressure Interaction	0.0031	0.0219	0.1396	0.8891	-0.0400	0.0461
Pressure -Type Interaction	-0.0135	0.0219	-0.6178	0.5372	-0.0566	0.0296
Field - Type Interaction	0.1459	0.0055	26.6714	0.0000	0.1351	0.1567

Table 4 - Regression statistics for conductivity in relation to intrinsic switch parameters.

Table 4 shows the regression analysis for conductivity in relation to the intrinsic switch variables. Electric field and its interaction with gas type had a significant effect on the conductivity of the streamer. Neither gas type nor pressure had significant independent effect on the conductivity.

3.5 Process for Exploring Triggering Laser Pulse Parameter Effects

The effects of varying the parameters of the laser pulse used to trigger the spark gap were explored by modifying the rate, shape, and area of the generated ionization in the simulations. An increase in generation rate simulated an increase in the power of the triggering laser pulse. Simulated laser power was varied between a 15 mJ pulse and a 60 mJ pulse lasting 10 ns each. A decrease in the generation area simulated a focusing of the triggering laser pulse. Four spot areas were examined. The spot areas were 1200 μm^2, 2400 μm^2, 3600 μm^2, and 4800 μm^2. Changing the shape of the genaration area simulated reorientation of the laser pulse shape. The triggering beam in both cases was a linear spot, which was oriented both parallel and transverse to the electric field. The parallel spots were 0.4 mm, 0.3 mm, 0.2 mm, and 0.1 mm long with width of 12 μm. The transverse spots were 0.05 mm, 0.10 mm, 0.15 mm, and 0.20 long with width of 24 μm. Each spot was centered within the simulation space.

Each combination of parameters was run 10 times to obtain a number of results for the streamer radius and conductivity. The electric field in the spark gap for each simulation was 3 MV/m. The gap was pressurized by 1 atm of Argon gas. These parameters were not varied in the simulations. Information on streamer radius, density and electron temperature was obtained in a similar manner as previously mentioned.

3.6 Results of Triggering Laser Pulse Parameter Variances

3.6.1 Experimental Variation Effects on Radius

Figure 11 shows an overview of the effects of varying the triggering laser pulse parameters had on the radius of the streamer. Laser spot area is shown to have a large effect on the radius when the linear spot is oriented transverse to the electric field. When the spot is parallel to the electric field, there is a negligible effect. A small effect from increased laser pulse energy is also illustrated. Figure 12 illustrates how the reorientation of the laser was accomplished. The transverse beam with a large spot area had, by far, the greatest effect on changing the streamer radius than any other change made during this study.
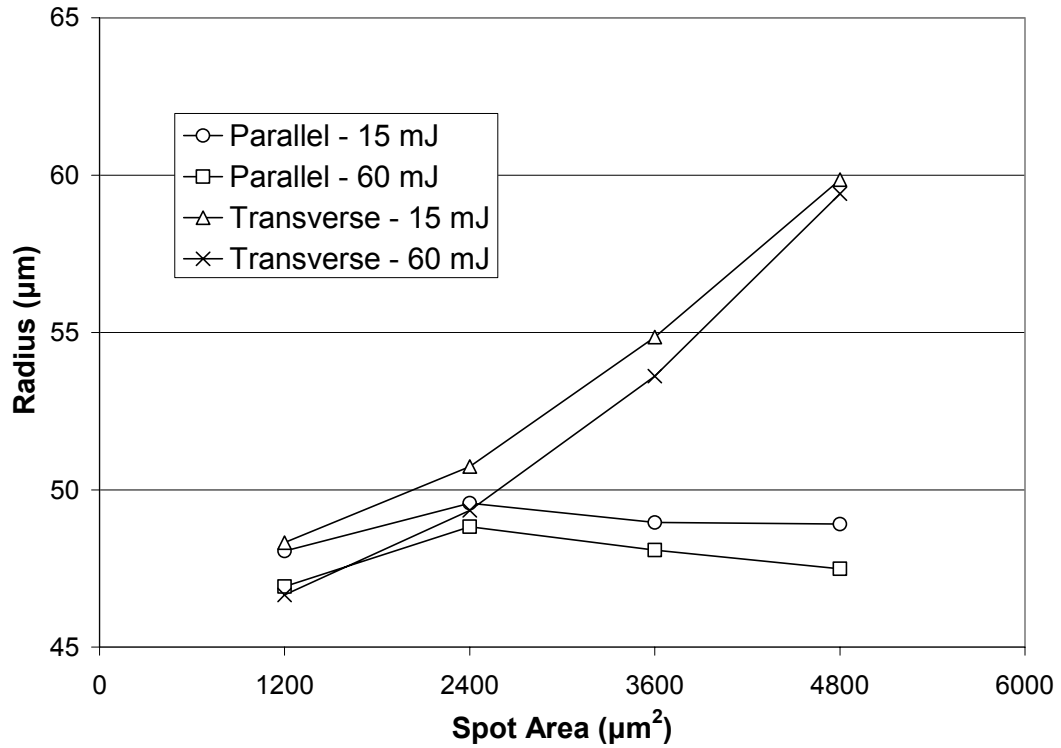
Figure 11 - Resulting streamer radii due to a change in the laser spot area from 1200 µm^2 to 4800 µm^2. The simulation sets were run for 4 different combinations of laser spot orientation and laser pulse energy and simulate a triggered breakdown in the spark gap. The plot points represent the mean results of 10 simulations.
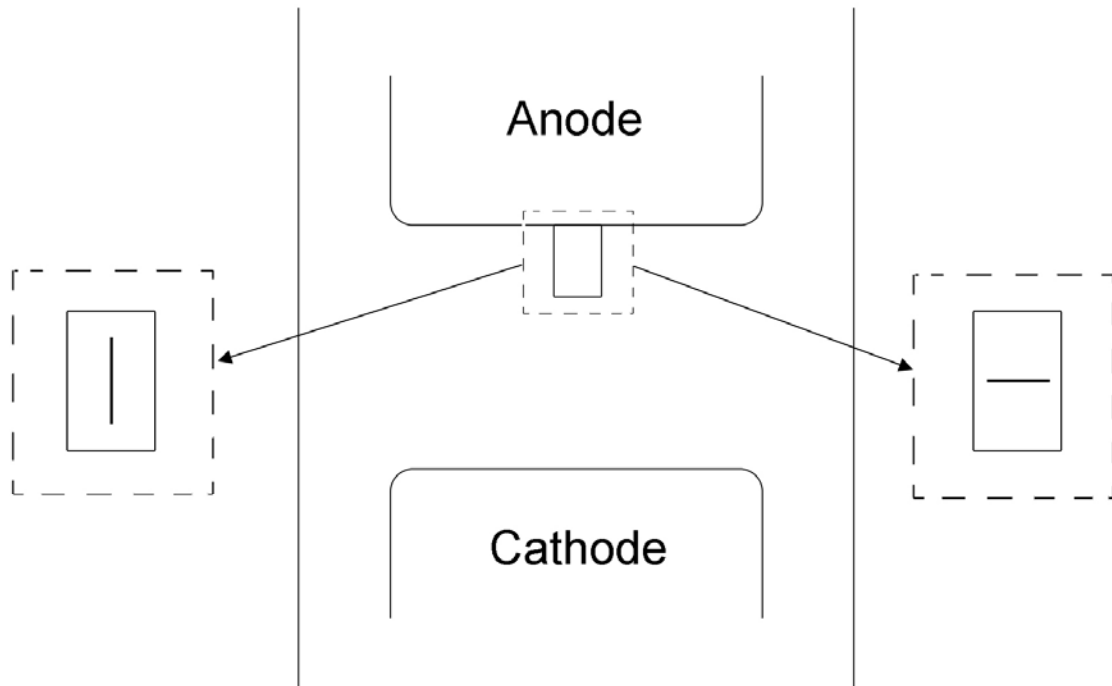
Figure 12 - Illustration of reorienting the laser pulse from a linear spot parallel to the electric field to a linear spot transverse to the electric field.

Shifting the triggering pulse from a linear spot 0.4 mm high and 12 μm wide, an area of 4800 μm², parallel to the electric field, to a linear spot 0.2 mm wide and 24 μm high transverse to the electric field yielded a 22% increase in streamer radius, from 48.91 μm to 59.86 μm. The pulse had a simulated laser power of 15 mJ. Focusing the two beams into a smaller area by shrinking the length of the spot practically negated any effect of reorienting the beam. The streamer radius increased only slightly, from 49.57 μm to 50.74 μm, an increase of 2%.

The effect of focusing the laser pulse into a smaller spot was seen in the next set of simulations. The beam varied in area from 1200 μm² to 4800 μm². Each set of

simulations was run with a laser pulse power of 15 mJ with a linear spot oriented parallel to the electric field. Increasing the area slightly decreased the streamer radius 3%, from 49.57 μm to 48.03 μm.   Reorienting the linear spot to be transverse to the electric field greatly affected the streamer radius. Widening the beam across the gap resulted in an increase of the streamer radius by 18%, from 50.74 μm to 59.86 μm.

Laser pulse energy did not have a large effect on the streamer radius. The simulated laser pulse was increased in power from 15 mJ to 60 mJ over a 10 ns pulse length. A 5% decrease, from 49.81 μm to 47.49 μm, in the value of the streamer radius resulted from changing laser pulse energy in the long laser pulse parallel to the electric field. Radius decreased 2%, from 49.57 μm to 48.83 μm in a more focused beam with an area of 2400 μm^2. The laser power had practically no effect on the laser pulses oriented transverse to the electric field. The streamer generated by the wider spot increased in radius by less than 1%, from 59.41 μm to 59.86 μm. Increasing the power in the more focused spot resulted in a 3% decrease in the streamer radius, from 50.74 μm to 49.35 μm, while holding the conductivity steady around 2.21 mho/m.

3.6.2 Experimental Variation Effects on Conductivity

Figure 13 shows an overview of the effect the triggering laser properties have on the conductivity, density, and temperature of the streamer. The graph shows that the conductivity is slightly affected by changes in spot area, laser pulse energy, and orientation of the linear laser pulse. Increasing the laser spot area for spots parallel to the electric field will slightly increase the conductivity for pulse energies of 15 mJ and 60 mJ, while decreasing conductivity for linear beams oriented transverse to the electric field in

the switch. All conductivity changes are due to a change in density because laser trigger

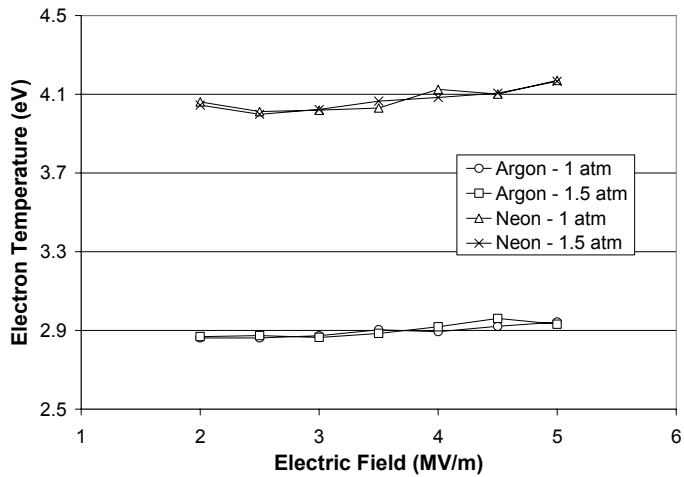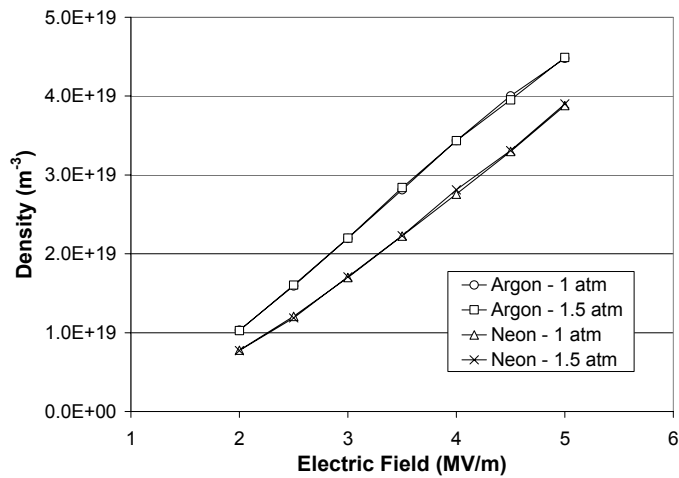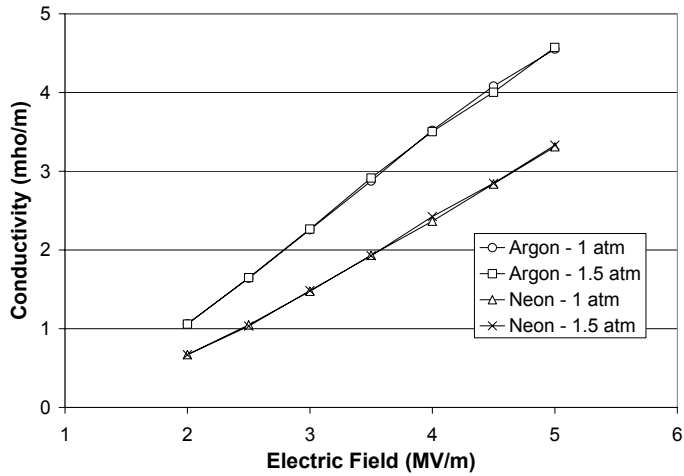parameters did not have an effect on the electron temperature.
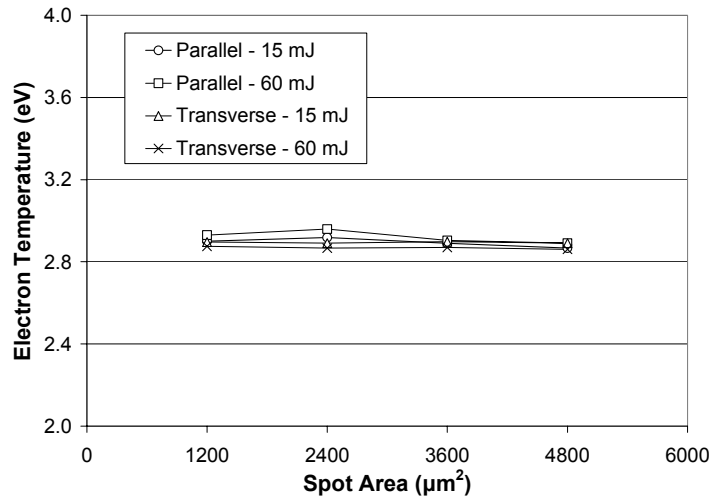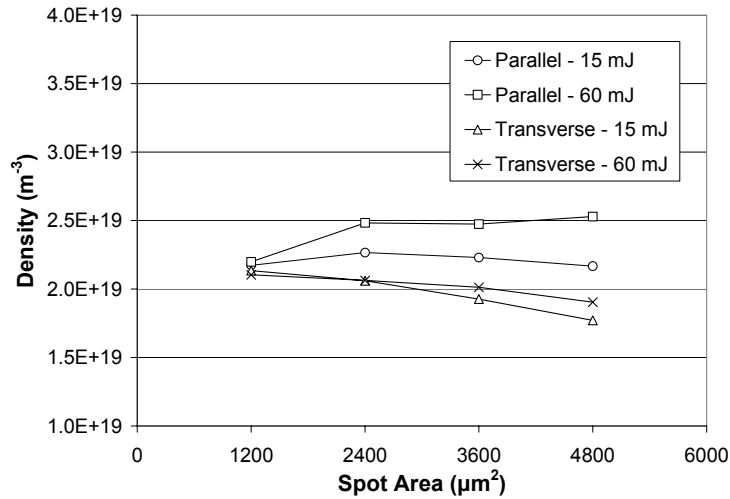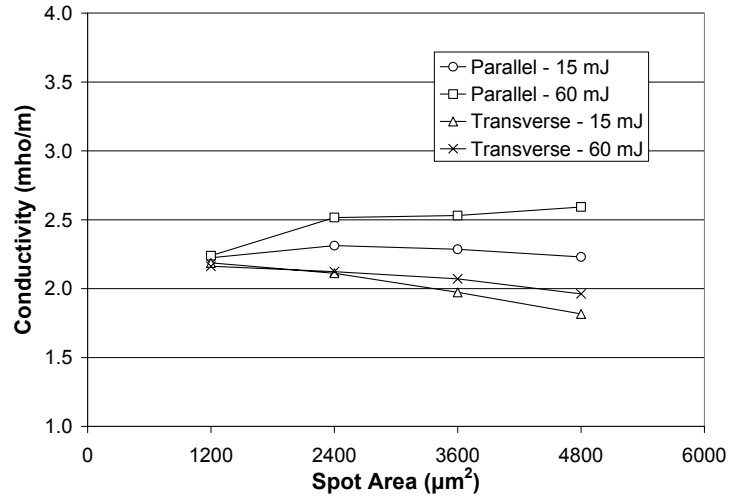
Figure 13 - Resulting streamer conductivities, densities, and electron temperatures due to a change in the laser spot area from 1200 μm² to 4800 μm². The simulation sets were run for 4 different combinations of laser spot orientation and laser pulse energy and simulate a triggered breakdown in the spark gap. The plot points represent the mean results of 10 simulations.

Shifting the triggering pulse from a linear spot 0.4 mm high and 12 μm wide, an area of 4800 μm^2, parallel to the electric field, to a linear spot 0.2 mm wide and 24 μm high transverse to the electric field resulted in significant changes. This adjustment yielded a 23% decrease in streamer conductivity, from 2.23 mho/m to 1.82 mho/m. The pulse had a simulated laser power of 15 mJ. Focusing the two beams into a smaller area by shrinking the linear length of the spot practically negated any effect of reorienting the beam. The conductivity was also less affected, decreasing 5% from 2.31 mho/m to 2.21 mho/m.

Increasing the spot area from 1200 μm^2 to 4800 μm^2 had a minimal effect on the conductivity. Modifying the area on the linear spot parallel to the electric field resulted in the conductivity remaining relatively unchanged, increasing 2% from 1.24 mho/m to 1.26 mho/m for a spot with an energy of 15 mJ. Changing the area in the linear beam transverse to the electric field by widening the beam across the gap resulted in an decrease in the conductivity from 1.13 mho/m to 0.97 mho/m, a 16% decrease.

Changing the laser power had a slight effect on the conductivity with many of the spot shapes or laser orientations examined in the study. The conductivity increased 23%, from 2.23 mho/m to 1.82 mho/m, in the long laser pulse parallel to the electric field. On the more focused parallel pulse, conductivity increased by 9%, from 2.31 mho/m to 2.52 mho/m. The laser pulse energy had little effect on the conductivities in the laser spots oriented transverse to the electric field. Conductivity increased by 8%, from 1.82 mho/m to 1.96 mho/m in the wider spot. Increasing the power in the more focused spot held the conductivity steady around 2.21 mho/m.

3.7 Statistical Analysis of Laser Triggering Parameter Results

Regression Statistics	
Multiple R	0.9763
R Square	0.9531
Adjusted R Square	0.9509
Standard Error	0.9018
Observations	160

ANOVA

	df	SS	MS	F	Significance F
Regression	7	2511.7896	358.8271	441.2344	1.4650E-97
Residual	152	123.6116	0.8132		
Total	159	2635.4013			

	Coefficients	Standard Error	t Stat	P-value	Lower 95%	Upper 95%
Intercept	46.5077	0.3573	130.1538	0.0000	45.8017	47.2137
Spot Area	0.0017	0.0001	16.0333	0.0000	0.0015	0.0019
Orientation	2.5859	0.2112	12.2427	0.0000	2.1686	3.0032
Laser Power	-0.0325	0.0078	-4.1895	0.0000	-0.0479	-0.0172
Random Seed	0.0116	0.0248	0.4680	0.6404	-0.0374	0.0607
Area-Orientation Interaction	-0.0016	0.0001	-30.7069	0.0000	-0.0017	-0.0015
Orientation-Power Interaction	0.0016	0.0032	0.5128	0.6088	-0.0046	0.0079
Area-Power Interaction	0.0000	0.0000	1.0981	0.2739	0.0000	0.0000

Table 5 - Regression analysis for radius in relation to laser triggering parameters.

Table 5 shows the regression analysis done for radius in relation the laser
triggering parameters that were varied in the previously discussed simulations. P-values
of 0.05 or below are considered significant. The P-values in the analysis indicate that
each of the variables was independently significant, as well as the interaction between
spot area and spot orientation.

Regression Statistics	
Multiple R	0.9572
R Square	0.9163
Adjusted R Square	0.9124
Standard Error	0.0622
Observations	160

ANOVA

	df	SS	MS	F	Significance F
Regression	7	6.4464	0.9209	237.7097	1.7355E-78
Residual	152	0.5889	0.0039		
Total	159	7.0352			

	Coefficients	Standard Error	t Stat	P-value	Lower 95%	Upper 95%
Intercept	2.3296	0.0247	94.4561	0.0000	2.2808	2.3783
Spot Area	-0.0001	0.0000	-10.6309	0.0000	-0.0001	-0.0001
Orientation	-0.0898	0.0146	-6.1604	0.0000	-0.1186	-0.0610
Laser Power	-0.0017	0.0005	-3.2416	0.0015	-0.0028	-0.0007
Random Seed	-0.0008	0.0017	-0.4805	0.6315	-0.0042	0.0026
Area-Orientation Interaction	0.0001	0.0000	16.8739	0.0000	0.0001	0.0001
Orientation-Power Interaction	0.0017	0.0002	7.5516	0.0000	0.0012	0.0021
Area-Power Interaction	0.0000	0.0000	9.5518	0.0000	0.0000	0.0000

Table 6 - Regression analysis for conductivity in relation to laser triggering parameters.

Table 6 shows the regression analysis done for conductivity in relation to the laser triggering variables. The generated P-values indicate that each and every variable; spot area, spot orientation, and laser power; and their interaction with one another was significant to the conductivity.

Chapter 4

Fluid Model Results

4.1 Overview of Results for Fluid Model

The fluid model was used to determine that the spark gap characteristic that was most significantly affected by varying values of initial arc radius, arc conductivity, and gas density in the spark gap was the arc resistance. A higher initial radius, higher conductivity, and lower gas density all resulted in a decrease in the fall time of the resistance of the arc, i.e. a faster switch. However, none had a significant effect on either the inductance or the impedance of the spark gap switch. Change in inductance values were insignificant when compared to the 100 nH inductance that accounts for the transition from the larger area of the plate that makes up part of the Blumlein to the small area of the electrode in the spark gap. This inductance also dominates the impedance of the switch making any effect due to changes to experimental parameters almost negligible.

Arc Resistance	Initial Radius	Conductivity	Gas Density
Initial Radius	Yes		
Conductivity	No	Yes	
Gas Density	No	No	Yes

Switch Inductance	Initial Radius	Conductivity	Gas Density
Initial Radius	No		
Conductivity	No	No	
Gas Density	No	No	No

Switch Impedance	Initial Radius	Conductivity	Gas Density
Initial Radius	No		
Conductivity	No	No	
Gas Density	No	No	No

Table 7 - Overview of effects of various parameters on the arc resistance, inductance, and impedance in the fluid model. A 'Yes' indicated that there was a large effect of the vertical and horizontal parameters; identical intersection fields denote that it had a large single parameter effect. A 'Yes' in other intersection fields denote that a large effect was observed when the parameters were varied in conjunction.

4.2 Process for Developing the Fluid Model

The fluid model utilized the Braginskii model relating arc current to arc radius as well a circuit model representing the Blumlein system to describe the behavior of the conducting arc in a spark gap. The fluid model made use of conditions for the conducting arc that included the physical parameters of the spark gap, properties of the Blumlein, and the initial voltage of the system. The Braginskii model was modified by

introducing an initial radius parameter. The streamer radius result from the kinetic model

described in the previous chapter provided the initial arc radius for the fluid model. This

parameter provides the fluid model a required initial resistance. The model without this

initial resistance would experience no current flow, and therefore no arc channel

expansion. The model was solved in *Mathematica*. A depiction of the behavior

throughout the life of the conducting arc was ascertained utilizing the Blumlein circuit

model and the Braginskii arc model.

A discrete element model of the Blumlein circuit was developed. Each

transmission line in the Blumlein was modeled as a series of four inductors and

capacitors. A first-order differential equation represented each voltage at a node and

current through a loop in the circuit model. This circuit model is depicted in Figure 14.

A resistance matching the sum of the impedances in the transmission lines represented

the load. A variable resistance and inductance represented the switch corresponding to

the Braginskii model, and a constant inductor represented the transition of the conductor

from the plates in the Blumlein to the electrode in the switch.
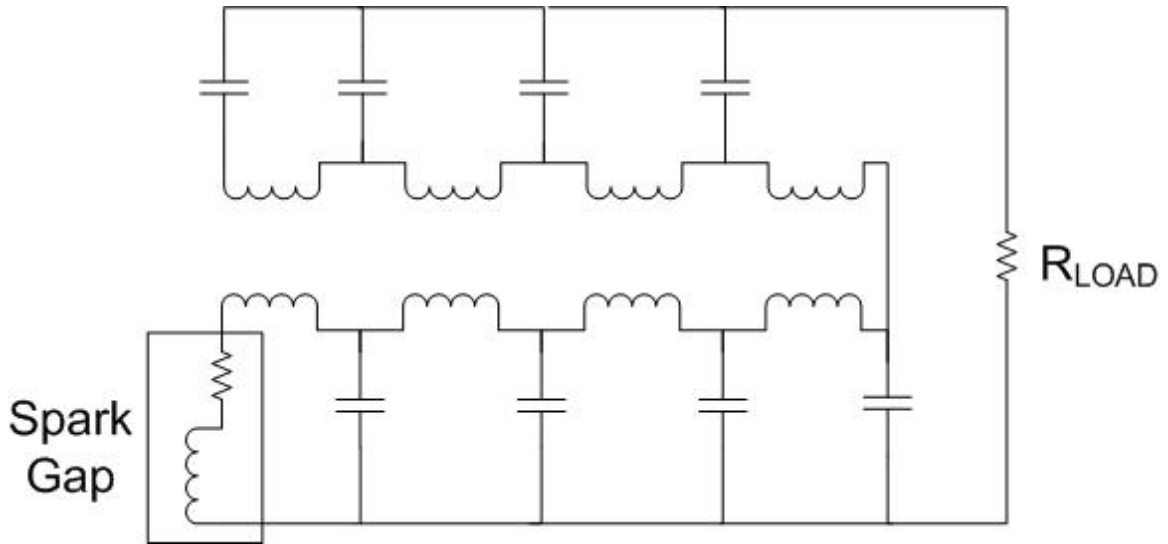
Figure 14 - The circuit model representing the Blumlein and spark gap. C represents one-quarter of the total capacitance in a single transmission line and L represents one-quarter of the inductance. The load resistance is the sum of the impedance in the transmission lines. A time dependant resistance and inductance represent the spark gap switch.

The differential equations shown in Appendix V were solved to determine the voltages and currents throughout the circuit model. The value for the gas density of the shown solution was 3.87 kg/m^3. The values for the initial radius and arc conductivity of the shown solution were 35 μm and 20,000 mho/m, respectively. A plot of the solution for the arc current through the switch is shown in Figure 15, and the switch voltage is shown in Figure 16.
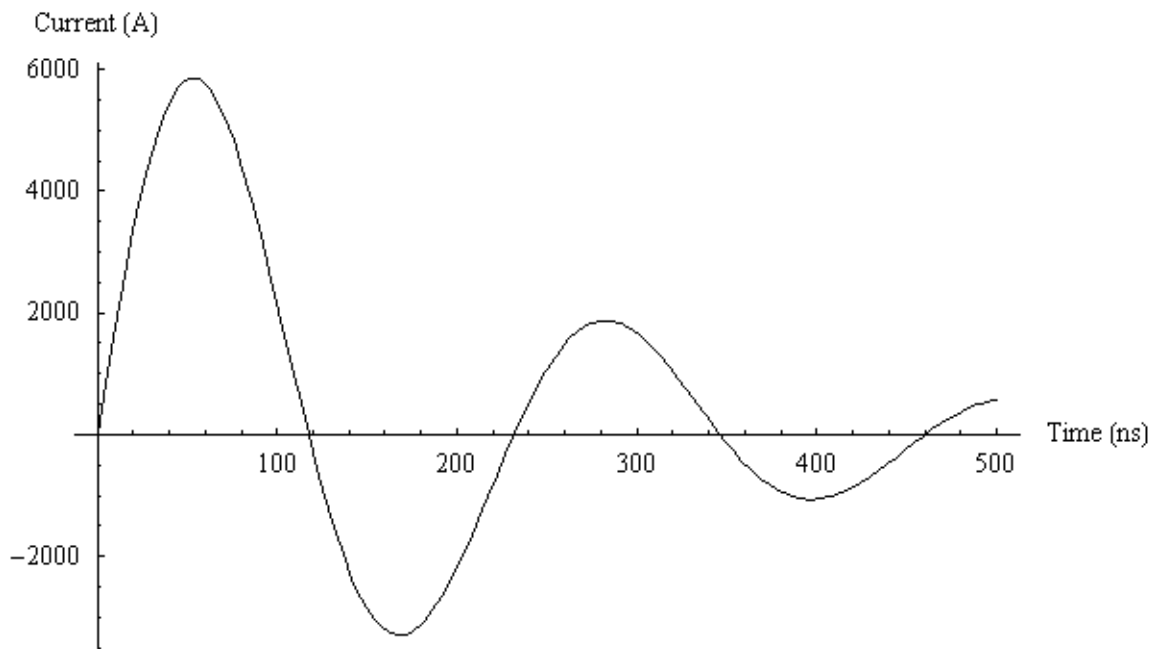
Figure 15 - Arc current determined from solving the set of differential equations describing the Blumlein pulse forming system. Gas density was 3.87 kg/m³. Conductivity was 20,000 mho/m. Initial radius was 35 μm.
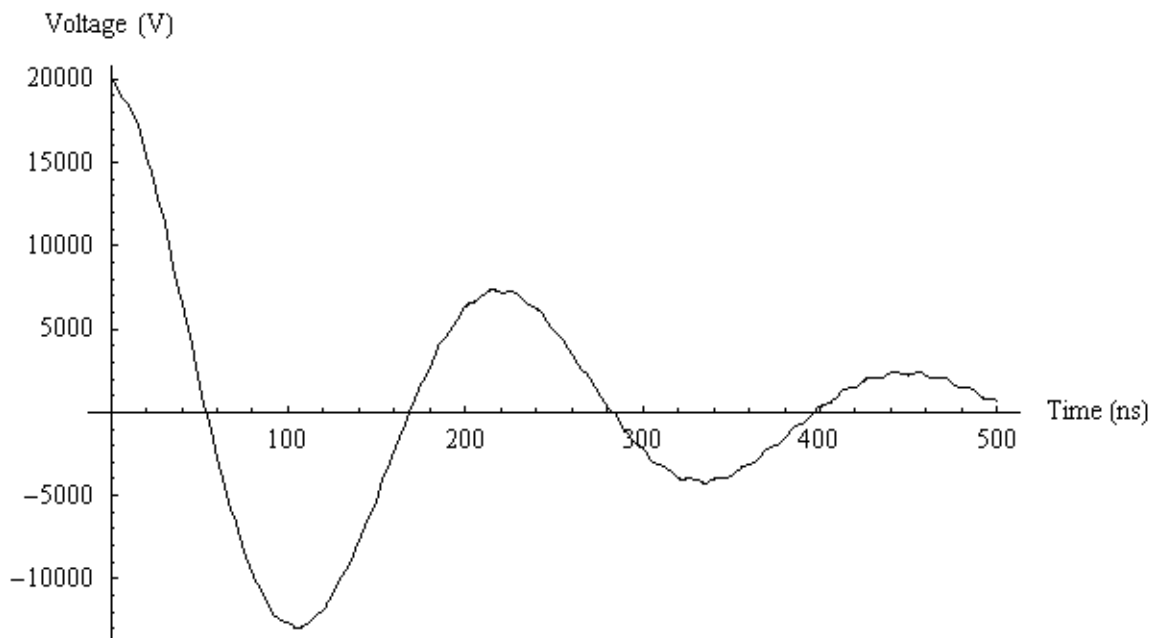
Figure 16 - Switch voltage determined from solving the set of differential equations describing the Blumlein pulse forming system. Gas density was 3.87 kg/m³. Conductivity was 20,000 mho/m. Initial radius was 35 μm.

55

The current over time through the switch was substituted into Equation (1), which is the Braginskii arc model to determine the arc radius over time, where a_0 initial radius, a is the radius, ρ_0 is the gas density, σ is conductivity, ξ is an experimentally derived constant equal to 4.5, and I is the current. The arc radius is shown in Figure 17.

$$a^2(t) = a_0^{\,2} + \left(\frac{4}{\pi\rho_0\xi\sigma}\right)^{\frac{1}{3}} \int I^{\frac{2}{3}} dt \qquad (1)$$
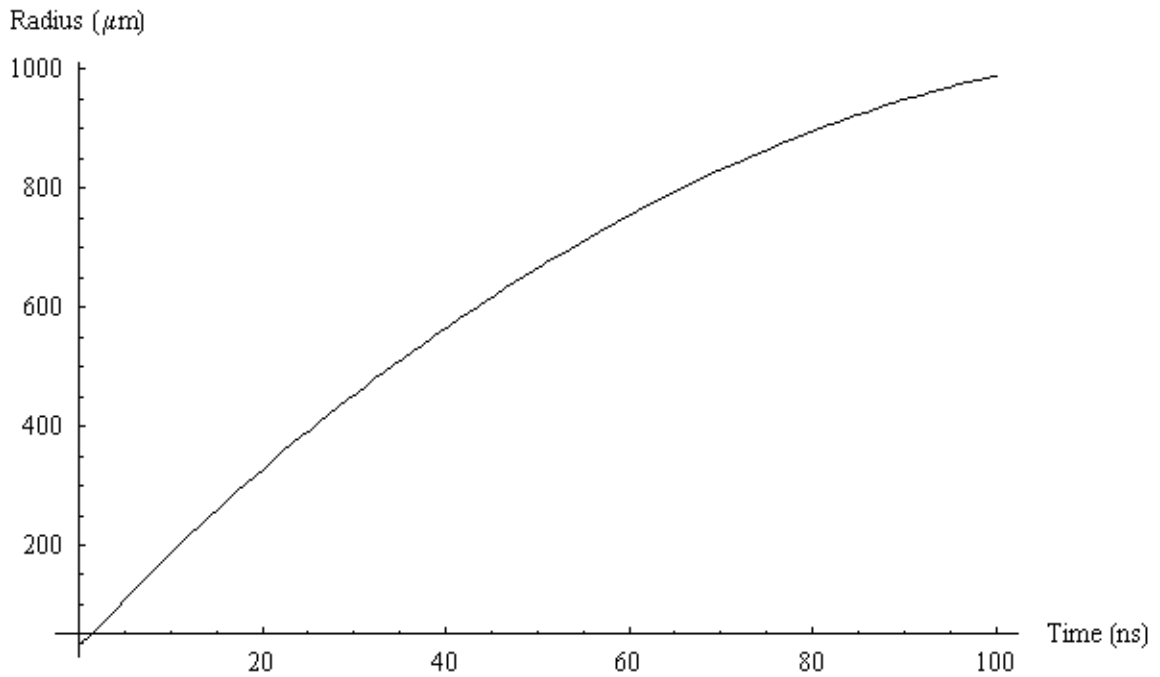
Figure 17 - Arc radius in the spark gap determined from substituting arc current into Equation (1). Gas density was 3.87 kg/m³. Conductivity was 20,000 mho/m. Initial radius was 35 μm.

The arc radius over time yields the resistance found from Equation (2) and shown in Figure 18, where R is resistance, d is the separation between the electrodes, and σ is conductivity.

$$R(t) = \frac{d}{\sigma \pi a^2(t)} \qquad (2)$$
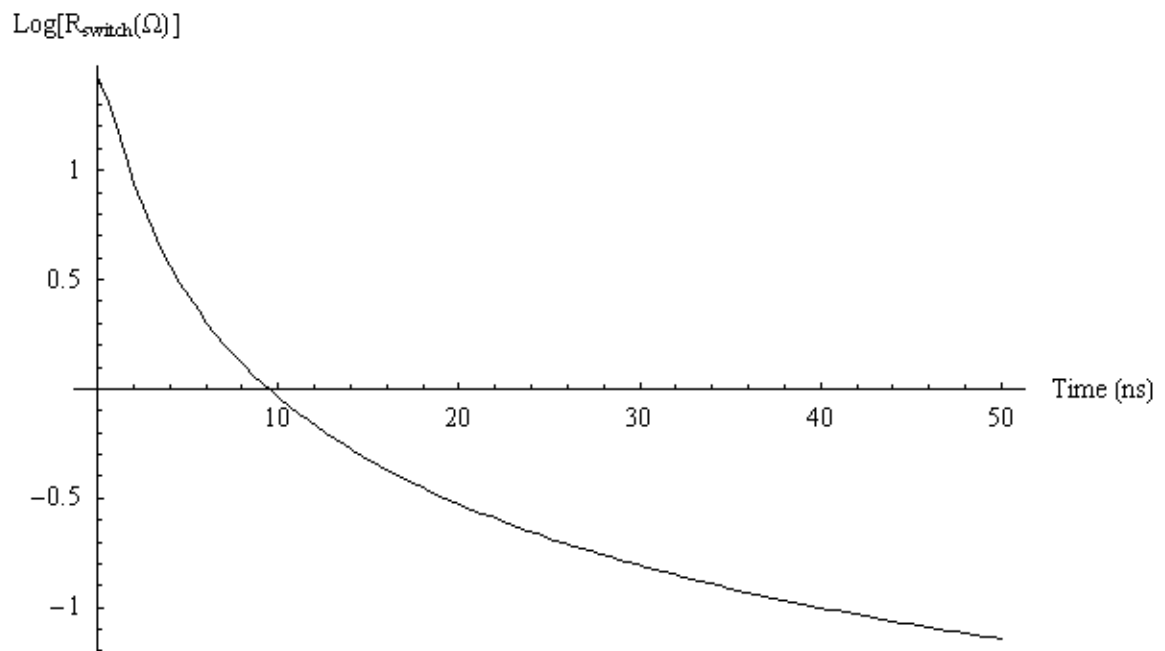
Figure 18 - Log$_{10}$ of the resistance of the arc determined from substituting the arc radius into equation (2). Gas density was 3.87 kg/m^3. Conductivity was 20,000 mho/m. Initial radius was 35 μm.

The inductance in the arc over time is also found using Equation (3) and shown in Figure 19, where L is inductance and a_{cr} is the current return radius. The inductance plot includes a 100nH inductance that is caused by the change in area from the large plate that is part of the Blumlein to the smaller electrode that is a part of the spark gap switch [1].

$$L(t) = 2 \times 10^{-7} d \ln\left(\frac{a_{cr}}{a(t)}\right) \qquad (3)$$
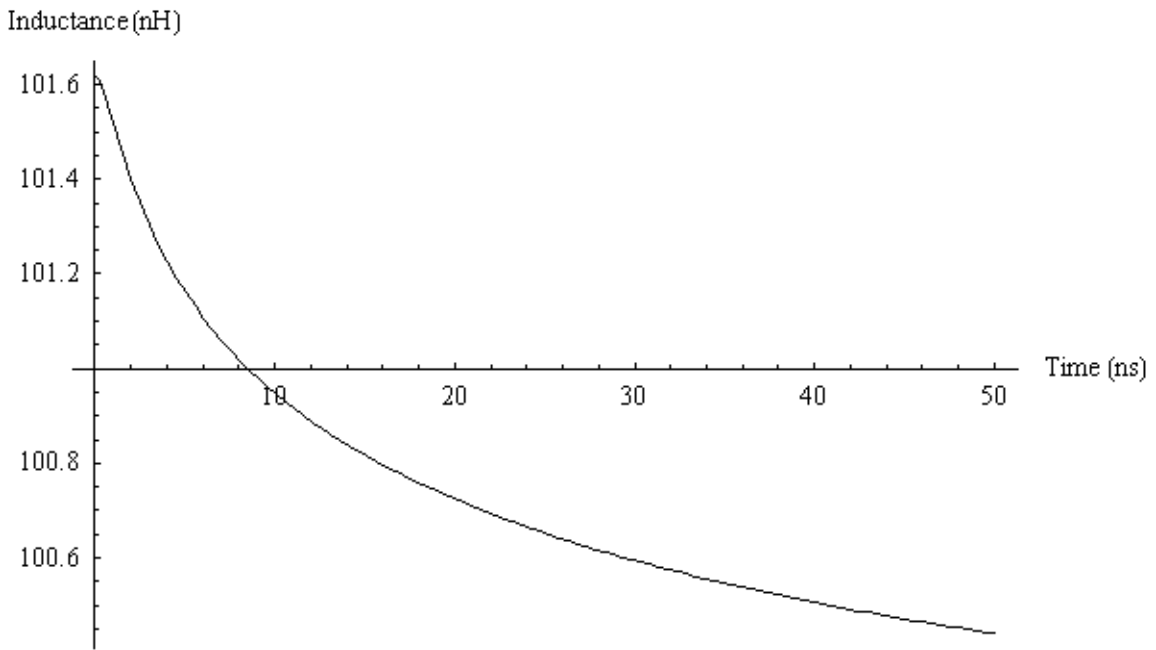
Figure 19 – Log$_{10}$ of the inductance through the spark gap determined by sustituting arc radius into equation (3). The value for inductance includes 100 nH that results from compressing the conductor from a large plate to a small electrode as part of the switch. Gas density was 3.87 kg/m^3. Conductivity was 20,000 mho/m. Initial radius was 35 μm.

Impedance in the arc was found by calculating the value for switch voltage divided by arc current in Equation (4) and shown in Figure 20.

$$Z(t) = \frac{V(t)}{I(t)}$$

(4)
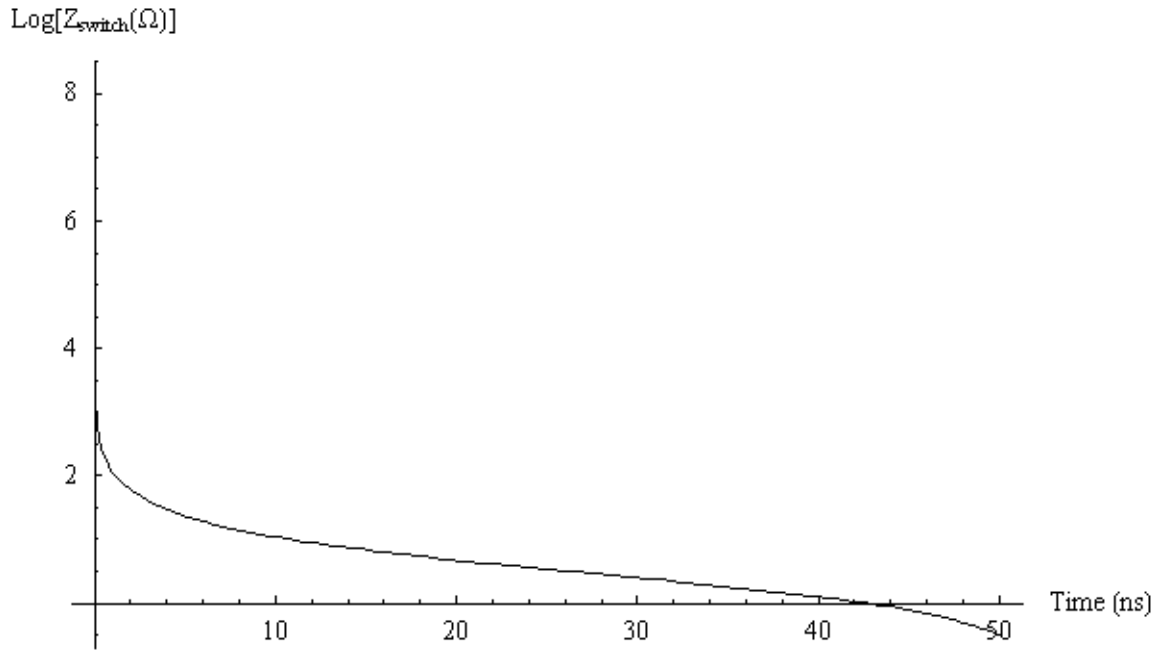
Figure 20 - Impedance through the switch determined by substituting solutions for switch voltage and arc current into equation (4).

The goal in developing the fluid model was to examine the effects seen on these three values when changes were made to the experimental parameters. A range of initial radii that might be obtained from the kinetic model were tested, 10 μm, 35 μm, and 60 μm. A range of conductivities were also tested. At a temperature of 5 eV, 10,000 mho/m, 20,000 mho/m, and 30,000 mho/m correspond to a plasma density of $2.5 \cdot 10^{23}$ m^{-3}, $5 \cdot 10^{23}$ m^{-3}, and $7.5 \cdot 10^{23}$ m^{-3}, respectively.

4.3 Energy Dissipation in the Spark Gap Switch

Analysis of the energy dissipation served two functions. First was to verify the validity of the simulation by comparing the amount of stored energy in the Blumlein system and the amount that was dissipated by the switch and by the load. Of greater interest was determining the percentage of the stored energy that was lost to the switch. This is the energy that was utilized to heat and expand the arc. Energy stored in the Blumlein was determined by Equation (5), where E is energy, C is the Blumlein capacitance, and V is the charge voltage.

$$E = \frac{1}{2}CV^2$$

(5)

The energy stored in the system was 2.788 J. This was calculated from a capacitance of 6.97 nF from each transmission line and charge voltage of 20 kV. Energy is lost from the system at two points: the spark gap switch and the load. The vast majority of the energy should be deposited in the load. Energy lost through the switch was determined by solving Equation (6), where I is current, R is the time dependant resistance of the arc, and t is the period of time when all the energy of the Blumlein has been expelled from the system.

$$E = \int_0^t I^2 R(\tau)d\tau$$

(6)

Energy loss to the switch was determined for several different experimental values of initial radius and conductivity as seen in Tables 8 and 9.

| | | Conductivity | | |
		10,000 mho/m	20,000 mho/m	30,000 mho/m
	10 μm	0.219 J	0.143 J	0.111 J
Initial Radius	35 μm	0.216 J	0.141 J	0.108 J
	60 μm	0.211 J	0.136 J	0.105 J

Table 8 - Energy dissipated in the switch for 3 values each of conductivity and initial radius. The energy dissipated is used to heat up and expand the conducting arc.

| | | Conductivity | | |
		10,000 mho/m	20,000 mho/m	30,000 mho/m
	10 μm	7.86%	5.13%	3.98%
Initial Radius	35 μm	7.75%	5.06%	3.87%
	60 μm	7.57%	4.88%	3.77%

Table 9 - Energy dissipated in the switch as a percentage of the total energy stored in the Blumlein system.

The tables show that more energy is dissipated by the arc when the conductivity is lower and, to a lesser degree, when the initial arc radius is smaller.

4.4 Resistance, Inductance and Impedance Falltime Results of Fluid Model

Three parameters were varied to determine their effect on the impedance, resistance, and inductance of the conducting arc: the initial arc radius, conductivity of the arc, and the density of the gas in the spark gap. The effects of changing the steady state conductivity of the arc were explored and the results are depicted in the first set of graphs.

The effects of changing the initial radius were explored and the results are reiterated in the second set of graphs. For both of these sets of data, the gas density was kept constant at 3.87 kg/m^3. This is the gas density for a spark gap filled with dry air at 3 atm. The gas density was varied in the final set of experiments (last set of graphs). Changing the gas type and changing the pressure are both ways in which the gas density could be changed in an experimental setting. Four values for gas density were explored: 0.900 kg/m^3 (Neon at 1 atm), 2.70 kg/m^3 (Neon at 3 atm), 1.65 kg/m^3 (Argon at 1 atm), and 4.95 kg/m^3 (Argon at 3 atm). Conductivity was kept constant at 20,000 mho/m and initial radius remained at 35 μm. Graphs were generated to show the differences in the impedance, resistance, and inductance over time when the experimental values were changed.

4.4.1 Arc Resistance Over Time At Varying Conductivities

Resistance of the arc was directly affected by the conductivity of the plasma generating the arc. Figure 21 shows a 54% reduction of the initial resistance between the arc with a conductivity of 10,000 mho/m and the arc with a conductivity of 20,000 mho/m. It also shows a 42% reduction of the initial resistance between the arc with a conductivity of 20,000 mho/m and the arc with a 30,000 mho/m conductivity. The initial arc radius for the data represented in the graph was 10 μm. The difference in resistance gradually lessens to < 1% 10 ns into the arc formation when the arc resistances have fallen to approximately 1 ohm. Changing the initial radii to 35 μm and 60 μm resulted in a similar behavior in the resistance of the arc.
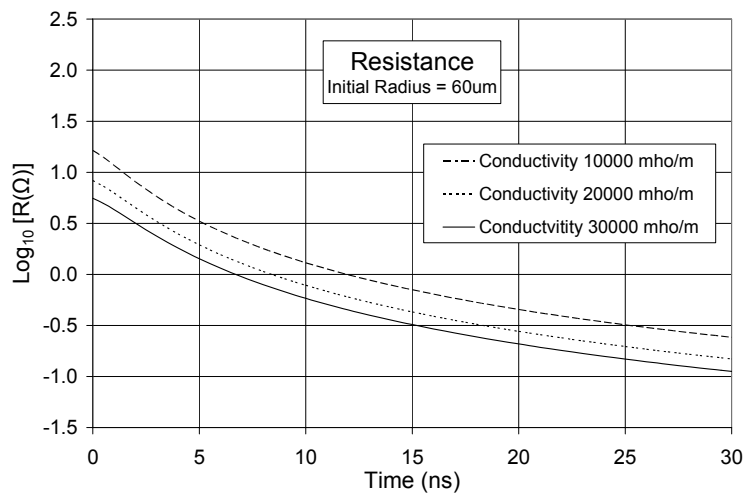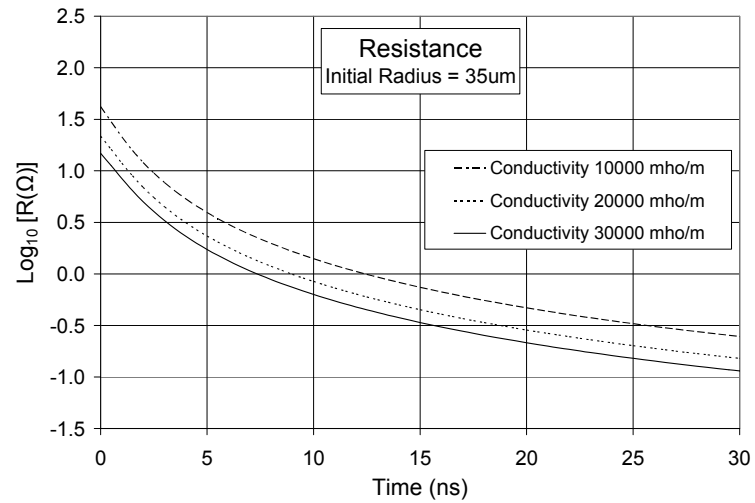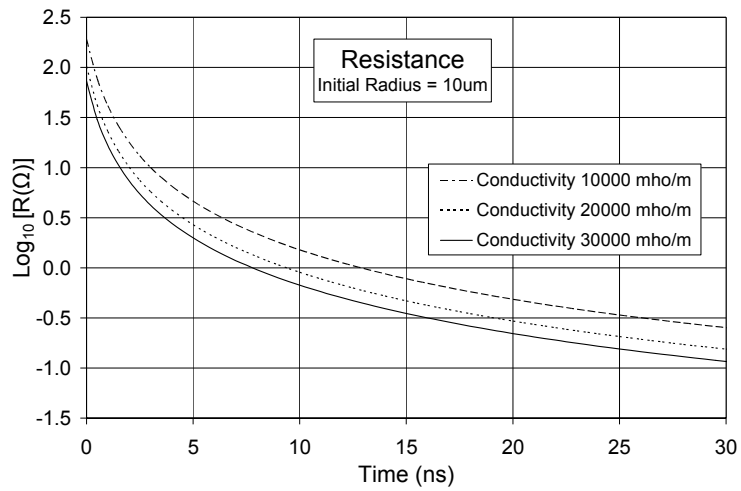
Figure 21 - Resistance of the arc over time with arc conductivities of 10,000 mho/m, 20,000 mho/m, and 30,000 mho/m. Initial arc radius is 15 μm in the upper graph, 35 μm in the middle graph, and 60 μm in the lower graph. Gas density was 3.87 kg/m³.

4.4.2 Switch Inductance Over Time At Varying Conductivities

Inductance of the arc is slightly affected by the change in conductivity. Lower

conductivities accounted for a lower inductance in each case. However, the overall

reduction in inductance from arc formation to a steady state conducting arc was small

compared to the 100 nH inductance that represents the change in geometry of the

Blumlein. Figure 22 illustrates the behavior of the switch inductance, including the 100

nH built-in inductance, for an initial arc radius of 10 μm, 35 μm, and 60 μm.
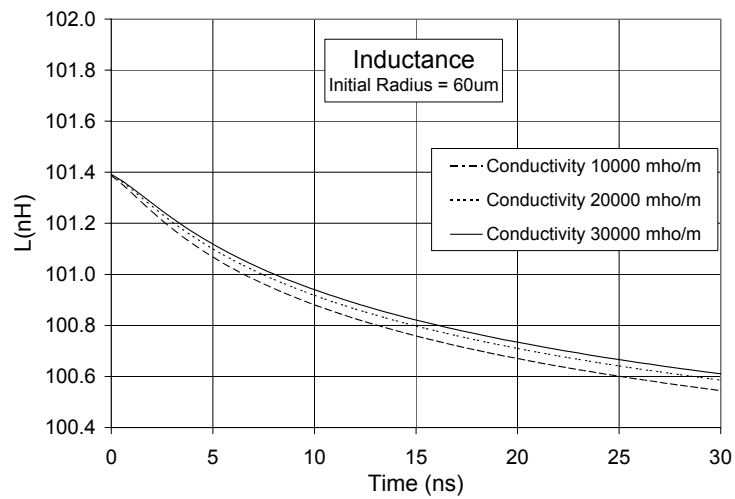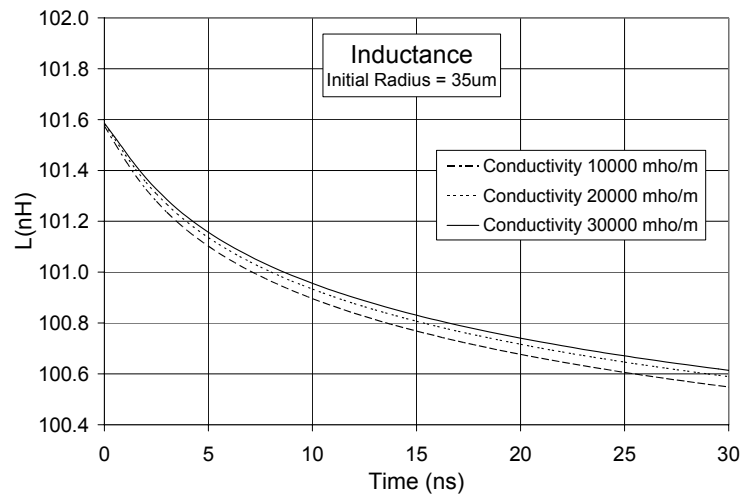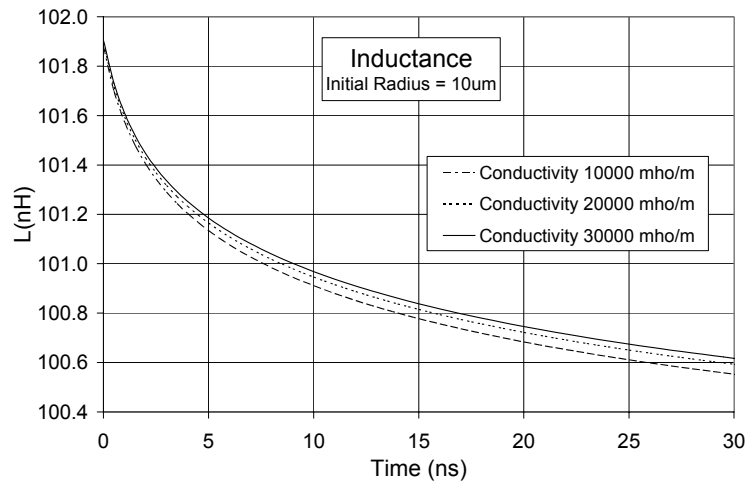
Figure 22 - Inductance through the switch over time with arc conductivities of 10,000 mho/m, 20,000 mho/m, and 30,000 mho/m. Initial radius of the arc is 10 μm in the upper graph, 35 μm in the middle graph and 60 μm in the lower graph.

4.4.3 Switch Impedance Over Time At Varying Conductivities

Impedance does not appear to be affected significantly by changing the conductivity. The effect is illustrated in Figure 23. Graphs were generated for initial arc radii of 10 μm, 35 μm, and 60 μm. Increasing conductivity does slightly decrease the impedance fall time in each case.
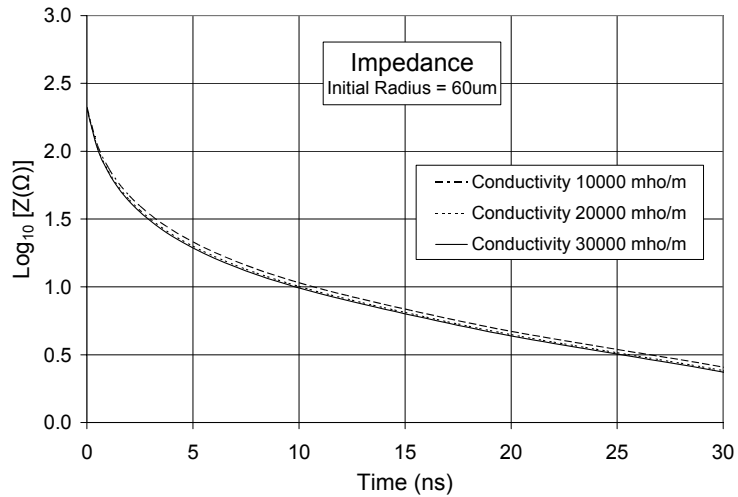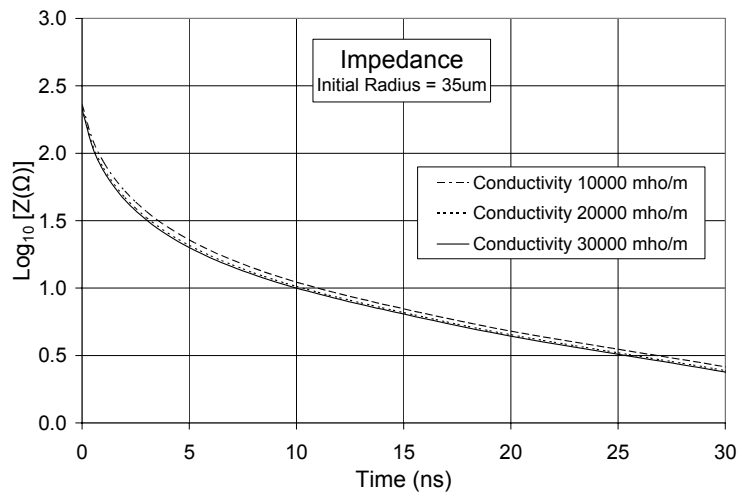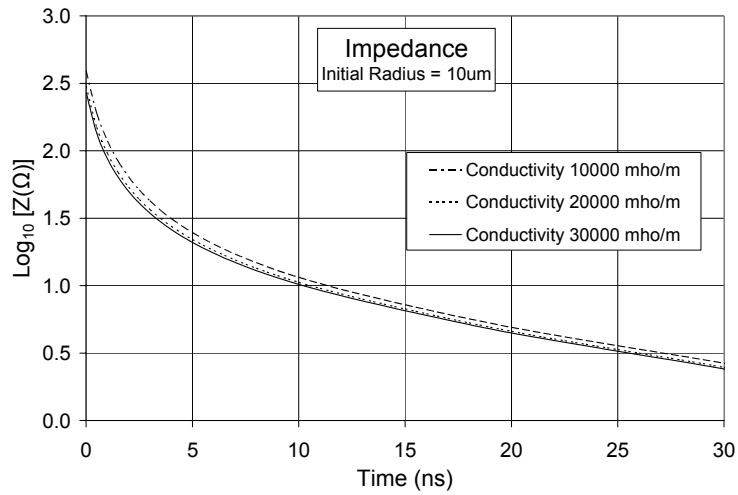
Figure 23 - Impedance through the switch over time with arc conductivities of 10,000 mho/m, 20,000 mho/m, and 30,000 mho/m. Initial radius of the arc is 61 μm in the upper graph, 35 μm in the middle graph and 60 μm in the lower graph.

68

4.4.4 Arc Resistance Over Time At Varying Initial Arc Radii

The resistance behavior of the arc was greatly affected by the initial radius of the arc for the first 10 ns of the arc's life. Figure 24 shows the behavior of the arc at the varying initial radii of 10 μm, 35 μm, and 60 μm for conductivities of 10,000 mho/m, 20,000 mho/m, and 30,000 mho/m. The initial resistance for the smaller initial radii was higher than for the larger initial radii. However, the difference became less significant as the arc formed, and was seen to be less than 1% after 10 ns.
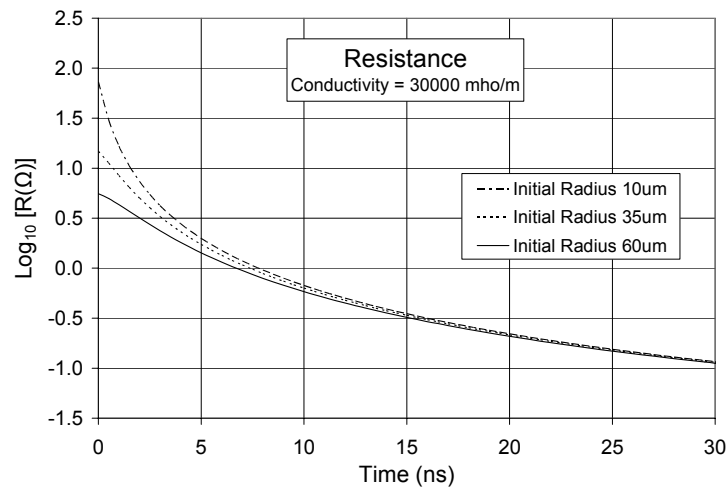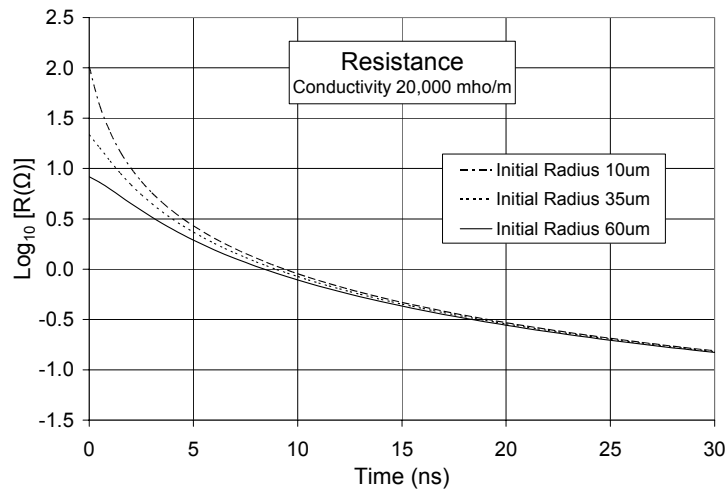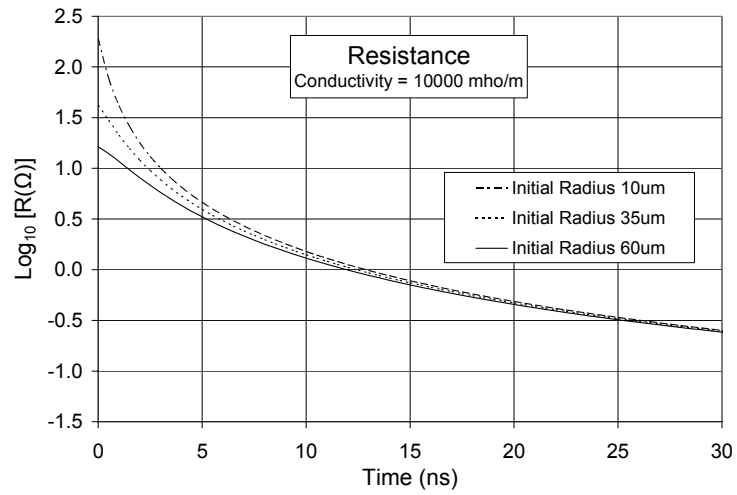
Figure 24 - Resistance of the arc over time with an initial arc radii of 10 μm, 35 μm, and 60 μm. Conductivity of the arc is 10,000 mho/m, in the upper graph, 20,000 mho/m in the middle graph, and 30,000 mho/m in the lower graph.

70

4.4.5 Switch Inductance Over Time At Varying Initial Arc Radii

The difference in inductance caused by increasing the initial radius of the arc was again insignificant when compared to the 100 nH built-in inductance of the Blumlein system. The difference in inductance between an arc with an initial radius of 10 μm, and an arc with an initial radius of 60 μm, was only about 0.45 nH at the initial formation of the arc. This difference decreased throughout the life of the arc. The effect can be seen in Figure 25.
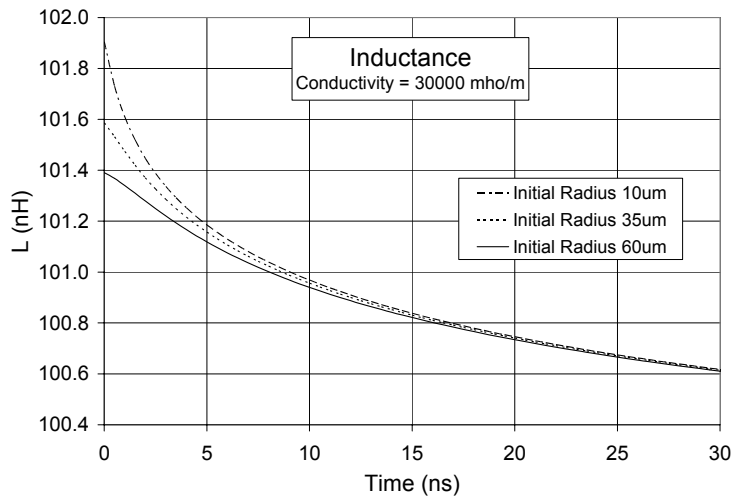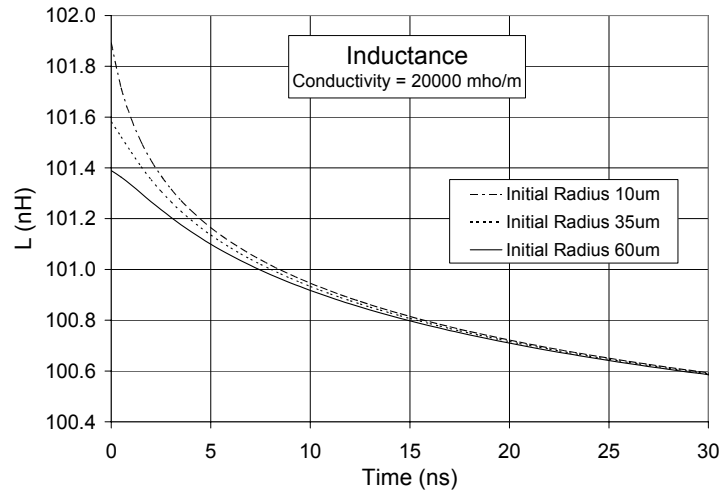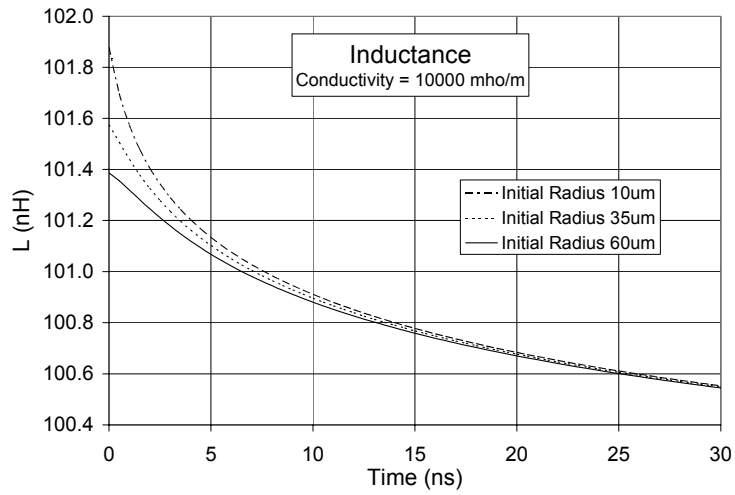
Figure 25 - Inductance through the switch over time with initial arc radii of 10 µm, 35 µm, and 60 µm. Conductivity of the arc is 10,000 mho/m in the upper graph, 20,000 mho/m in the middle graph, 30,000 mho/m in the lower graph.

4.4.6 Switch Impedance Over Time At Varying Initial Arc Radii

Figure 26 illustrates the effects on switch impedance of adjusting the initial radius of the arc at various arc conductivities. These graphs shows the slight effect changing the initial radius had on the impedance of the switch at a steady state conductivity of 10,000 mho/m, 20,000 mho/m, and 30,000 mho/m. A slight increase in the fall time of the impedance was seen for a higher initial arc radius for all three cases. This effect became indistinguishable after 10 ns.
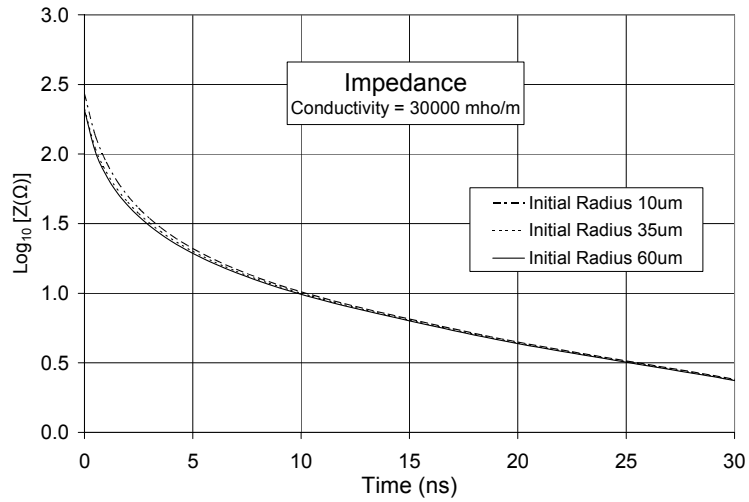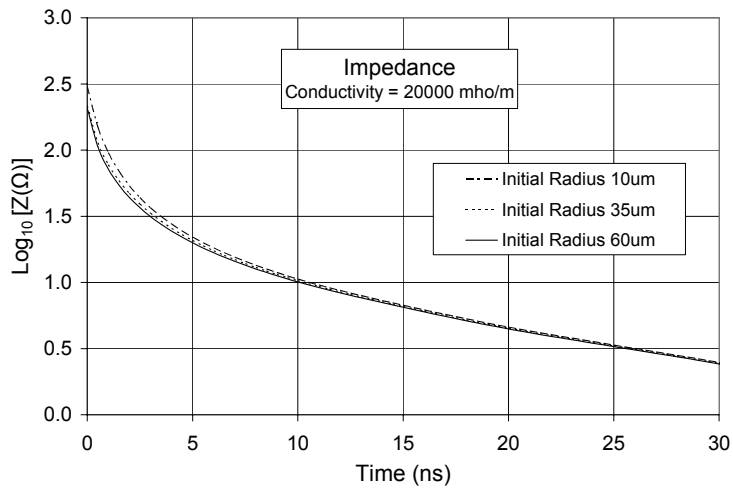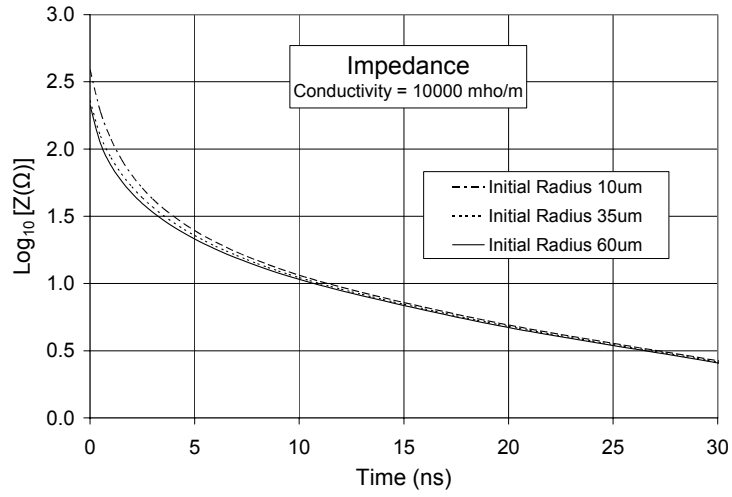
Figure 26 - Impedance through the switch over time with initial arc radii of 10 µm, 35 µm, and 60 µm. Conductivity of the arc is 10,000 mho/m in the upper graph, 20,000 mho/m in the middle graph, and 30,000 mho/m in the lower graph.

4.4.7 Resistance, Inductance And Impedance Over Time At Varying Gas Densities

Figure 27 represents the results obtained when the density of the gas pressurizing the spark gap was varied. A change in density in an experimental setting can be accomplished by either increasing the pressure or changing the type of gas used in the spark gap. All three graphs were generated with an initial arc radius of 35 μm and an arc conductivity of 20,000 mho/m. The graph of the gap impedance shows virtually no difference when changing the gas density between values that are given by Argon and Neon at pressures of 1 and 3 atm. The resistances of the arcs at the varying gas pressures had identical initial values. The lighter gas did, however, allow the arc resistance to drop at a faster rate. Neon at 1 atm, with a density of 0.900 kg/m^3, allowed the resistance to reach a value of 1 ohm 3 ns faster than Argon at 3 atm with a density of 4.95 kg/m^3. The value of the inductance also fell more rapidly and to a lower final value with a lighter gas pressurizing the spark gap. However, the change in value was still insignificant compared to the 100 nH inductance caused by transitioning from the large flat plate of the Blumlein to the small electrode of the spark gap.
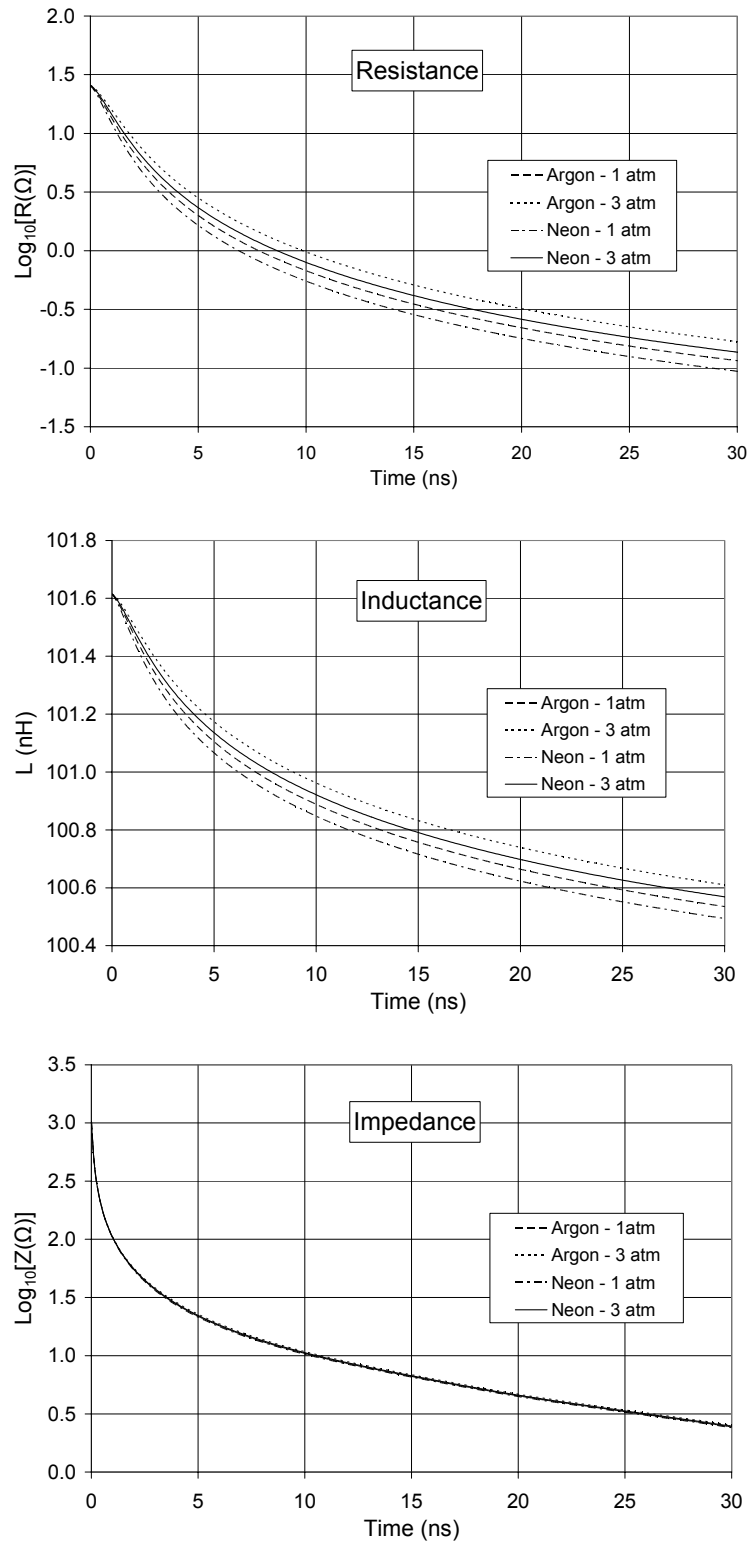
Figure 27 - Impedance (upper), Resistance (middle), and Inductance (lower) through the switch at varying gas densities corresponding to specific gas types and pressures. The initial arc radius is 35 μm and the arc conductivity is 20,000 mho/m.

76

Chapter 4 References

[1]   Personal communication from Dr. William C. Nunnally at Lawrence Livermore
        National Laboratory, November, 2004

Chapter 5

Summary and Conclusions

5.1 Summary

Two models have been developed to examine a laser triggered, gas filled spark gap used to switch a Blumlein pulsed power system. A kinetic model was developed with the particle-in-cell code XOOPIC to simulate the formation of the plasma streamer. This streamer forms the initial connection between the high voltage electrode and the grounded electrode. Information on the streamer radius and conductivity were determined from code output on particle position and velocity. The radius and conductivity represented the initial conditions for the fluid model, which was used to examine the electrical behavior of the arc. The fluid model, based on the model developed by Braginskii, was used to provide information on the resistance, inductance, and impedance over time in the spark gap. The overall goal was to determine experimental parameters that could be varied to decrease the resistive fall time of the arc and therefore lead to a faster current rise time in the Blumlein load.

The kinetic model study was performed in two separate sets of simulations. The intrinsic switch parameters of electric field, pressure, and gas type were varied to discover the effect on the streamer radius. The electric field was varied between 2 and 5 MV/m. Pressure was varied between 1 and 1.5 atm. Two gas types, Neon and Argon, were investigated. Changes to the electric field and gas type resulted in the largest effect on the radius and conductivity. A higher electric field caused a larger electron density, leading to a higher conductivity and a larger radius. Switching from Neon to Argon fill gas lowered the conductivity due to the higher electron temperature for the Neon-filled simulation. This change had no effect on the radius. Varying the pressure did not lead to any changes in streamer radius or conductivity.

The laser triggering effects were also varied, including the laser spot shape, spot area, and laser power. The laser spot was reoriented from a linear beam parallel to the electric field to a linear beam transverse to the electric field. The spot area was varied from 1200 μm^2 to 4800 μm^2 while maintaining constant pulse energy. The parallel beam was 12 μm wide and varied in length between 0.1mm and 0.4 mm. The transverse beam was 24 μm high and varied in width between 0.05 mm and 0.2 mm. The laser power was varied between 15 mJ and 60 mJ. The laser triggering parameters shown to have the greatest effect on the streamer radius were orientation of the beam and cross-sectional area. A wide, transverse beam had a larger radius than a narrow parallel beam. However, the opposite effect was noted for conductivity. All other laser triggering conditions were shown to have little effect on the radius and conductivity.

The initial arc radius, steady state conductivity, and gas density were varied in the fluid model. The radius was varied from 15 μm to 60 μm. These values encompassed

the values for the streamer radius generated by the kinetic model. Conductivity was

varied from 10,000 mho/m to 30,000 mho/m. While the streamer conductivity found in

the kinetic model was not utilized in the fluid model, it is assumed that a higher initial

conductivity will lead to a faster resistive fall time. Gas density in the fluid model was

varied from 0.0900 kg/m^3, which is the density of Neon at 1 atm, to 4.95 kg/m^3, which is

the density of Argon at 3 atm. All three parameters were shown to have an effect on the

fall time of the resistance. Higher initial arc radii, greater steady state conductivities, and

lighter gas densities led to faster fall times. However, no parameter had a large effect on

the inductance compared to the 100 nH built-in inductance. This inductance was caused

by the flow of current from a plate with a wide area in the Blumlein to an electrode with a

small area in the spark gap. There was also little effect on the impedance of the spark

gap.

5.2 Conclusions

The plots in Figures 23 and 26 in Chapter 4 show the difficulty in affecting the

impedance fall time of the spark gap by changing the parameters chosen in this study.

The impedance of the spark gap is still higher than the impedance of the transmission line

after 30 ns. This value must fall to a value significantly less than the impedance of the

transmission line to generate a good current pulse in the load. The high impedance is due

to the 100 nH inductance that is as result of the convergence of current from the

transmission line plates on the Blumlein to the spark gap. It can be seen that this

inductance has a large effect by utilizing equations for current rise time in the load from Chapter 1,

$$T_{RISE} \approx \sqrt{T_{RESISTIVE}^2 + T_{INDUCTIVE}^2} \qquad (1)$$

$T_{RESISTIVE}$ is the time taken for the resistance to fall to a value significantly less than the impedance of the transmission line and $T_{INDUCTIVE}$ is approximated by

$$T_{INDUCTIVE} \approx \frac{3 \cdot L_{sw}}{Z_L} \qquad (2)$$

where L_{sw} is the inductance of the switch and Z_L is the load impedance. $T_{RESISTIVE}$ was taken to be around 10 ns. $T_{INDUCTIVE}$ is calculated to be 75 ns with the switch interface inductance of 100 nH and the load impedance of 4 Ω. The value for $T_{RESISTIVE}$ fluctuates as the experimental parameters explored in this work are varied, but the changes are insignificant in affecting the calculated value of T_{RISE}. This calculated value is about 76 ns. Given this information, it can be concluded that the 100 nH built-in inductance prevents any progress made in decreasing the resistive fall time of the arc from having a meaningful effect on the rise time. Methods for decreasing this inductance were not investigated in this work.

The models were developed in order to determine methods of decreasing the resistive fall time in the spark gap. Changes in several parameters were shown to have an effect. Figure 21 in Chapter 4 shows that higher steady state conductivity in the arc will facilitate a faster fall time in the arc resistance. However, methods of obtaining this higher conductivity were not investigated.

A larger initial arc radius is shown in Figure 24 in Chapter 4 to decrease the resistive fall time of the arc. Methods of increasing the initial arc radius are explored in the kinetic model. One of the two most significant effects can be seen by increasing the electric field across the gap by increasing the charge voltage of the Blumlein or shaping the electrodes. The higher electric field leads to a larger diameter streamer, and therefore a larger initial arc radius. This is seen in Figure 9 of Chapter 3. Large increases of the initial radius were also realized by orienting the triggering laser pulse as a linear beam transverse to the electric field. Wider trigger beams led to larger initial radii. This effect is shown in Figure 11 of Chapter 3.

Figure 27 in Chapter 4 shows that a lighter gas density causes the resistance to drop more quickly. Lighter gas density can be achieved by decreasing the pressure or by decreasing the fill gas atomic weight (for example, Argon to Neon). Kinetic model results in Figure 9 in Chapter 3 show that a lower pressure does not have a large effect on the streamer radius or conductivity. However, a lighter gas is shown to decrease the conductivity of the streamer (Figure 10 of Chapter 3).

An increase in streamer conductivity is assumed to decrease the resistive fall time even though this is not considered in the fluid model. Various changes in parameters explored in Chapter 3 cause a change in streamer conductivity. An increased electric field will increase the conductivity as seen in Figure 10 of Chapter 3. Spreading the linear laser pulse across the gap (seen in Figure 12 of Chapter 3) decreases the conductivity. While it is assumed that higher streamer conductivity contributes to a decrease in the fall time of the arc resistance, it is likely that the variation seen with these

simulations would be insignificant given the proper model and analysis when considering that the steady state conductivity of the arc is around 20,000 mho/m.

5.3 Future Work

The two models themselves can be adapted to represent virtually any spark gap in any given application. Adjustments in the kinetic model can be made to the simulation space in order to better approximate a particular switch. The intrinsic parameters electric field, pressure, and gas type can be adjusted to more typical values of a given switch and varied around these values in order to see their effect on the switch. The fluid model can be easily redesigned to represent a charging system different than a Blumlein system by introducing the representative discrete element circuit.

Many improvements to the kinetic model can be made by simply increasing the amount of computing power available. Currently, both the voltage and the switch size must be scaled down to accommodate the Blumlein spark gap application. With more computing power, switch size can be expanded to encompass the entire switch and voltage can be increased to the appropriate value. A higher voltage leads to denser plasma and a larger switch size leads to more particles. Denser plasmas could require a more refined mesh size because of the decrease in the Debye length.

The kinetic model is currently only capable of simulating spark gaps filled with Argon, Neon, or other noble gasses. Development of a collision model to be utilized by XOOPIC would allow other gasses commonly used in spark gaps, such as dry air and SF_6, to be used in the model. The effects of changing gasses from dry air to SF_6 could be considered more useful to experimentalists who do not use Argon and Neon. The model

could also show that pressure changes could affect the streamer radius and conductivity given these new options for gas type.

The fluid model was Braginskii's arc model, coordinated with a discrete circuit model representing the Blumlein array. Because of Braginskii's assumption of a constant, high steady state conductivity, information about the arc between the initial connection and the time when the arc is fully developed was lost. A model that deals with the transition from the low conductivity in the streamer to the high steady state conductivity in the fully developed arc would better illustrate the arc formation and lead to better data on the resistive fall time of the arc. Such a development would also allow both the streamer radius and streamer conductivity to be utilized as initial conditions in the fluid model (rather than just the streamer radius measured here).

Appendix I – Construction and Maintenance of the Linux Computer Cluster

The Linux Cluster consists of 5 Pentium IV computers utilizing the Red Hat 9 Linux operating system. This cluster was used to run the XOOPIC simulations discussed in Chapter 3. It provided the necessary computing power for the simulations and made the task of running the required number of simulations possible. The cluster will continue to be useful in future projects involving XOOPIC and other computationally extensive programs.

A cluster is a group of computers that work together to complete a common task. It acts as a single computer with multiple processors. Table 9 provides an overview of the cluster specifications.

5	Pentium 4 3GHz w/ 512 MB memory, 80 GB hard drives, and Linksys 1Gbit Ethernet Cards
1	Monitor
1	Keyboard
1	Mouse
1	Netgear Gbit 5 port Hub
1	CD-RW drive installed in Node 1.

Table 10 - Linux cluster components.

Each of the computers, labeled nodes 1 through 5, is wired via CAT5e cable to the hub. The hub facilitates communication between the five computers. All interfacing with the cluster is done through a keyboard, mouse, monitor, and CD-RW drive connected to node 1 of the cluster.

The cluster was constructed using the following steps.

1. On nodes 2-5, Install RedHat 9
   a. Include Engineering and Scientific package, but not LAM
   b. Include KDE Desktop Enviroment
   c. Include Network Servers
   d. Include Development Tools
   e. Include Kernal Development and TK
   f. Include Admin and System Tools
2. Create an ECE account, "tigers" as password (without the quotes)
3. Log in as root, "tigers" as password (again, without the quotes)
   a. Edit file "/etc/sudoers", uncommented line beginning "%wheel"
   b. Add ECE to group wheel, set the password to not expire
4. Logout and Login as ECE.
   a. Install Linksys Gbit NIC drivers.
   b. Set firewall settings to "None" through "RedHat/System Settings/Security Level"
   c. Open the Network settings: "RedHat/System Settings/Network". Select "Statically Set IP Addresses." Set Address to 192.168.0.N, where N is 2-5 to represent the correct node. Set Subnet Mask to 255.255.255.0.
   d. Click on Hosts tab. Add the following new Host:
      1. Address: 192.168.0.1
      2. Hostname: node1.ece.missouri.edu
      3. Alias: node1
   e. Repeat for nodes 2-5 with appropriate address, hostname, and alias. All 5 hosts must be listed on each computer.
   f. Activate the NIC.
   g. If this is not the first computer, attempt to ping a previously configured node. If ping timeouts, recheck the steps.
   h. Edit "/etc/fstab" file and insert the following at the end:
      ```
      node1:/home        /home nfs      bg,rw,intr    0      0
      node2:/user/local  /usr/local     nfs           noauto,ro,soft
      node3:/mnt/cdrom   /mnt/cdrom     nfs           noauto,ro,soft
      ```
   i. Remove keyboard, mouse, CD-RW and Reboot
   j. Repeat for nodes 2-5.
5. For node 1, follow instructions 1 through 4.d, substituting a "1" where there was previously a 2, 3, 4, or 5.
   a. Activate the NIC and attempt to ping nodes 2-5.
   b. Edit file "/etc/xinetd.d/rsh". Change disable=yes to disable=no.
   c. Run command "/etc/rc.d/init.d/xinetd restart".
   d. Edit file "/etc/pam.d/rsh". Change the line:
      ```
      auth    required    /lib/security/pam_rhosts_auth.so
      ```
      to now read:
      ```
      auth    sufficient  /lib/security/pam_rhosts_auth.so
      ```

e. Edit file "/etc/pam.d/rlogin". Change the line:

> auth   required   /lib/security/pam_rhosts_auth.so

to now read:

> auth   sufficient   /lib/security/pam_rhosts_auth.so

f. Create new file "/etc/exports". Add the following:

> # /etc/exports file
> #allow nodes to mount /home
> /home node2(rw,no_root_squash) node3(rw,no_root_squash)
> node4(rw,no_root_squash) node5(rw,no_root_squash)
>
> #allow nodes to mount /usr/local
> /usr/local node2((rw,no_root_squash) node3(rw,no_root_squash)
> node4(rw,no_root_squash) node5(rw,no_root_squash)
>
> #allow nodes to mount /mnt/cdrom
> /mnt/cdrom node2(ro,no_root_squash) node3(ro,no_root_squash)
> node4(ro,no_root_squash) node5(ro,no_root_squash)

g. Run command "/etc/rc.d/init.d/nfs restart".

h. Run command "/etc/rc.d/init.d/network restart"

i. Enable NFS service on boot by going to "RedHat/System Settings/Server Settings/Services". Check the NFS service checkbox.

j. Type the command "rsh node2." If a password is required, review the previous steps. Be sure to check all nodes.

k. Login to each node and type the following commands

> mount /mnt/cdrom
> mount /usr/local
> mount /home

l. On node 1, install LAM 7, XGraphix, and XOOPIC.

m. Create a file in "/home/lamhosts". Add the following.

> node1.ece.missouri.edu
> node2.ece.missouri.edu
> node3.ece.missouri.edu
> node4.ece.missouri.edu
> node5.ece.missouri.edu

n. Run command "lamboot lamhosts –v" in the home directory.

These steps represent the process required to construct the cluster and are only required if the cluster must be rebuilt at some future point. Various guides can also be found on the internet, should this process prove insufficient. However, since this cluster is already in operation, the only steps that must be completed for a new project are steps 5.k and 5.n. These steps need to be performed when the cluster is rebooted.

Appendix II – Input Decks for XOOPIC Simulations

```
ltgsbase.inp
{
  .6mm x .3mm simulation.  1 atm, argon, 3 MV/m.
}
Variables
{
 Kmax = 512
 x1max = 0.0003
 x2max = 0.0006
 dx = x2max/Kmax
Jmax =Kmax*x1max/x2max
 tstep = 2.0E-12
randomseed = %%1
electronmass = 9.11e-31
electroncharge = -1.6e-19
singleioncharge = 1.6e-19
ionmass = 6.67e-26
maxnumber = 1e6
press=760
voltage=x2max*6e6/2
sourcex1=(x1max/2)-.02*x1max
sourcey1=0
sourcex2=(x1max/2)+.02*x1max
sourcey2=x2max
simpartsperreal=5e6
initialparts=0
rateparts=2
plasmarate=rateparts*simpartsperreal/((sourcex2-
sourcex1)*(sourcey2-sourcey1)*tstep)
loaddensity=initialparts*(2*simpartsperreal)/((sourcex2-
sourcex1)*(sourcey2-sourcey1))
DADI=1
Multigrid=4
PETSC=6
espoiflag=Multigrid
}
Region
{
Species
{
        name = electrons
        m = electronmass
        q = electroncharge
 collisionModel=1
 particleLimit=maxnumber
}
Species
{
        name = argon
```

```
        m = ionmass
        q = singleioncharge
 collisionModel=2
 particleLimit=maxnumber
}
Grid
{
 J = Jmax
 x1s = 0.0
 x1f = x1max
 n1 = 1.0
 K = Kmax
 x2s = 0.0
 x2f = x2max
 n2 = 1.0
Geometry = 1
}
Control
{
 dt = tstep
 ElectrostaticFlag = espoiflag
 np2cFactor=simpartsperreal
 presidue=1E-4
 Frandseed=randomseed
 }
MCC
{
 gas = Ar
 pressure = press
 eSpecies = electrons
 iSpecies = argon
}
Equipotential
{
 C = voltage
 phase = 0
 A1 = 0
 A2 = x2max
 B1 = x1max
 B2 = x2max
 name = Equipotential
 normal = -1
}
Conductor
{

 A1 = 0
 A2 = 0
 B1 = x1max
 B2 = 0
 name = Conductor
 normal = 1
 Secondary
 {
  secondary = 0.2
  secSpecies = electrons
  iSpecies = argon
```

```
 }
}
Dielectric
{
er = 1
normal= 1
A1=0
A2=0
B1=0
B2=x2max
}
Dielectric
{
er = 1
normal= -1
A1=x1max
A2=0
B1=x1max
B2=x2max
}
PlasmaSource
{
A1 = sourcex1
A2 = sourcey1
B1 = sourcex2
B2 = sourcey2
speciesName1 = electrons
speciesName2 = argon
sourceRate = plasmarate
np2c = simpartsperreal
analyticF = 1
}
Load
{
 x1MinMKS = sourcex1
 x1MaxMKS = sourcex2
 x2MinMKS = sourcey1
 x2MaxMKS = sourcey2
 speciesName = electrons
 density = loaddensity
 np2c = simpartsperreal
 LoadMethodFlag =1
 temperature = 5.93e5
}
}
```

XOOPIC uses an input file to change the conditions of the simulation and does

not require recompilation for every experimental change. The basic input file used in the

simulations is shown above. The code utilizes data input into this file to determine the

behavior of the plasma over a set amount of time. There are several factors that need to be defined in the input deck in order to create a simulation for streamer formation in a spark gap.

Two species were defined: the electrons and the ions. The electrons were given a standard electron mass of $9.11 \cdot 10^{-31}$ kg, and the ions were given a standard mass for Neon and Argon of $3.28 \cdot 10^{-26}$ kg and $6.67 \cdot 10^{-26}$ kg respectively. The electrons were given a charge of $-1.6022 \cdot 10^{-19}$ coulombs (C), and the ions were given a charge of $1.6022 \cdot 10^{-19}$ C. This ion charge was determined by assuming the ions only lost a single electron during ionization. A particle limit was imposed on both species to insure that the simulation did not get sluggish. When a particle limit was reached, the number of particles was halved and the number of real particles represented by each particle in the simulation was doubled. The kinetic model was designed with this limit in mind and was not affected by the species particle limit.

The grid determines the resolution of the simulation. All calculations made on the particles are in reference to their grid positions. A more refined mesh is required to resolve the Debye length of the plasma as discussed earlier. The number of grids in the J and K directions was given here. The kinetic model utilized 512 grids horizontally and 1024 grids vertically in the simulation space of 0.3 mm by 0.6 mm. This provided a grid size of approximately 0.5 µm.

The control section is where a number of parameters were defined. The time step determined how frequently calculations were made in the simulation. For a stable simulation, a time step of less than $1/20 f_{plasma}$ is needed. A time step of $2 \cdot 10^{-12}$ s was sufficient for simulating the spark gap. The electrostatic flag here determines the code

that was used by XOOPIC to solve Poisson's Equation, where ϕ is potential and ρ is charge density.

$$\nabla^2 \phi = \frac{-\rho}{\varepsilon_0}$$

(1)

Two choices of code were available, DADI and Multigrid. Multigrid was chosen because it appeared to be more stable. The Np2c Factor is the number of real particles that each simulated particle represents. This was chosen to be 10^6 for the simulations examining the intrinsic switch parameters, and $5 \cdot 10^6$ for the simulations examining the laser pulse parameters. A residue for the electrostatic solver is also defined here; this is the error range in which the solver is allowed to operate. A larger value will decrease the simulation time while a smaller value will give a more precise solution. The value chosen, 10^{-4}, was found to be acceptable. A larger allowed error value results in an incorrectly calculated electric field across the gap. A random seed was inserted here as well. This number provides a base for the random number generator in the code, which means that different numbers for this value will result in different random numbers generated by the random number generator. Different parameters for the random number generator allowed for several simulations to be run with identical initial conditions and resulted in a range of data to be interpreted.

Monte Carlo collisions are important in the kinetic model because of the number of collisions that occur in a spark gap. The code for the collisions determines the probability that a gas atom will be ionized if a collision takes place. The gas used and its pressure are also defined here. The choice of gasses included H, He, Li, Ar, Ne, and Xe. For the kinetic model, the noble gasses Neon and Argon were utilized. The particles that

92

result from a collision are defined in the species section discussed above. Note that the gas used here and the ion mass must be manually correlated.

The equipotential, conductor and dielectric sections define the simulation space of the model. Each was given a starting point and ending point as well as a normal vector pointed towards the inside of the simulation. The equipotential plane on the upper boundary has a normal of -1, which points downward. The conductor, which is the bottom grounded plane, has a normal of 1, which points upward.

The PlasmaSource section defines the position and rate at which ionized particles are injected into the simulation. This was used to simulate the laser pulse and the small amount of naturally occurring ionization that facilitates self-breaking. The position and area of the generated ionization was a rectangular region defined by two sets of coordinates. These coordinates were adjusted to indicate a change in shape and area of the laser pulse. The rate at which the ionization is generated was changed to indicate a difference in laser power. Converting laser power to ionization rate was discussed earlier.

The following "C" program was utilized to extract electron temperature, density, and streamer radius from a comma separated table generated by XOOPIC containing data on particle position on the x and y axis and particle velocity in the x and y direction.

```c
#include <stdio.h>

#include <stdlib.h>
#include <math.h>

#define OFF 0
#define ON 1
#define DEBUG ON

main()
{
        FILE *fp;
        char newline[100];
        int i,j,k,l,m,n,o,p,q,r;
        long particles, totalparticles;
        double x,y,vx,vy,vz,mean,total,top,stdev,variance;
        double electronmass, electroncharge, vsquared, energy, avgenergy;
        double density, avgke, avgtemp;
        double simpartsperreal = 5e6;
        double radius;

        fp = fopen("ltgs.csv","r");

        /* Round 1 -- Find Mean */

        electroncharge = 1.6022e-19;
        electronmass = 9.10938e-31;
        energy = 0;
        total=0;
        i=0;
        while (fscanf(fp,"%lf,%lf,%lf,%lf,%lf %*[^\n]",&x,&y,&vx,&vy,&vz) != EOF) {

                i++;
                total = total + x;

        /*      printf("%lf\t%d\n",x,i); */    }

        /* printf("%lf\n",total); */

        mean = total / i;
        totalparticles = i;

        /* Round 2 -- Find Standard Deviation */

        rewind(fp);
        top=0;
        while (fscanf(fp,"%lf,%lf,%lf,%lf,%lf %*[^\n]",&x,&y,&vx,&vy,&vz) != EOF) {

                top = (x-mean)*(x-mean) + top;

        /*      printf("%.12lf\n",top); */ }

        variance = top / i;
        stdev = sqrt(variance);

        /* Round 3 -- Find Density and Avg Electron Temp */

        rewind(fp);
        energy = 0;
        i=0; j=0; k=0; l=0; m=0; n=0; o=0; p=0; q=0; r=0;
        while (fscanf(fp,"%lf,%lf,%lf,%lf,%lf %*[^\n]}",&x,&y,&vx,&vy,&vz) != EOF) {
        if (x > mean - stdev && x < mean + stdev) {

        if (y >= 0 && y < .00006) i++;
        if (y >= .00006 && y < .00012) j++;
        if (y >= .00012 && y < .00018) k++;
        if (y >= .00018 && y < .00024) l++;
        if (y >= .00024 && y < .00030) m++;
        if (y >= .00030 && y < .00036) n++;
        if (y >= .00036 && y < .00042) o++;
        if (y >= .00042 && y < .00048) p++;
```

```
        if (y >= .00048 && y < .00054) q++;
        if (y >= .00054 && y < .00060) r++;

        vsquared = vx*vx + vy*vy + vz*vz;
        energy = (vsquared * .5 * electronmass) + energy;}}

        /* printf("%d %d %d %d %d %d %d %d %d %d\n",i,j,k,l,m,n,o,p,q,r); */

        particles = r+q+p+o+n+m;
        density = particles * simpartsperreal / (6 * .00006 * stdev);
        avgenergy = energy / (particles + l + k + j + i);
        avgke = (avgenergy / electroncharge);
        avgtemp = avgke * 2/3;

        /* printf("%e\n",avgtemp); */

        fclose(fp);

        radius = stdev * 1000000;

        fp = fopen("results", "a+");

        if (fscanf(fp,"%*[^\n]") == EOF) {
        fprintf(fp,"Simulation:\t.6mm x .3mm, 760 torr, 1800V, Argon\n");
        fprintf(fp,"\tRadius\t\tDensity\t\tTemperature\tParticles\n");}
        fprintf(fp,"\t%.2lf microns\t%.4e\t%.2lf
eV\t\t%d\n",radius,density,avgtemp,totalparticles);

        fclose(fp);

        return(0);
}
```

Appendix III – Switch Parameter Variance Results

Simulation:		.6mm x .3mm, 760 torr, 1200V, Argon				
		Radius (µm)	Density (m^{-3})	Temperature (eV)	Particles	Conductivity (mho/m)
		42.96	1.00E+19	2.83	57444	1.04
		41.14	1.07E+19	2.89	57393	1.10
		41.62	1.07E+19	2.83	59475	1.11
		41.91	1.02E+19	2.85	55819	1.05
		42.52	1.01E+19	2.90	57158	1.04
		41.36	1.04E+19	2.83	58672	1.08
		42.13	1.04E+19	2.86	57050	1.07
		42.65	1.01E+19	2.89	56651	1.03
		42.97	9.86E+18	2.83	57109	1.02
		41.07	1.06E+19	2.91	58101	1.09
Average		42.03	1.03E+19	2.86		1.06
Range	+	0.94	4.00E+17	0.05		0.05
	-	0.96	4.50E+17	0.03		0.04

Simulation:		.6mm x .3mm, 760 torr, 1500V, Argon				
		Radius (µm)	Density (m^{-3})	Temperature (eV)	Particles	Conductivity (mho/m)
		47.20	1.51E+19	2.92	87816	1.54
		44.63	1.65E+19	2.87	89311	1.70
		46.97	1.54E+19	2.85	88789	1.59
		43.85	1.67E+19	2.88	90708	1.72
		45.98	1.59E+19	2.83	89594	1.65
		45.62	1.58E+19	2.82	86161	1.64
		45.43	1.60E+19	2.88	89617	1.64
		46.33	1.61E+19	2.79	95631	1.68
		47.06	1.51E+19	2.90	89545	1.55
		44.72	1.64E+19	2.88	92316	1.68
Average		45.78	1.59E+19	2.86		1.64
Range	+	1.42	8.29E+17	0.06		0.08
	-	1.93	7.81E+17	0.07		0.10

Simulation:		.6mm x .3mm, 760 torr, 1800V, Argon				
		Radius (µm)	Density (m^{-3})	Temperature (eV)	Particles	Conductivity (mho/m)
		48.08	2.20E+19	2.95	124044	2.23
		47.42	2.28E+19	2.92	128421	2.33
		49.31	2.12E+19	2.88	122158	2.18
		48.69	2.16E+19	2.93	123049	2.20
		46.77	2.30E+19	2.88	126903	2.37
		48.43	2.16E+19	2.85	122620	2.23
		47.63	2.16E+19	2.79	118175	2.26
		48.48	2.19E+19	2.85	126465	2.26
		48.58	2.19E+19	2.82	125514	2.27
		48.83	2.18E+19	2.86	128753	2.24
Average		48.22	2.20E+19	2.87		2.26
Range	+	1.09	1.09E+18	0.08		0.11
	-	1.45	7.11E+17	0.08		0.08

Simulation:		.6mm x .3mm, 760 torr, 2100V, Argon				
		Radius (µm)	Density (m^{-3})	Temperature (eV)	Particles	Conductivity (mho/m)
		49.35	2.90E+19	2.89	162549	2.97
		48.77	2.98E+19	2.93	163624	3.04
		50.17	2.84E+19	2.84	161939	2.93
		49.83	2.81E+19	2.86	156303	2.90
		49.92	2.77E+19	2.94	155338	2.82
		49.48	2.79E+19	2.89	154066	2.86
		50.44	2.76E+19	3.02	159342	2.77
		50.81	2.73E+19	2.94	158600	2.78
		50.78	2.68E+19	2.89	154139	2.75
		50.29	2.84E+19	2.84	163721	2.94
Average		49.98	2.81E+19	2.90		2.88
Range	+	0.83	1.72E+18	0.12		0.16
	-	1.21	1.27E+18	0.06		0.12

Simulation: .6mm x .3mm, 760 torr, 2400V, Argon

		Radius (μm)	Density (m^{-3})	Temperature (eV)	Particles	Conductivity (mho/m)
		51.57	3.30E+19	2.94	188139	3.35
		49.90	3.56E+19	2.92	194299	3.63
		49.53	3.64E+19	2.89	197249	3.73
		50.56	3.41E+19	2.84	187042	3.53
		51.28	3.38E+19	2.85	189367	3.49
		50.61	3.38E+19	2.90	186372	3.46
		51.63	3.35E+19	2.97	190629	3.38
		52.50	3.26E+19	2.88	190931	3.35
		50.08	3.51E+19	2.85	192274	3.63
		50.51	3.58E+19	2.90	200083	3.67
Average		50.82	3.44E+19	2.89		3.52
Range	+	1.68	2.05E+18	0.08		0.21
	-	1.29	1.76E+18	0.05		0.17

Simulation: .6mm x .3mm, 760 torr, 2700V, Argon

		Radius (μm)	Density (m^{-3})	Temperature (eV)	Particles	Conductivity (mho/m)
		51.77	4.13E+19	2.91	233599	4.22
		53.08	3.80E+19	2.90	219724	3.89
		51.84	3.96E+19	2.94	221981	4.02
		51.27	4.12E+19	2.95	227457	4.18
		51.23	4.25E+19	2.91	238810	4.35
		51.95	3.91E+19	2.88	220232	4.02
		51.39	4.13E+19	2.91	228473	4.22
		51.96	4.00E+19	2.88	225519	4.11
		52.80	3.79E+19	2.90	217834	3.88
		52.40	3.92E+19	3.03	222907	3.92
Average		51.97	4.00E+19	2.92		4.08
Range	+	1.11	2.52E+18	0.11		0.26
	-	0.74	2.11E+18	0.04		0.20

Simulation: .6mm x .3mm, 760 torr, 3000V, Argon

		Radius (μm)	Density (m^{-3})	Temperature (eV)	Particles	Conductivity (mho/m)
		52.60	4.63E+19	2.89	262151	4.74
		51.26	4.70E+19	2.90	256736	4.82
		52.63	4.55E+19	3.00	257647	4.58
		52.19	4.71E+19	3.05	263543	4.70
		52.83	4.37E+19	2.96	247173	4.43
		52.20	4.41E+19	2.98	246242	4.46
		52.12	4.57E+19	2.87	255418	4.70
		53.45	4.36E+19	2.87	251866	4.49
		53.95	4.10E+19	2.89	238028	4.20
		52.73	4.39E+19	3.02	248127	4.40
Average		52.60	4.48E+19	2.94		4.55
Range	+	1.35	2.26E+18	0.11		0.26
	-	1.34	3.82E+18	0.07		0.35

Simulation: .6mm x .3mm, 1140 torr, 1200V, Argon

		Radius (μm)	Density (m^{-3})	Temperature (eV)	Particles	Conductivity (mho/m)
		42.85	1.01E+19	2.83	58823	1.05
		41.89	1.07E+19	2.84	59749	1.10
		40.97	1.08E+19	2.86	59572	1.11
		41.77	1.05E+19	2.89	57813	1.07
		41.62	1.06E+19	2.86	58018	1.09
		42.14	1.02E+19	2.80	57037	1.07
		43.15	1.00E+19	2.90	61947	1.03
		43.20	9.86E+18	2.91	56887	1.01
		43.15	9.98E+18	2.92	58727	1.02
		42.89	1.00E+19	2.88	55807	1.03
Average		42.36	1.03E+19	2.87		1.06
Range	+	0.84	5.08E+17	0.05		0.05
	-	1.39	4.15E+17	0.07		0.05

Simulation: .6mm x .3mm, 1140 torr, 1500V, Argon

		Radius (μm)μ	Density (m^{-3})	Temperature (eV)	Particles	Conductivity (mho/m)
		45.79	1.58E+19	2.88	89900	1.62
		45.41	1.58E+19	2.86	86675	1.63
		46.29	1.58E+19	2.89	91716	1.62
		45.40	1.63E+19	2.93	92388	1.66
		45.82	1.53E+19	2.95	84478	1.55
		44.81	1.65E+19	2.85	93595	1.71
		46.03	1.59E+19	2.79	91972	1.66
		43.74	1.69E+19	2.83	93325	1.75
		46.64	1.59E+19	2.95	91040	1.61
		45.14	1.62E+19	2.81	89122	1.68
Average		45.51	1.60E+19	2.87		1.65
Range	+	1.13	8.91E+17	0.08		0.10
	-	1.77	7.84E+17	0.08		0.10

Simulation: .6mm x .3mm, 1140 torr, 1800V, Argon

		Radius (μm)	Density (m^{-3})	Temperature (eV)	Particles	Conductivity (mho/m)
		48.84	2.14E+19	2.85	123566	2.21
		46.78	2.29E+19	2.86	127023	2.36
		48.04	2.22E+19	2.81	126386	2.31
		49.24	2.11E+19	2.79	122359	2.21
		47.73	2.22E+19	2.93	123890	2.26
		47.63	2.21E+19	2.87	121699	2.27
		46.44	2.26E+19	2.87	121846	2.33
		49.44	2.11E+19	2.99	123864	2.13
		48.07	2.21E+19	2.82	126795	2.30
		48.14	2.22E+19	2.86	124293	2.28
Average		48.04	2.20E+19	2.87		2.27
Range	+	1.41	8.97E+17	0.13		0.09
	-	1.60	8.57E+17	0.07		0.13

Simulation: .6mm x .3mm, 1140 torr, 2100V, Argon

		Radius (μm)	Density (m^{-3})	Temperature (eV)	Particles	Conductivity (mho/m)
		50.23	2.76E+19	2.93	159697	2.81
		49.97	2.83E+19	2.83	160599	2.94
		50.94	2.71E+19	2.93	157357	2.76
		48.73	2.95E+19	2.92	162483	3.01
		50.06	2.83E+19	2.89	160786	2.90
		48.92	2.89E+19	2.83	159768	2.99
		49.61	2.89E+19	2.92	162232	2.95
		50.61	2.83E+19	2.88	164246	2.91
		51.03	2.69E+19	2.85	155324	2.78
		47.63	3.00E+19	2.87	159171	3.09
Average		49.77	2.84E+19	2.89		2.91
Range	+	1.26	1.65E+18	0.04		0.18
	-	2.14	1.49E+18	0.06		0.16

Simulation: .6mm x .3mm, 1140 torr, 2400V, Argon

		Radius (μm)	Density (m^{-3})	Temperature (eV)	Particles	Conductivity (mho/m)
		51.05	3.39E+19	2.85	189669	3.49
		52.16	3.33E+19	3.03	190891	3.34
		49.47	3.55E+19	2.85	190064	3.67
		51.69	3.38E+19	3.09	192691	3.35
		51.33	3.44E+19	2.91	194310	3.52
		50.28	3.44E+19	2.89	188503	3.53
		50.51	3.46E+19	2.91	190383	3.54
		50.73	3.47E+19	2.92	194872	3.54
		51.45	3.42E+19	2.84	193611	3.54
		50.96	3.46E+19	2.90	192818	3.54
Average		50.96	3.43E+19	2.92		3.50
Range	+	1.20	1.17E+18	0.17		0.16
	-	1.49	1.02E+18	0.08		0.17

Simulation: .6mm x .3mm, 1140 torr, 2700V, Argon

		Radius (µm)	Density (m^{-3})	Temperature (eV)	Particles	Conductivity (mho/m)
		52.49	3.94E+19	2.98	224558	3.98
		51.44	4.10E+19	2.94	229852	4.17
		51.46	4.11E+19	2.90	229489	4.20
		51.65	4.04E+19	2.99	224217	4.07
		52.35	3.98E+19	2.89	224986	4.08
		50.88	4.17E+19	2.94	228976	4.24
		52.94	3.83E+19	3.03	220532	3.83
		53.23	3.84E+19	3.06	222524	3.82
		52.41	3.83E+19	2.90	219578	3.92
		54.05	3.70E+19	2.98	218416	3.73
Average		52.29	3.95E+19	2.96		4.00
Range	+	1.76	2.17E+18	0.10		0.23
	-	1.41	2.56E+18	0.07		0.27

Simulation: .6mm x .3mm, 1140 torr, 3000V, Argon

		Radius (µm)	Density (m^{-3})	Temperature (eV)	Particles	Conductivity (mho/m)
		51.37	4.56E+19	2.90	248508	4.67
		54.51	4.41E+19	2.88	261061	4.52
		51.76	4.56E+19	2.94	252225	4.64
		53.03	4.53E+19	2.91	258687	4.63
		53.01	4.48E+19	2.99	255566	4.52
		51.92	4.56E+19	2.92	252813	4.65
		52.04	4.68E+19	2.93	262383	4.77
		53.13	4.29E+19	2.98	245203	4.33
		54.67	4.26E+19	2.92	252249	4.34
		54.08	4.56E+19	2.95	267882	4.63
Average		52.95	4.49E+19	2.93		4.57
Range	+	1.72	1.93E+18	0.06		0.20
	-	1.58	2.33E+18	0.05		0.24

Simulation: .6mm x .3mm, 760 torr, 1200V, Neon

		Radius (µm)	Density (m^{-3})	Temperature (eV)	Particles	Conductivity (mho/m)
		43.95	7.66E+18	4.05	37760	0.66
		42.43	7.93E+18	4.03	36934	0.69
		43.43	7.79E+18	3.94	37633	0.68
		43.23	7.54E+18	4.05	35128	0.65
		42.14	8.13E+18	4.02	38858	0.71
		42.73	7.80E+18	4.01	37325	0.68
		43.08	7.82E+18	4.12	37347	0.67
		42.67	7.79E+18	4.09	36776	0.67
		44.40	7.31E+18	4.13	35269	0.63
		42.58	7.94E+18	4.17	37677	0.68
Average		43.06	7.77E+18	4.06		0.67
Range	+	1.34	3.61E+17	0.11		0.03
	-	0.92	4.61E+17	0.12		0.05

Simulation: .6mm x .3mm, 760 torr, 1500V, Neon

		Radius (µm)	Density (m^{-3})	Temperature (eV)	Particles	Conductivity (mho/m)
		45.32	1.26E+19	4.07	64403	1.09
		45.93	1.19E+19	4.00	59921	1.04
		45.97	1.21E+19	4.09	61187	1.04
		46.62	1.16E+19	3.98	59607	1.01
		45.34	1.20E+19	4.00	60956	1.05
		46.76	1.17E+19	4.02	60858	1.02
		45.49	1.20E+19	4.01	60307	1.05
		44.41	1.24E+19	4.04	59954	1.07
		44.63	1.23E+19	3.89	60945	1.09
		45.25	1.22E+19	4.02	61236	1.06
Average		45.57	1.21E+19	4.01		1.05
Range	+	1.19	5.28E+17	0.08		0.04
	-	1.16	4.52E+17	0.12		0.04

Simulation: .6mm x .3mm, 760 torr, 1800V, Neon

		Radius (μm)	Density (m^{-3})	Temperature (eV)	Particles	Conductivity (mho/m)
		47.87	1.64E+19	3.96	86829	1.44
		46.55	1.71E+19	3.96	86736	1.50
		46.40	1.75E+19	4.12	89520	1.50
		47.24	1.71E+19	3.97	89140	1.50
		46.32	1.75E+19	4.01	89754	1.53
		47.25	1.69E+19	4.10	88198	1.46
		47.15	1.70E+19	3.94	88232	1.49
		47.20	1.65E+19	4.10	84765	1.42
		47.00	1.72E+19	4.02	88610	1.50
		48.13	1.67E+19	4.01	88742	1.45
Average		47.11	1.70E+19	4.02		1.48
Range	+	1.02	5.39E+17	0.10		0.05
	-	0.79	5.55E+17	0.08		0.06

Simulation: .6mm x .3mm, 760 torr, 2100V, Neon

		Radius (μm)	Density (m^{-3})	Temperature (eV)	Particles	Conductivity (mho/m)
		47.61	2.33E+19	4.06	121235	2.02
		49.69	2.13E+19	4.04	115480	1.85
		48.39	2.27E+19	4.02	119170	1.97
		49.00	2.18E+19	3.98	115996	1.91
		48.40	2.27E+19	4.07	121366	1.96
		48.59	2.26E+19	3.97	121373	1.98
		49.77	2.17E+19	4.06	119508	1.88
		48.66	2.24E+19	4.09	119762	1.93
		49.32	2.12E+19	4.01	113231	1.85
		47.47	2.27E+19	4.00	117159	1.98
Average		48.69	2.23E+19	4.03		1.93
Range	+	1.08	1.05E+18	0.06		0.08
	-	1.22	1.04E+18	0.06		0.09

Simulation: .6mm x .3mm, 760 torr, 2400V, Neon

		Radius (μm)	Density (m^{-3})	Temperature (eV)	Particles	Conductivity (mho/m)
		49.51	2.81E+19	4.06	150914	2.43
		49.02	2.81E+19	4.12	148216	2.41
		50.09	2.74E+19	4.06	148297	2.37
		50.85	2.78E+19	4.08	154997	2.40
		49.98	2.69E+19	4.11	145126	2.31
		51.27	2.69E+19	4.10	151090	2.32
		49.68	2.74E+19	4.28	147329	2.31
		48.45	2.76E+19	4.04	141678	2.39
		50.37	2.75E+19	4.14	151140	2.36
		50.33	2.80E+19	4.26	154066	2.36
Average		49.96	2.76E+19	4.13		2.37
Range	+	1.32	5.74E+17	0.16		0.07
	-	1.51	6.90E+17	0.09		0.06

Simulation: .6mm x .3mm, 760 torr, 2700V, Neon

		Radius (μm)	Density (m^{-3})	Temperature (eV)	Particles	Conductivity (mho/m)
		50.01	3.42E+19	4.09	183159	2.94
		50.42	3.36E+19	4.15	182218	2.88
		50.22	3.32E+19	4.04	177967	2.88
		50.07	3.31E+19	4.09	176240	2.86
		51.97	3.17E+19	4.02	178087	2.76
		51.15	3.19E+19	4.09	174987	2.75
		51.05	3.21E+19	4.05	175394	2.78
		51.11	3.33E+19	4.19	184742	2.84
		50.25	3.32E+19	4.18	178300	2.83
		50.08	3.34E+19	4.11	179146	2.87
Average		50.63	3.30E+19	4.10		2.84
Range	+	1.34	1.18E+18	0.09		0.11
	-	0.62	1.23E+18	0.08		0.09

Simulation: .6mm x .3mm, 760 torr, 3000V, Neon

Radius (µm)	Density (m^{-3})	Temperature (eV)	Particles	Conductivity (mho/m)
50.40	3.92E+19	4.31	209063	3.29
51.71	3.79E+19	4.18	209746	3.23
51.37	3.84E+19	4.16	210292	3.28
51.04	3.89E+19	4.17	211577	3.32
51.35	3.87E+19	4.18	212748	3.30
51.26	3.99E+19	4.21	219025	3.39
51.10	3.75E+19	4.10	203537	3.22
52.04	3.85E+19	4.15	214679	3.29
51.93	3.87E+19	4.10	217361	3.33
50.22	4.03E+19	4.14	215333	3.45

		Radius	Density	Temperature		Conductivity
Average		51.24	3.88E+19	4.17		3.31
Range	+	0.80	1.53E+18	0.14		0.14
	-	1.02	1.34E+18	0.07		0.09

Simulation: .6mm x .3mm, 1140 torr, 1200V, Neon

Radius (µm)	Density (m^{-3})	Temperature (eV)	Particles	Conductivity (mho/m)
41.52	8.02E+18	4.14	36095	0.69
42.08	8.15E+18	4.03	38544	0.71
43.88	7.53E+18	4.15	36570	0.64
43.94	7.44E+18	4.04	35709	0.65
43.91	7.89E+18	4.08	39773	0.68
43.20	7.62E+18	4.00	36317	0.66
42.19	7.92E+18	4.01	36825	0.69
42.57	7.79E+18	3.90	36432	0.69
43.42	7.46E+18	4.05	35060	0.65
43.83	7.47E+18	4.05	36629	0.65

		Radius	Density	Temperature		Conductivity
Average		43.05	7.73E+18	4.05		0.67
Range	+	0.89	4.26E+17	0.11		0.04
	-	1.53	2.90E+17	0.14		0.03

Simulation: .6mm x .3mm, 1140 torr, 1500V, Neon

Radius (µm)	Density (m^{-3})	Temperature (eV)	Particles	Conductivity (mho/m)
45.10	1.20E+19	3.94	59237	1.05
44.68	1.21E+19	3.97	58782	1.05
46.02	1.18E+19	3.95	60328	1.04
46.16	1.15E+19	4.08	57949	1.00
45.88	1.19E+19	4.02	60739	1.03
46.18	1.18E+19	3.93	59861	1.03
46.35	1.13E+19	4.03	56941	0.98
44.18	1.22E+19	4.02	57952	1.06
44.85	1.17E+19	4.02	57237	1.02
44.64	1.23E+19	4.02	61145	1.07

		Radius	Density	Temperature		Conductivity
Average		45.40	1.19E+19	4.00		1.03
Range	+	0.95	4.42E+17	0.08		0.04
	-	1.22	5.48E+17	0.07		0.05

Simulation: .6mm x .3mm, 1140 torr, 1800V, Neon

Radius (µm)	Density (m^{-3})	Temperature (eV)	Particles	Conductivity (mho/m)
47.57	1.67E+19	4.08	87673	1.44
47.00	1.71E+19	4.00	88501	1.49
46.80	1.68E+19	4.09	84862	1.45
46.96	1.72E+19	3.97	89548	1.51
46.78	1.75E+19	4.04	91060	1.52
47.76	1.66E+19	4.00	87324	1.45
46.83	1.73E+19	4.06	89654	1.50
47.06	1.65E+19	3.95	83700	1.45
46.17	1.73E+19	4.11	86655	1.49
46.10	1.78E+19	3.92	91022	1.57

		Radius	Density	Temperature		Conductivity
Average		46.90	1.71E+19	4.02		1.49
Range	+	0.86	7.20E+17	0.09		0.08
	-	0.80	5.81E+17	0.10		0.04

Simulation: .6mm x .3mm, 1140 torr, 2100V, Neon

	Radius (μm)	Density (m^{-3})	Temperature (eV)	Particles	Conductivity (mho/m)
	48.48	2.25E+19	4.11	119470	1.93
	47.03	2.28E+19	3.94	115437	2.00
	47.80	2.29E+19	4.07	119247	1.98
	48.50	2.31E+19	4.08	122237	1.99
	48.48	2.26E+19	4.08	118705	1.95
	49.62	2.11E+19	4.19	114215	1.80
	49.21	2.13E+19	4.00	113826	1.86
	48.93	2.23E+19	4.08	120323	1.93
	49.52	2.20E+19	4.07	119407	1.90
	48.42	2.24E+19	4.03	119081	1.95
Average	48.60	2.23E+19	4.07		1.93
Range +	1.02	7.61E+17	0.13		0.08
−	1.57	1.18E+18	0.13		0.13

Simulation: .6mm x .3mm, 1140 torr, 2400V, Neon

	Radius (μm)	Density (m^{-3})	Temperature (eV)	Particles	Conductivity (mho/m)
	49.54	2.74E+19	4.02	145152	2.38
	49.88	2.82E+19	4.09	153110	2.43
	49.69	2.77E+19	4.04	148924	2.40
	49.52	2.86E+19	4.08	155203	2.47
	49.88	2.79E+19	4.11	150684	2.40
	49.88	2.79E+19	4.08	150768	2.41
	49.34	2.80E+19	4.16	149489	2.40
	48.54	2.92E+19	4.07	151990	2.52
	49.57	2.88E+19	4.06	155556	2.49
	49.59	2.75E+19	4.13	147847	2.36
Average	49.54	2.81E+19	4.08		2.42
Range +	0.34	1.08E+18	0.08		0.10
−	1.00	7.36E+17	0.06		0.07

Simulation: .6mm x .3mm, 1140 torr, 2700V, Neon

	Radius (μm)	Density (m^{-3})	Temperature (eV)	Particles	Conductivity (mho/m)
	50.39	3.42E+19	4.09	185316	2.95
	51.20	3.29E+19	4.19	181645	2.80
	50.44	3.32E+19	4.03	179594	2.89
	51.28	3.23E+19	4.08	177961	2.79
	50.91	3.33E+19	4.06	182028	2.88
	51.61	3.26E+19	4.18	182186	2.78
	50.54	3.37E+19	4.07	183096	2.91
	51.14	3.28E+19	4.09	180393	2.82
	50.77	3.31E+19	4.16	181348	2.83
	51.71	3.28E+19	4.10	184149	2.82
Average	51.00	3.31E+19	4.11		2.85
Range +	0.71	1.11E+18	0.09		0.10
−	0.61	7.53E+17	0.08		0.07

Simulation: .6mm x .3mm, 1140 torr, 3000V, Neon

	Radius (μm)	Density (m^{-3})	Temperature (eV)	Particles	Conductivity (mho/m)
	51.30	3.79E+19	4.26	208043	3.20
	50.43	3.87E+19	4.08	207567	3.34
	51.28	3.92E+19	4.10	215963	3.38
	51.44	3.87E+19	4.08	213393	3.34
	52.25	3.88E+19	4.27	218946	3.27
	50.15	4.02E+19	4.17	213053	3.43
	51.56	3.84E+19	4.25	212027	3.25
	51.64	3.93E+19	4.15	218446	3.36
	50.88	3.98E+19	4.16	216655	3.40
	51.55	3.91E+19	4.14	215914	3.35
Average	51.25	3.90E+19	4.17		3.33
Range +	1.00	1.22E+18	0.10		0.10
−	1.10	1.09E+18	0.09		0.13

Appendix IV – Triggering Laser Spot Variance Results

Simulation: 1200 µm², 15 mJ, Vertical

	Radius (µm)	Density (m^{-3})	Temperature (eV)	Particles	Conductivity (mho/m)
	48.28	2.15E+19	2.90	139009	2.20
	48.83	2.13E+19	2.89	139631	2.19
	46.69	2.26E+19	2.90	141637	2.32
	48.56	2.14E+19	2.87	141818	2.20
	47.98	2.18E+19	2.89	138581	2.23
	48.14	2.16E+19	2.91	140507	2.21
	48.10	2.18E+19	2.93	137191	2.22
	47.98	2.18E+19	2.90	140638	2.24
	48.28	2.16E+19	2.93	140705	2.20
	47.66	2.19E+19	2.88	139831	2.24
Average:	48.05	2.17E+19	2.90		2.22
Range +	0.78	8.92E+17	0.03		0.09
-	1.36	4.08E+17	0.03		0.04

Simulation: 2400 µm2, 15 mJ, Vertical

	Radius (µm)	Density (m^{-3})	Temperature (eV)	Particles	Conductivity (mho/m)
	48.96	2.31E+19	2.93	166852	2.35
	48.93	2.32E+19	2.92	165230	2.37
	49.16	2.28E+19	2.93	162507	2.33
	49.81	2.29E+19	2.92	165449	2.33
	50.24	2.22E+19	2.88	163187	2.28
	50.16	2.19E+19	2.92	162836	2.24
	49.55	2.27E+19	2.88	165168	2.33
	50.12	2.18E+19	2.96	165098	2.21
	49.32	2.28E+19	2.89	167568	2.34
	49.47	2.31E+19	2.95	169265	2.35
Average:	49.57	2.27E+19	2.92		2.31
Range +	0.67	5.76E+17	0.04		0.06
-	0.64	8.15E+17	0.04		0.10

Simulation: 3600 µm², 15 mJ, Vertical

	Radius (µm)	Density (m^{-3})	Temperature (eV)	Particles	Conductivity (mho/m)
	49.53	2.22E+19	2.91	147283	2.27
	48.91	2.25E+19	2.90	144155	2.31
	48.14	2.26E+19	2.96	141131	2.29
	48.90	2.26E+19	2.88	143629	2.32
	48.30	2.26E+19	2.86	140448	2.33
	48.78	2.24E+19	2.84	139948	2.31
	50.05	2.14E+19	2.91	135687	2.18
	48.87	2.23E+19	2.90	141071	2.28
	48.69	2.23E+19	2.89	135909	2.29
	49.41	2.20E+19	2.85	142344	2.27
Average:	48.96	2.23E+19	2.89		2.29
Range +	1.09	3.37E+17	0.07		0.04
-	0.82	9.37E+17	0.05		0.10

Simulation: 4800 µm², 15 mJ, Vertical

	Radius (µm)	Density (m^{-3})	Temperature (eV)	Particles	Conductivity (mho/m)
	49.02	2.15E+19	2.87	128297	2.22
	48.41	2.17E+19	2.86	126394	2.24
	49.25	2.13E+19	2.89	127065	2.18
	48.12	2.26E+19	2.83	132454	2.34
	47.89	2.25E+19	2.89	129292	2.30
	50.65	2.06E+19	2.86	129183	2.12
	48.05	2.19E+19	2.85	126123	2.26
	50.03	2.09E+19	2.88	129125	2.15
	49.80	2.10E+19	2.86	128381	2.16
	47.86	2.27E+19	2.88	133124	2.33
Average:	48.91	2.17E+19	2.87		2.23
Range +	1.74	1.06E+18	0.02		0.11
-	1.05	1.07E+18	0.04		0.11

Simulation: 1200 µm², 60 mJ, Vertical

Radius (µm)	Density (m^{-3})	Temperature (eV)	Particles	Conductivity (mho/m)
46.15	2.26E+19	2.92	194067	2.31
46.81	2.18E+19	2.93	192797	2.22
47.06	2.18E+19	2.93	193794	2.22
47.09	2.20E+19	2.93	194789	2.24
47.63	2.16E+19	2.94	194125	2.19
47.08	2.17E+19	2.94	193908	2.21
47.24	2.18E+19	2.94	193026	2.22
46.37	2.26E+19	2.92	195127	2.31
46.75	2.22E+19	2.93	194467	2.26
47.07	2.18E+19	2.92	194129	2.22
Average:	46.93	2.20E+19	2.93		2.24
Range +	0.71	6.13E+17	0.01		0.07
−	0.77	3.98E+17	0.01		0.04

Simulation: 2400 µm², 60 mJ, Vertical

Radius (µm)	Density (m^{-3})	Temperature (eV)	Particles	Conductivity (mho/m)
48.33	2.56E+19	2.96	246226	2.60
49.11	2.44E+19	2.94	239553	2.48
48.64	2.49E+19	2.96	243976	2.53
48.88	2.48E+19	2.95	244959	2.52
48.36	2.53E+19	2.95	242082	2.56
49.15	2.47E+19	2.96	247245	2.50
49.50	2.47E+19	2.98	244157	2.49
49.03	2.46E+19	2.96	245298	2.49
48.91	2.45E+19	2.97	242391	2.47
48.37	2.49E+19	2.96	242955	2.52
Average:	48.83	2.48E+19	2.96		2.52
Range +	0.67	8.17E+17	0.02		0.08
−	0.50	4.33E+17	0.02		0.04

Simulation: 3600 µm², 60 mJ, Vertical

Radius (µm)	Density (m^{-3})	Temperature (eV)	Particles	Conductivity (mho/m)
48.05	2.46E+19	2.90	205427	2.52
47.71	2.51E+19	2.90	206075	2.57
48.77	2.43E+19	2.89	205868	2.49
48.54	2.44E+19	2.93	206068	2.49
48.24	2.51E+19	2.89	206789	2.58
47.87	2.48E+19	2.89	203417	2.54
47.89	2.44E+19	2.89	201282	2.51
47.93	2.46E+19	2.93	204768	2.50
47.85	2.53E+19	2.91	208783	2.58
47.98	2.47E+19	2.91	203358	2.53
Average:	48.08	2.47E+19	2.90		2.53
Range +	0.69	5.13E+17	0.03		0.05
−	0.37	4.25E+17	0.01		0.04

Simulation: 4800 µm², 60 mJ, Vertical

Radius (µm)	Density (m^{-3})	Temperature (eV)	Particles	Conductivity (mho/m)
47.78	2.53E+19	2.86	190620	2.61
47.96	2.51E+19	2.90	194920	2.57
47.18	2.55E+19	2.90	191562	2.61
48.36	2.40E+19	2.91	185632	2.46
47.19	2.53E+19	2.88	190355	2.60
47.94	2.45E+19	2.88	188255	2.52
46.85	2.61E+19	2.91	191856	2.67
47.30	2.56E+19	2.87	191027	2.63
46.81	2.59E+19	2.91	193448	2.64
47.55	2.55E+19	2.89	193366	2.61
Average:	47.49	2.53E+19	2.89		2.59
Range +	0.87	8.34E+17	0.02		0.08
−	0.68	1.26E+18	0.03		0.14

Simulation: 1200 µm^2, 15 mJ, Horizontal

		Radius (µm)	Density (m^{-3})	Temperature (eV)	Particles	Conductivity (mho/m)
		48.10	2.16E+19	2.88	135473	2.22
		49.10	2.08E+19	2.91	134083	2.13
		48.44	2.14E+19	2.90	135510	2.19
		47.57	2.20E+19	2.91	135301	2.25
		48.38	2.14E+19	2.88	134971	2.19
		47.90	2.13E+19	2.89	133221	2.18
		48.52	2.12E+19	2.91	136340	2.16
		48.94	2.09E+19	2.90	134104	2.14
		47.40	2.21E+19	2.87	135951	2.27
		48.86	2.09E+19	2.91	134608	2.14
Average:		48.32	2.14E+19	2.90		2.19
Range	+	0.78	7.03E+17	0.01		0.08
	-	0.92	5.19E+17	0.03		0.06

Simulation: 2400 µm^2, 15 mJ, Horizontal

		Radius (µm)	Density (m^{-3})	Temperature (eV)	Particles	Conductivity (mho/m)
		49.40	2.14E+19	2.88	141465	2.20
		51.07	2.04E+19	2.87	137312	2.10
		50.40	2.10E+19	2.89	141457	2.16
		49.85	2.12E+19	2.89	139791	2.17
		50.79	2.05E+19	2.90	139221	2.10
		51.34	2.00E+19	2.89	139467	2.05
		50.19	2.09E+19	2.86	142323	2.16
		51.79	2.00E+19	2.89	139649	2.06
		51.45	2.03E+19	2.91	140297	2.08
		51.11	2.02E+19	2.93	139618	2.06
Average:		50.74	2.06E+19	2.89		2.11
Range	+	1.05	7.85E+17	0.04		0.08
	-	1.34	5.96E+17	0.03		0.06

Simulation: 3600 µm^2, 15 mJ, Horizontal

		Radius (µm)	Density (m^{-3})	Temperature (eV)	Particles	Conductivity (mho/m)
		55.11	1.93E+19	2.89	143755	1.98
		54.94	1.92E+19	2.90	142101	1.97
		54.14	1.97E+19	2.89	141918	2.02
		55.65	1.90E+19	2.89	143516	1.95
		54.58	1.93E+19	2.91	144243	1.98
		54.26	1.97E+19	2.90	143761	2.01
		54.46	1.94E+19	2.89	143190	1.99
		54.82	1.91E+19	2.90	143394	1.96
		54.54	1.93E+19	2.91	142794	1.97
		56.01	1.87E+19	2.90	143330	1.91
Average:		54.85	1.93E+19	2.90		1.97
Range	+	1.16	4.21E+17	0.01		0.05
	-	0.71	5.63E+17	0.01		0.06

Simulation: 4800 µm^2, 15 mJ, Horizontal

		Radius (µm)	Density (m^{-3})	Temperature (eV)	Particles	Conductivity (mho/m)
		58.69	1.82E+19	2.87	144054	1.87
		60.61	1.74E+19	2.91	143493	1.77
		58.91	1.83E+19	2.88	145026	1.88
		60.39	1.73E+19	2.89	143891	1.78
		60.10	1.78E+19	2.90	144729	1.82
		59.39	1.80E+19	2.89	143903	1.84
		59.26	1.80E+19	2.86	145637	1.86
		60.02	1.75E+19	2.91	143695	1.79
		59.83	1.76E+19	2.89	142933	1.80
		61.36	1.72E+19	2.91	144281	1.75
Average:		59.86	1.77E+19	2.89		1.82
Range	+	1.50	6.24E+17	0.02		0.07
	-	1.17	5.41E+17	0.03		0.06

Simulation:		1200 µm², 60 mJ, Horizontal				
		Radius (µm)	Density (m⁻³)	Temperature (eV)	Particles	Conductivity (mho/m)
		46.72	2.09E+19	2.86	184856	2.16
		47.13	2.06E+19	2.88	184344	2.11
		46.36	2.14E+19	2.87	186632	2.21
		46.65	2.13E+19	2.87	186514	2.19
		46.54	2.08E+19	2.88	184188	2.14
		46.78	2.08E+19	2.88	183798	2.14
		45.90	2.16E+19	2.88	185174	2.22
		46.14	2.15E+19	2.89	185612	2.20
		47.16	2.06E+19	2.88	184712	2.12
		47.18	2.08E+19	2.86	184823	2.15
Average:		46.66	2.10E+19	2.88		2.16
Range	+	0.52	5.97E+17	0.02		0.06
	-	0.76	4.84E+17	0.01		0.05

Simulation:		2400 µm², 60 mJ, Horizontal				
		Radius (µm)	Density (m⁻³)	Temperature (eV)	Particles	Conductivity (mho/m)
		49.46	2.02E+19	2.86	199065	2.08
		49.68	2.04E+19	2.86	198145	2.11
		48.62	2.10E+19	2.86	199228	2.17
		49.07	2.08E+19	2.88	199542	2.14
		50.16	2.02E+19	2.88	198694	2.08
		48.70	2.14E+19	2.86	200501	2.21
		48.94	2.07E+19	2.86	199133	2.14
		49.50	2.04E+19	2.88	198436	2.10
		49.99	2.03E+19	2.87	197214	2.09
		49.35	2.07E+19	2.86	199226	2.13
Average:		49.35	2.06E+19	2.87		2.12
Range	+	0.81	8.07E+17	0.01		0.09
	-	0.73	4.50E+17	0.01		0.05

Simulation:		3600 µm², 60 mJ, Horizontal				
		Radius (µm)	Density (m⁻³)	Temperature (eV)	Particles	Conductivity (mho/m)
		54.26	1.96E+19	2.87	208226	2.01
		53.51	2.00E+19	2.88	208946	2.06
		53.98	2.01E+19	2.85	209608	2.07
		53.94	2.00E+19	2.87	209793	2.05
		53.79	1.98E+19	2.87	209022	2.04
		53.12	2.05E+19	2.87	208526	2.11
		53.72	2.01E+19	2.87	209791	2.06
		53.36	2.02E+19	2.86	210051	2.08
		53.68	2.01E+19	2.88	208546	2.06
		52.74	2.09E+19	2.88	210111	2.15
Average:		53.61	2.01E+19	2.87		2.07
Range	+	0.65	8.17E+17	0.01		0.08
	-	0.87	5.49E+17	0.02		0.06

Simulation:		4800 µm², 60 mJ, Horizontal				
		Radius (µm)	Density (m⁻³)	Temperature (eV)	Particles	Conductivity (mho/m)
		60.02	1.86E+19	2.85	213930	1.92
		58.88	1.92E+19	2.88	214909	1.98
		60.60	1.84E+19	2.85	215693	1.90
		59.16	1.91E+19	2.87	215257	1.96
		59.95	1.87E+19	2.87	215158	1.93
		58.80	1.92E+19	2.86	214580	1.98
		58.98	1.92E+19	2.86	215507	1.98
		59.49	1.92E+19	2.85	216819	1.98
		59.53	1.91E+19	2.86	217046	1.96
		58.68	1.98E+19	2.86	216245	2.04
Average:		59.41	1.90E+19	2.86		1.96
Range	+	1.19	7.84E+17	0.02		0.08
	-	0.73	6.89E+17	0.01		0.07

Appendix V – Differential Equations Representing the Blumlein Circuit Model

$$\frac{\partial I_{switch}}{\partial t} = \frac{V_1 - I_{switch}R_{switch}}{L_{switch} + L}$$	$$\frac{\partial V_1}{\partial t} = \frac{I_2 - I_{switch}}{C}$$
$$\frac{\partial I_2}{\partial t} = \frac{V_2 - V_1}{L}$$	$$\frac{\partial V_2}{\partial t} = \frac{I_3 - I_2}{C}$$
$$\frac{\partial I_3}{\partial t} = \frac{V_3 - V_2}{L}$$	$$\frac{\partial V_3}{\partial t} = \frac{I_4 - I_3}{C}$$
$$\frac{\partial I_4}{\partial t} = \frac{V_4 - V_3}{L}$$	$$\frac{\partial V_4}{\partial t} = \frac{I_5 - I_4}{C}$$
$$\frac{\partial I_5}{\partial t} = \frac{V_5 - V_4}{L}$$	$$\frac{\partial V_5}{\partial t} = \frac{I_6 - I_5}{C} - \frac{R_{load}(V_5 - V_4)}{L}$$
$$\frac{\partial I_6}{\partial t} = \frac{V_6 - V_5}{L}$$	$$\frac{\partial V_6}{\partial t} = \frac{I_7 - I_6}{C} - \frac{R_{load}(V_5 - V_4)}{L}$$
$$\frac{\partial I_7}{\partial t} = \frac{V_7 - V_6}{L}$$	$$\frac{\partial V_7}{\partial t} = \frac{I_8 - I_7}{C} - \frac{R_{load}(V_5 - V_4)}{L}$$
$$\frac{\partial I_8}{\partial t} = \frac{V_7 - V_6}{L}$$	$$\frac{\partial V_8}{\partial t} = \frac{-I_8}{C} - \frac{R_{load}(V_5 - V_4)}{L}$$

Appendix VI – Mathematica File for Fluid Model

```mathematica
ρair = 1.29;
p = 3;
ξ = 4.5;
σ = 20000;
ao = .000035;
d = .002;
vo = 20000;
jo = 0;
acr = 0.002;
Z = 2;
c = 6.97 * 10^-9 / 4;
ind = Z^2 * c / 4;
ind1 = 100 10^-9;

p0 = ρair * p

3.87

a2[t_] := ao^2 + 4 / (π p0 ξ σ) ^ (1 / 3) ∫0.0^t Abs[j[t]] ^ (2 / 3) dt;

a[t_] := √(a2[t]) ;
r[t_] := d / (σ π a2[t]);
l[t_] := (2 * 10^-7) d Log[acr / a[t]] + ind1;

model = {v1'[t] == (j2[t] - j[t]) / c, v2'[t] == (j3[t] - j2[t]) / c, v3'[t] == (j4[t] - j3[t]) / c, v4'[t] == (j5[t] - j4[t]) / c,
    v5'[t] == (j6[t] - j5[t]) / c - 2 Z (v5[t] - v4[t]) / ind, v6'[t] == (j7[t] - j6[t]) / c - 2 Z (v5[t] - v4[t]) / ind,
    v7'[t] == (j8[t] - j7[t]) / c - 2 Z (v5[t] - v4[t]) / ind, v8'[t] == -j8[t] / c - 2 Z (v5[t] - v4[t]) / ind, j'[t] == (v1[t] - j[t] r[t]) / (ind + l[t]),
    j2'[t] == (v2[t] - v1[t]) / ind, j3'[t] == (v3[t] - v2[t]) / ind, j4'[t] == (v4[t] - v3[t]) / ind, j5'[t] == (v5[t] - v4[t]) / ind,
    j6'[t] == (v6[t] - v5[t]) / ind, j7'[t] == (v7[t] - v6[t]) / ind, j8'[t] == (v8[t] - v7[t]) / ind, v1[0] == v0, v2[0] == v0, v3[0] == v0,
    v4[0] == v0, v5[0] == v0, v6[0] == v0, v7[0] == v0, v8[0] == v0, j[0] == j0, j2[0] == j0, j3[0] == j0, j4[0] == j0, j5[0] == j0, j6[0] == j0, j7[0] == j0, j8[0] == j0};
input1 = { v0 → vo, j0 → jo};
soln = NDSolve[model /. input1, {v1, v2, v3, v4, v5, v6, v7, v8, j, j2, j3, j4, j5, j6, j7, j8}, {t, 0, (1000 * 10^-9)}, MaxSteps → 1000000]

{{v1 → InterpolatingFunction[{{0., 1. × 10^-6}}, <>], v2 → InterpolatingFunction[{{0., 1. × 10^-6}}, <>],
   v3 → InterpolatingFunction[{{0., 1. × 10^-6}}, <>], v4 → InterpolatingFunction[{{0., 1. × 10^-6}}, <>], v5 → InterpolatingFunction[{{0., 1. × 10^-6}}, <>],
   v6 → InterpolatingFunction[{{0., 1. × 10^-6}}, <>], v7 → InterpolatingFunction[{{0., 1. × 10^-6}}, <>], v8 → InterpolatingFunction[{{0., 1. × 10^-6}}, <>],
   j → InterpolatingFunction[{{0., 1. × 10^-6}}, <>], j2 → InterpolatingFunction[{{0., 1. × 10^-6}}, <>], j3 → InterpolatingFunction[{{0., 1. × 10^-6}}, <>],
   j4 → InterpolatingFunction[{{0., 1. × 10^-6}}, <>], j5 → InterpolatingFunction[{{0., 1. × 10^-6}}, <>], j6 → InterpolatingFunction[{{0., 1. × 10^-6}}, <>],
   j7 → InterpolatingFunction[{{0., 1. × 10^-6}}, <>], j8 → InterpolatingFunction[{{0., 1. × 10^-6}}, <>]}}

currentimage = Plot[j[t * 10^-9] /. soln, {t, 0, 200}, PlotRange → All, AxesLabel → {"time (ns)", "Current (A)"}]
```
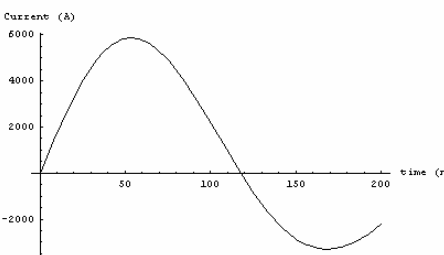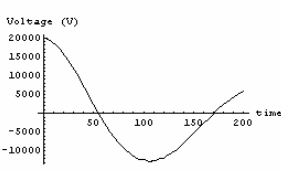
Current (A)

- Graphics -

```mathematica
tlinevoltage = Plot[v1[t * 10^-9] /. soln, {t, 0, 200}, AxesLabel → {"time (ns)", "Voltage (V)"}, PlotRange → All]
```

Voltage (V)
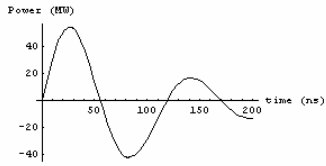
- Graphics -

`powerimage = Plot [v1[t * 10⁻⁹] * j[t * 10⁻⁹] / 10⁶ /. soln, {t, 0, 200}, AxesLabel → {"time (ns)", "Power (MW)"}, PlotRange → All]`

- Graphics -

`energystored = 6 * .5 c v₀^2`

2.091

`chargestored = N[8 * c * v₀ * 10⁶]`

278.8

`chargeswitch = NIntegrate[Evaluate[j[t1] /. soln] , {t1, 0, 50 * 10⁻⁹}] * 10⁶`

{174.05}

`int[t_] := NIntegrate[Evaluate[Abs[j[τ]^(2/3)] /. soln], {τ, 0, t}]`

`a22[t_] := a₀² + 4 / (π p0 ξ σ) ^ (1/3) * int[t]`
`a1[t_] := √a22[t]`
`r1[t_] := d / (σ π a22[t])`
`l1[t_] := (2 * 10⁻⁷) d Log[a_cr / a1[t]] + ind1`
`dl1[t_] := (-(2 * 10⁻⁷) d / a[t]) a1'[t]`

`vs[t_] := j[t] r1[t] + j'[t] l1[t]`
`v1[t_] := j5[t] 2 Z`

`powerdissipated2 = Plot[j[t * 10⁻⁹]² * r1[t * 10⁻⁹] / 10⁶ /. soln, {t, 0, 100}, AxesLabel → {"time(ns)", "Power Dissipated (MW)"}, PlotRange → All]`
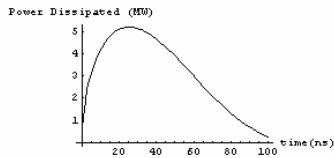
- Graphics -

`energyswitch = NIntegrate[Evaluate[r1[t1] * j[t1]² /. soln], {t1, 0, 50 10⁻⁹}]`

NIntegrate::nlim : τ = t1 is not a valid limit of integration. More…
NIntegrate::nlim : τ = t1 is not a valid limit of integration. More…
NIntegrate::nlim : τ = t1 is not a valid limit of integration. More…
General::stop : Further output of NIntegrate::nlim will be suppressed during this calculation. More…
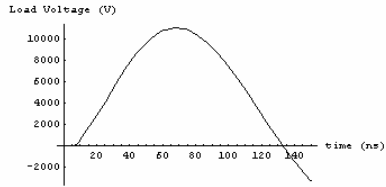
{{0.219132}}

`switchvoltage = Plot [vs[t * 10⁻⁹] /. soln, {t, 0, 100}, AxesLabel → {"time (ns)", "Switch Voltage (V)"}]`
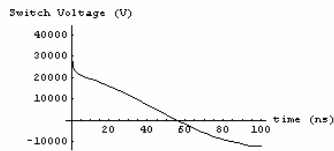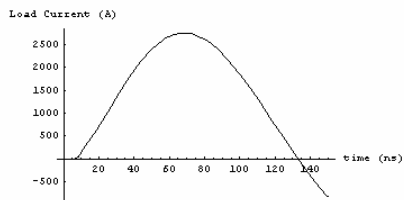

- Graphics -

`loadvoltage = Plot[v1[t * 10⁻⁹] /. soln, {t, 0, 150}, PlotRange → All, AxesLabel → {"time (ns)", "Load Voltage (V)"}]`

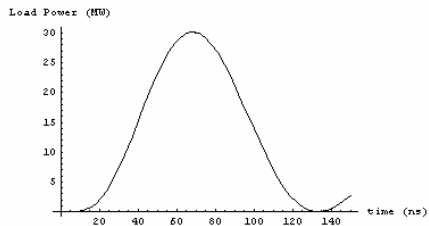Load Voltage (V)

- Graphics -

loadcurrent = Plot[j5[t * 10^{-9}] /. soln, {t, 0, 150}, PlotRange → All, AxesLabel → {"time (ns)", "Load Current (A)"}]

Load Current (A)

- Graphics -

loadpower = Plot[vl[t * 10^{-9}] j5[t * 10^{-9}] / 10^6 /. soln, {t, 0, 150}, PlotRange → All, AxesLabel → {"time (ns)", "Load Power (MW)"}]

Load Power (MW)

- Graphics -

energyload = NIntegrate[Evaluate[j5[t1] * vl[t1] /. soln], {t1, 0, 130 * 10^{-9}}]

{1.77898}

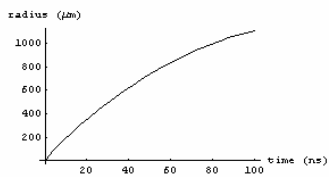chargeload = NIntegrate[Evaluate[j5[t1] /. soln], {t1, 0, 130 * 10^{-9}}] * 10^6

{209.139}

chargestored - chargeswitch - chargeload

{-104.389}
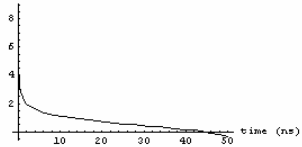
energystored - energyswitch - energyload

{{0.0928895}}

radiusimage = Plot[a1[t * 10^{-9}] * 10^6, {t, 0, 100}, AxesLabel → {"time (ns)", "radius (μm)"}, PlotRange → All]

radius (μm)

110

- Graphics -

r2image = Plot$\left[\text{Log}\left[10, \text{vs}\left[t*10^{-9}\right]/j\left[t*10^{-9}\right]\right]\right]$ /. soln, {t, 0, 50}, AxesLabel → {"time (ns)", "Log[$Z_{sv}(\Omega)$]"}, PlotRange → All]

Log[$Z_{sv}(\Omega)$]

time (ns)

- Graphics -

valuesimpedance = Table$\left[\text{Log}\left[10, \text{vs}\left[t*10^{-9}\right]/j\left[t*10^{-9}\right]\right]\right]$ /. soln, {t, .5, 50, .5}];

resistanceimage = Plot$\left[\text{Log}\left[10, r1\left[t*10^{-9}\right]\right]\right]$, {t, 0, 50}, AxesLabel → {"time (ns)", "Log[$R_{sv}(\Omega)$]"}, PlotRange → All]

Log[$R_{sv}(\Omega)$]
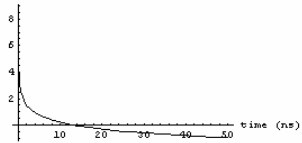
time (ns)

- Graphics -

valuesresistance = Table$\left[\text{Log}\left[10, r1\left[t*10^{-9}\right]\right]\right]$ /. soln, {t, .5, 50, .5}];

inductanceimage = Plot$\left[11\left[t*10^{-9}\right]*10^{9}\right]$, {t, 0, 50}, AxesLabel → {"time (ns)", "Inductance (nH)"}, PlotRange → All]

Inductance (nH)

time (ns)
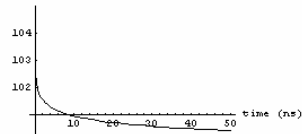
- Graphics -

valuesinductance = Table$\left[11\left[t*10^{-9}\right]*10^{9}\right]$ /. soln, {t, .5, 50, .5}];